

**Numerical and Experimental Study of
Target Detection and Localization in
Ultra Wideband Multiple-Input Multiple-Output Radars**

A dissertation submitted in partial fulfillment of the requirement for the degree
of doctor of engineering

at

Tokyo Denki University

by

IDNIN PASYA BIN IBRAHIM

March 2015

ABSTRACT

In recent years, radars utilizing multiple antennas at both the transmitter and receiver side have been proposed, where they have been referred to as multiple-input multiple-output (MIMO) radars. By utilizing transmit signals that are orthogonal to each other, MIMO radar yields increased degree of freedom that allows better target detection capability and higher localization accuracy compared to conventional radars using the same number of antennas. However, the complex composition of the MIMO radar system leads to various engineering challenges. This dissertation highlighted the issues of non-linear factors reducing the target detection performance of the MIMO radar, and unstable target localization due to fluctuating target radar cross sections. The thesis is composed into 6 chapters.

Chapter 1 explains the background of MIMO radar developments, and discusses recent research activities in the area. The definition and main category of MIMO radars are described, and their characteristics and advantages were discussed. Furthermore, we discussed the recent developments in MIMO radar research, and identified the remaining problems and challenges in the area.

Chapter 2 describes the fundamentals of the radar equation and detection. Firstly, the basic radar equation was presented, followed by the explanation of false alarm rate and probability of detection for monostatic coherent radars using threshold detection. Secondly, we described the fundamentals of array antenna signal processing principles, and direction estimations using high resolution sub-space approach, namely the multiple signal classification (MUSIC) algorithm will be presented. Extension to two-dimensional MUSIC and application for estimating the DOD and DOA in MIMO radar case was also explained.

Chapter 3 presents the study on performance of target detection in MIMO radars considering jitter influence. We constructed a time domain simulation model to evaluate the detection performance of M-sequence-based MIMO radars using three different types of joint signal processing scheme, namely the non-coherent MIMO, the coherent rephased netted radar (RPNR), and the distributed radar network (DRN) processing. The detection performance was evaluated while considering two types of jitter, which are the time and phase jitters. From numerical simulations, we observed that the presence of time jitter reduced the MIMO radar detection performance only in the case of a coherent processing (i.e. RPNR scheme), and was less significant for other processing schemes. On the other hand, phase jitters were found to give a direct impact on the P_d , regardless of the type of processing scheme. We also described a developed MIMO radar testbed for experimental evaluation of detection performance in a radio anechoic chamber.

Chapter 4 describes a new joint DOD and DOA estimation scheme in a UWB MIMO radar. The proposed scheme was based on a two-dimensional MUSIC algorithm extended for MIMO radar using a UWB signal. The idea was to treat the UWB signal as a summation of sinusoidal waves swept throughout the UWB frequency. The DOD and DOA were estimated at each of the frequency component of the UWB signal, and combined through majority decision. We carried out a series of numerical simulations and experimental evaluation to evaluate the performance of the proposed scheme in detecting targets with constant and fluctuating RCS. From our investigations, it was found that the proposed scheme was able to localize a fluctuating target with good accuracy compared to narrowband methods, since our proposed scheme exploited frequency diversity of the wideband signal. In addition, the proposed scheme outperformed conventional wideband estimation method such as the spectrum averaging method, when using wider signal bandwidth. This was ascribed to the effectiveness of the majority decision method.

In Chapter 5, we extended the joint DOD and DOA estimation scheme in MIMO radar to incorporate adaptive techniques for improved localization accuracy. Firstly we explains a method that implements target localization in a bistatic MIMO radar, using both DOD/DOA based, and TOA/DOA based direction estimation method. We derived the proposed scheme which applies the two-way MUSIC to detect the DOD, DOA and the TOA simultaneously. The radar system localizes a target location based on the estimated DOD, DOA and TOA, using two types of algorithm, namely the DOD/DOA-based, and the TOA/DOA based. We found from numerical simulations that the performance of the DOD/DOA-based was degraded when the vertical range perpendicular to the radar baseline increased, while that of the TOA/DOA-based method was almost independent of range. We then proposed implementation of an adaptive selection of localization method based on the estimated target range to improve the localization accuracy. Analyses of computational complexity also showed that the adaptive scheme yields reduced computational burden, especially when using larger MIMO configurations.

Chapter 6 concludes the works presented in the thesis. We have evaluated the influence of jitters on the detection performance of MIMO radars using three types of joint signal processing schemes. We also presented a new localization method in UWB MIMO radars that was effective in detecting target with fluctuating RCS. A direction finding scheme that adaptively selects localization method based on the estimated target range was also proposed.

Contents

Chapter 1 Introduction

1.1 Overview	1
1.2 Multiple-Input Multiple-Output Radar Technology	3
1.3 Recent Advancement in Multiple-Input Multiple-Output Research	9
1.4 Problem Statement	9
1.5 Outline of the Dissertation	10

Chapter 2 Radar Detection and Array Processing

2.1 Radar Detection	12
2.1.1 Radar Equation	12
2.1.2 False Alarm Rate and Detection Probability	13
2.2 Angle Estimation Schemes	16
2.2.1 Antenna Array Processing	16
2.2.2 High resolution and Sub-space Methods	19

Chapter 3 Detection Performance of M-Sequence-Based Multiple-Input Multiple-Output Radars

3.1 Introduction	28
3.2 M-Sequenced-Based Multiple-Input Multiple-Output Radar Signal Model	29
3.3 Signal Processing Schemes	31
3.4 Simulation of Detection Performance	34
3.4.1 Detection Performance in Ideal Conditions	34
3.4.2 Detection Performance Considering Jitter Influence	38
3.5 Development of Multiple-Input Multiple-Output Radar Testbed and Experimental Results..	50
3.6 Summary	56

Chapter 4 Joint Direction-of-Departure and Direction-of-Arrival Estimation in Ultra Wideband Multiple-Input Multiple-Output Radars

4.1 Introduction	58
4.2 Proposed Scheme	59
4.3 Simulations of Estimation Performance	66
4.3.1 Performance Detecting Targets with Constant Radar Cross Sections	66
4.3.2 Performance Undertaking Targets with Fluctuating Radar Cross Sections	71
4.4 Experimental Evaluation in Radio Anechoic Chamber	78
4.5 Summary	85

Chapter 5 Adaptive Target Localization Scheme in Bistatic Ultra Wideband Multiple-Input Multiple-Output Radars

5.1 Introduction	87
5.2 Proposed Localization Methods	88
5.3 Numerical Simulation	92
5.4 Experimental Evaluation	94
5.5 Implementation of Adaptive Scheme	96
5.6 Summary	98
Chapter 6 Conclusion	100
Reference	102
Acknowledgment	108
Appendices	109
Appendix A MIMO Radar Testbed Equipment Specifications	109
Appendix B Measured RCS Distribution of Automobiles against Frequency	111
Appendix C Range Resolution of Trilateration and Triangulation	114
Appendix D List of Publications and Awards	116

ACRONYMS

BPF	Band Pass Filter
DOD	Direction-of-Departure
DOA	Direction-of-Arrival
DRN	Distributed Radar Network
DSO	Digital Storage Oscilloscope
ESPRIT	Estimation of Signal Parameters via Rotational Invariance Techniques
FFT	Fast Fourier Transform
GPIB	General Purpose Interface Bus
IF	Intermediate Frequency
SISO	Single-Input Single-Output
MIMO	Multiple-Input Multiple-Output
MUSIC	Multiple Signal Classification
OFDM	Orthogonal Frequency Division Multiplexing
PDF	Probability Distribution Function
RCS	Radar Cross Sections
RMSE	Root Mean Square Error
RPNR	Re-Phased Netted Radar
Rx	Receiver
SNR	Signal to Noise Ratio
SVD	Singular Value Decomposition
TOA	Time-of-Arrival
Tx	Transmitter
ULA	Uniform Linear Array
UWB	Ultra Wideband
VNA	Vector Network Analyzer

NOTATIONS

$E[\cdot]$	Ensemble average operation
$[\cdot]^H$	Hermitian transpose operation
$[\cdot]^T$	Transpose operation
$\{\cdot\}$	Set of variables
\otimes	Kronecker product operator
M	Number of antenna in transmitting array
N	Number of antenna in receiving array
L	Number of target
K	Total frequency components

Chapter 1

INTRODUCTION

1.1. BACKGROUND

RADio Detection and Ranging (Radar) technology has been present more than 100 years, starting from the early experiments of the existence of electromagnetic waves by Heinrich Hertz, and are still evolving nowadays, into advance technology either in military, or civilian applications such as remote sensing, air traffic control, ship and automobile safety system [1, 2]. Radars deal with many different and diverse problems, however, most radar systems are generally designed for the purpose of detecting the presence or absence of targets. A basic form of radar consists of a single transmitter, which emits electromagnetic wave, and a receiver that collects the reflected wave coming off a reflecting object (the radar target). The receiver then processes the return signal to detect the presence of the target. Depending on the radar geometry and the type of signal used, it is possible for the radar system to extract other useful information such as range, location and velocity. Furthermore, target tracking ability may also allow the radar to predict the movement and trajectory of the target.

Conventional radar systems can be categorized by the radar geometry, which involves the number of antennas and how they are distributed in the system. These categories are referred to as monostatic, bistatic and multistatic radar systems [2]. Monostatic radar systems use transmitting and receiving antennas which are co-located to each other, and basically only a single antenna is used at both sides. When the transmitting antenna and receiving antenna are sufficiently separated in space, as such until their separation is in equal order with the target range, the system becomes a bistatic radar system. Radar system with the combination of multiple pairs of transmitting and receiving antennas are called multistatic radars systems, however, there is no strict definition to define the system. The multistatic radar can be constructed by multiple monostatic or bistatic radars, and the combinations of the two are also possible. Figure 1.1 depicts the illustration of the geometry of each radar system.

In target localization regime, it is important to estimate the angle of the targets, or the incoming reflected electromagnetic wave. Early radar systems utilized mechanically rotating directional antennas in order to scan over 360° of the observation angle for estimating the target location. Later on, array radars have been developed with the capability to synthesize beams to scan the whole space. In these systems, array of transmitting antennas is used at the transmitter side. In conventional approach, these antennas are closely distributed in space, and transmit the same signal from each element. The combined antenna beam can be steered in space by means of *beamforming* [1], which is

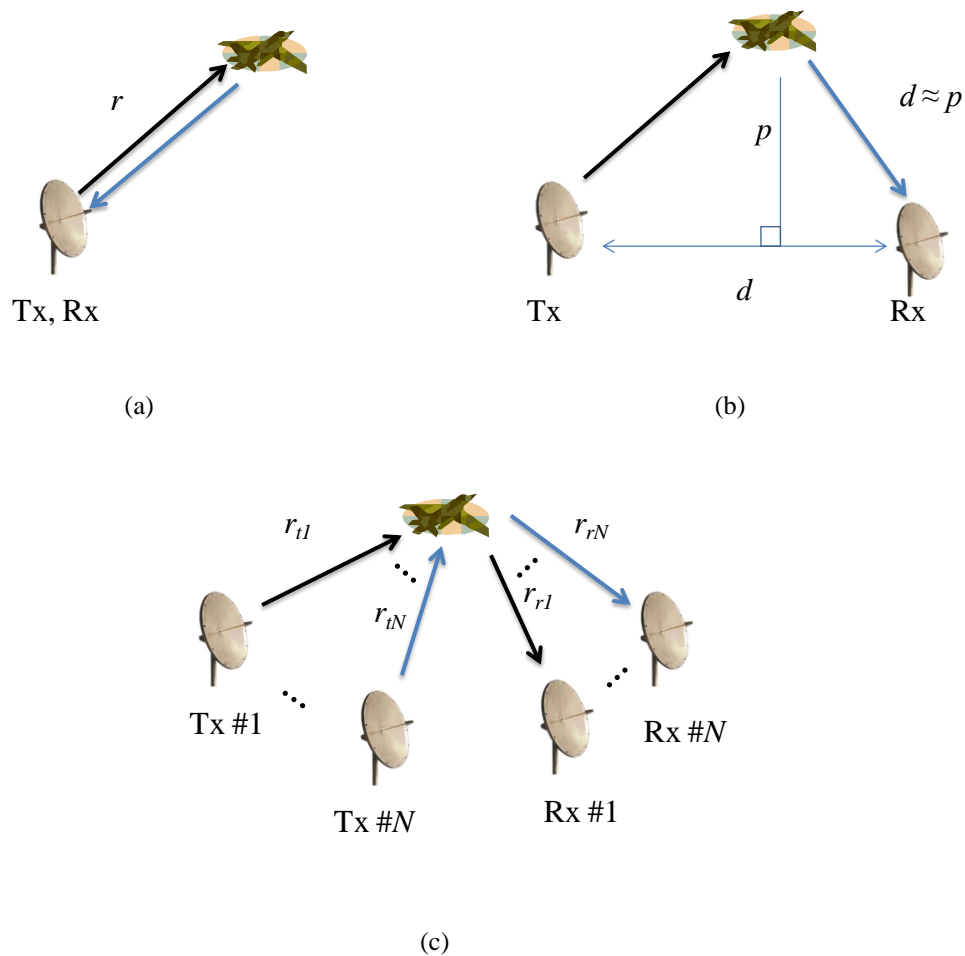


Fig. 1.1. Illustrations of basic radar geometry: (a) monostatic, (b) bistatic, and (c) multistatic.

basically a technique that controls the phases of each of these signals. This type of system is also called *phased array radars*. Other application of antenna arrays in radars includes the utilization of multiple antennas at the radar receivers for angle estimation, and imaging purposes.

In recent years, radars utilizing multiple antennas at both the transmitter and receiver side have been proposed, where they have been referred to as multiple-input multiple-output (MIMO) radars [3-5]. A MIMO radar system may transmit multiple signals that are orthogonal, correlated, or partially correlated with each other, where careful selection would increase the degree of freedom compared to the conventional phased array radar that uses the same number of antennas. Early works on MIMO radar indicated that the increase degree of freedom induces various benefit over conventional systems,

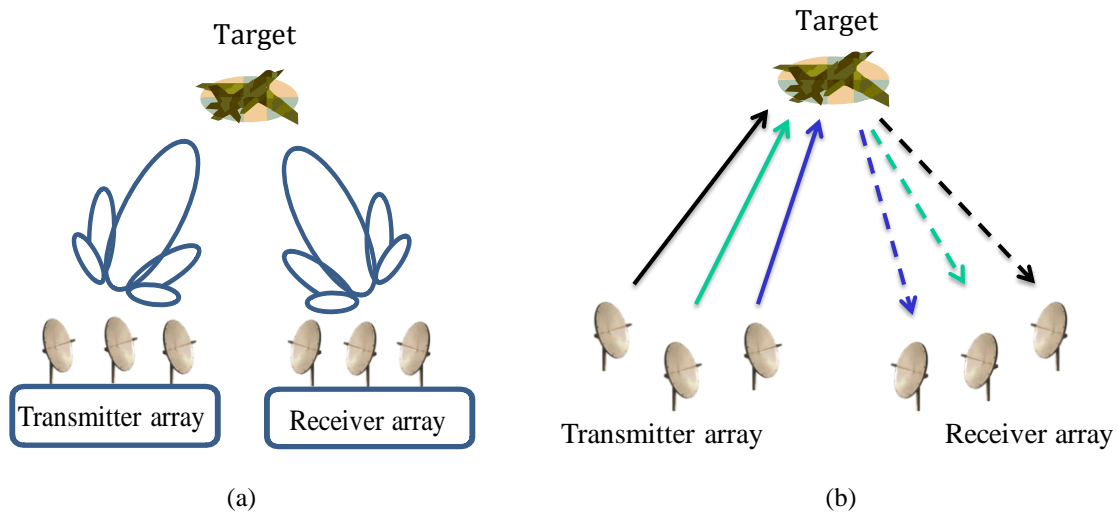


Fig. 1.1. Illustration of different radar systems: (a) Conventional phase array radar and (b) MIMO radar assuming independent transmitting signal.

such as improvement of number of detectable targets, resolution, and robustness against radar cross section (RCS) fluctuation. Nevertheless, the idea of MIMO radar have yet to be fully studied, and a lot more room for investigation is required to accelerate its development.

In the following section, we describe a brief overview of MIMO radar technology, discussing its definition, mechanism and its advantages and disadvantages compared to conventional systems.

1.2. OVERVIEW OF MULTIPLE INPUT MULTIPLE OUTPUT RADAR TECHNOLOGY

MIMO radar is loosely defined as a radar system that comprises of multiple antennas at the transmitter and receiver side. The system transmits signals that is orthogonal to each other, and combines the receive signal at a single processing unit. This is in-contrast with conventional phase array radars that generally transmit the same signal and utilize the electrical phase of each signal to control the antenna beam pattern. This different concept of both systems is briefly illustrated in Fig. 1.1. Based on the definitions above, MIMO radars can also be considered as a generalization of multi-static radar concepts. Some researchers defined MIMO radars as a sub-set or a special case of a multi-static radar geometry since their description usually fits the parameters of existing multi-static radar systems [6, 7]. For example the synthetic impulse and aperture radars (SIAR) [7] are existing systems that closely resemble MIMO radar.

Since MIMO radar deals with multiple antennas, there are several ways to configure the system, i.e. in terms of the array configuration, type of signal used, and type of processing used at the receiver. There are various concepts that have been proposed to define the term MIMO radar; however, this thesis holds to the most commonly addressed groups in literature, namely: (1) MIMO radar with widely separated antennas, and (2) MIMO radar with co-located antennas. The next subsections describe both types of radar systems.

A) MIMO radars with widely separated antennas

The first regime consists of multiple transmit and receive pairs which are widely separated in space, providing independent scattering responses for each pair. This type of MIMO radar is sometimes denoted as *statistical MIMO radar*, or *spatial MIMO radar*. The key point in this type of architecture is to sufficiently distribute the transmitting and receiving antennas of the radar system such that they experience an angular spread, where each transmit-receive antenna pairs illuminate obtained independent information of the target in terms of RCS variability as a function of aspect ratio. To be able to utilize these independent channels for stimulating increase processing gain, the receiver must be able to separate each receiving signal impinging the receiving antennas. This is why it is important to transmit orthogonal signals, which can be done using conventional techniques such as frequency, time or code division schemes. For the sake of clarifying the contribution of this thesis, detail discussions regarding the characteristics of orthogonal signal and their impact on the radar performance are not elaborated, since they are well documented in literatures [8]. The utilization of this angular spread is shown to yield spatial diversity that improves the detection performance of a MIMO radar detecting targets with fluctuating RCS, compared to conventional phased array radar.

In order to achieve the spatial diversity, certain conditions regarding the radar geometry must be met. Consider a model of MIMO radar geometry depicted in Fig. 1.3. Assume the MIMO radar is detecting a distributed target located in the far field. In this geometry, a 2×2 MIMO radar is considered for the sake of simplification and clarity. The distributed target considered in this model corresponds to a target with dimensions along the x and y axes be D_x and D_y , respectively. The target has a center of gravity in the x-y plane is given by $X_0 = (x_0, y_0)$.

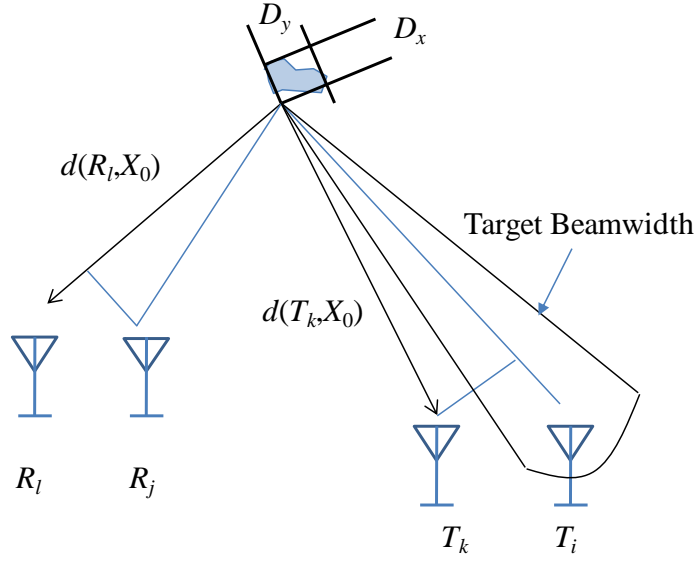


Fig. 1.3. MIMO radar geometry.

Let the two transmit antennas have coordinates (x_{tk}, y_{tk}) and (x_{ti}, y_{ti}) , respectively, and the receiving antennas at (x_{rl}, y_{rl}) and (x_{rj}, y_{rj}) . Here, the distance between transmitting or receiving antenna and the target at X_0 is given by the notation $d(*, X_0)$. The conditions so that each transmitting and receiving antenna pair yields uncorrelated channel information between each other is given in [3] as

$$\begin{aligned} \frac{x_{tk}}{d(T_k, X_0)} - \frac{x_{ti}}{d(T_i, X_0)} &> \frac{\lambda}{D_x} \\ \frac{y_{tk}}{d(T_k, X_0)} - \frac{y_{ti}}{d(T_i, X_0)} &> \frac{\lambda}{D_y} \\ \frac{x_{rl}}{d(R_l, X_0)} - \frac{x_{rj}}{d(R_j, X_0)} &> \frac{\lambda}{D_x} \\ \frac{y_{rl}}{d(R_l, X_0)} - \frac{y_{rj}}{d(R_j, X_0)} &> \frac{\lambda}{D_y}, \end{aligned} \quad (1.1)$$

where λ is the wavelength of the radar signal. These indicates that if the target is viewed as an antenna with aperture length D , the information observed from a receiving antenna is considered uncorrelated if the beamwidth from the target cannot illuminate two receivers simultaneously. For instance, for a

target of dimension 10λ is positioned at distance $d = 10^4\lambda$, the separation required between the antennas of MIMO radar is in the order of $10^3\lambda$.

B) MIMO radars with co-located antennas

The second regime of MIMO radar refers to systems that comprise closely spaced transmitting and receiving antennas, where the term ‘closely’ here denotes that the spacing is much smaller than the target range. This also means that none of the conditions in Eq. (1.1) is met. Such MIMO radar configuration assumes that the target scattering response is the same for each receiving antenna. The estimation performance of the antenna, thus do not exploit spatial diversity as the MIMO radars with widely separated antennas. However, MIMO radars with co-located antennas take advantage of the enhanced aperture resolution of its antenna array compared to conventional antenna array, for example such used in phased array radars. The enhanced array resolution is achieved through the concept of *virtual array*, which can be constructed by the convolution of the locations of the respective transmitting and receiving antennas, with the condition that the system transmits orthogonal waveforms [9]. The utilization of an efficient virtual array leads to improvement in parameter estimation performance and increased maximum number of detectable targets compared to conventional phased array radar using the same number of antennas [10].

To illustrate the concept of virtual array, consider a MIMO radar in Fig. 1.3. Here, Consider an arbitrary array with M transmitting antennas and N receiving antennas. The m^{th} transmitting antenna is located at $\mathbf{x}_{T,m}$ and the n^{th} receiving antenna is located at $\mathbf{x}_{R,n}$. Figures 1.3 (a) and (b) show an example with $M = 3$, and $N = 3$. The m^{th} transmitting antenna emits the waveform $\phi(\tau)$. Assuming that the transmitted waveforms are orthogonal to each other, the equation below can be derived.

$$\int \phi_m(\tau)\phi_m^*(\tau)d\tau = \delta_{m,m} . \quad (1.2)$$

To separate each of the transmitting waveform, a bank of matched filters (total of M) is used at the MIMO radar receiver. Hence, the total number of receiving outputs at all N receivers is $M \times N$. Considering a far-field target, the target response at the m^{th} match filter output of the n^{th} receiving antenna can be expressed by

$$y_{n,m}^{(t)} = \rho_t \exp\left(j \frac{2\pi}{\lambda} \mathbf{u}_t^T (\mathbf{x}_{T,m} + \mathbf{x}_{R,n})\right), \quad (1.3)$$

where \mathbf{u}_t is a unit vector pointing towards the target from the radar and ρ_t is the amplitude coefficient of the signal reflected from the target.

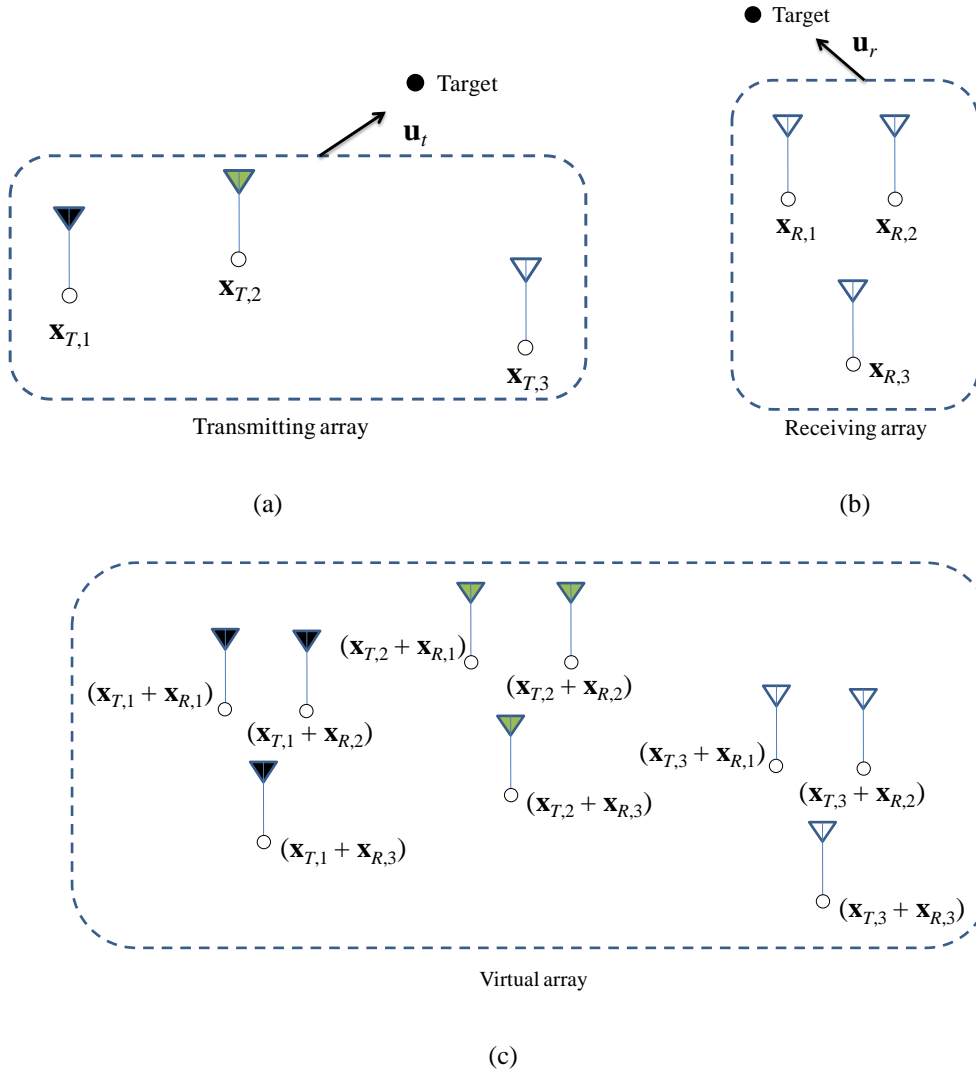


Fig. 1.3. Illustration of virtual array concept in MIMO radar: (a) Transmitting array with $M = 3$, (b) receiving array with $N = 3$, and (c) the corresponding virtual array.

The phase differences are created by both the transmitting and receiving antennas locations, located at

$$\{\mathbf{x}_{T,m} + \mathbf{x}_{R,n} \mid m = 0,1,\dots,M-1, n = 0,1,\dots,N-1\}.$$

As shown in Fig. 1.3 (c), by using only $N + M$ elements, a virtual array of NM elements can be constructed using MIMO radar. This is far more elements than using a conventional phased array radars with the same number of physical antennas, because they are treated as a single-input multiple-output (SIMO) array with $M = 1$, therefore resulting in only $(M+N) - 1$ array length.

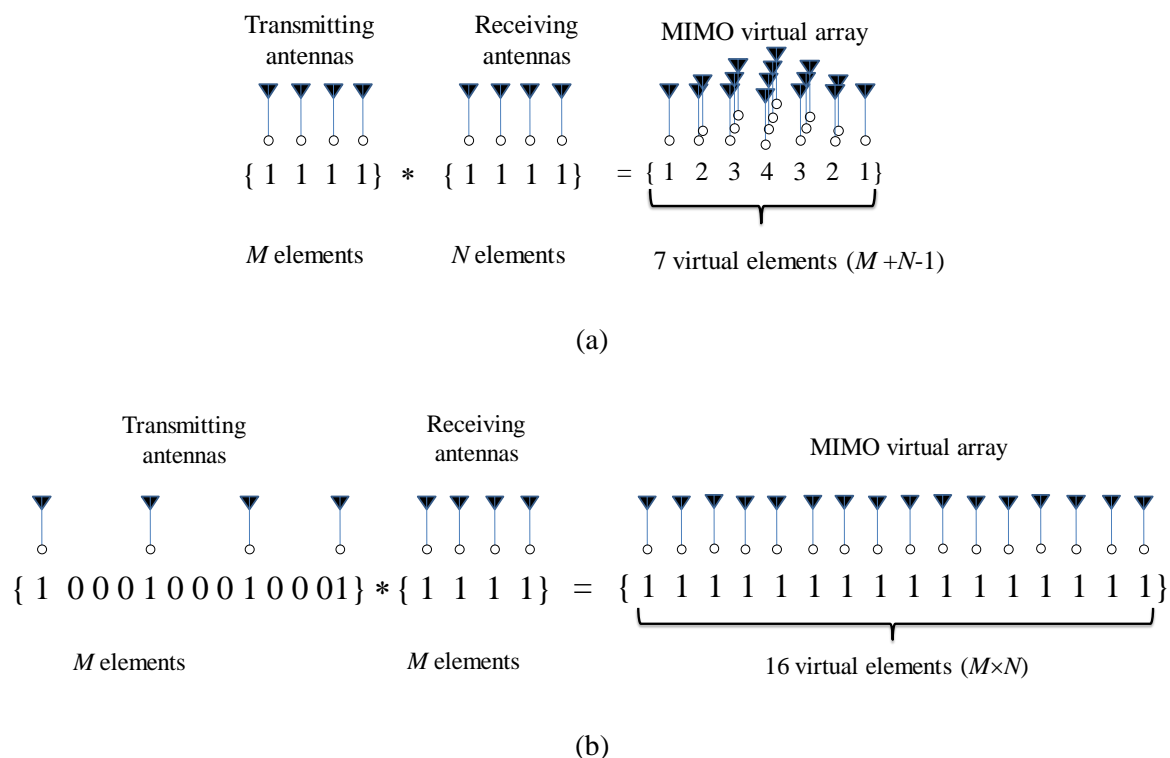


Fig. 1.4. Examples of MIMO radar antenna configurations, and the resulting virtual arrays: (a) with redundant elements and (b) without redundant elements.

Nevertheless, in order to obtain a full $M \times N$ number of virtual antenna elements as depicted in Fig. 1.3 (c), either the transmitting or receiving antennas must be sparsely positioned in spacing such that yields convolution results that are unique from each other [9]. This is to avoid overlapping elements as a result of the convolutional operation. Figure 1.3 illustrates this concept further. Let the physical transmitting and receiving antennas position using the notation $\{1\ 1\ 1\ 1\}$, where each entry corresponds to the number of antennas at the particular location on the $\lambda/2$ grid, where λ is the wavelength. Using this array at both the transmitting and receiving side, the constructed virtual array by calculating the convolution of the physical antenna positions resulted in $\{1\ 2\ 3\ 4\ 3\ 2\ 1\}$. Here, we obtained a virtual array with a length $(M+N) - 1$, since the convolution operation marked several redundant antenna positions, as depicted in Fig. 1.4(a). By sufficiently separating either one of the transmitting or receiving array, we could obtain a convolution result without any redundant element, hence, the length of the virtual array may reach $M \times N$ (Fig. 1.4 (b)).

1.3. RECENT ADVANCEMENTS IN MIMO RADAR RESEARCH

It was shown in the previous sub-section that the spatial MIMO radar excels in exploiting the benefit of spatial diversity to increase the probability of detection. Early ideas on the spatial MIMO radar was proposed in [11]. Recent works investigated further in the regime, for example, through introduction of statistical hypothesis test to define the detection performance of the system [3, 12]. Other works involves the study concerning high resolution [13] and accuracy of location estimation [14] using the spatial MIMO radar. In addition, the impacts of different target and environment models on MIMO radar detection were discussed in [15, 16]. Several designs of transmit waveform including adaptive waveform designs can be found in [17, 18]. Nevertheless, since the spatial MIMO radar comprises of large systems of widely separated antennas, the system tends to have complex hardware and heavy signal processing, that leads to engineering and implementation problems, for example, centralized coordination of sensor transmissions, synchronized communication with a joint processing unit, and precise phase synchronization among sensor for high resolution in the order of meters [4, 6].

In the MIMO radars with co-located antennas, researches are focused on the target localization and parameter identifiability. Utilization of the virtual array and orthogonal signals was reported to yield enhanced parameter identifiability [5], and sensitivity to detect slow moving targets [6]. Furthermore, in target localization regime, a lot of investigation on estimation of direction-of-departure (DOD) and direction-of-arrival (DOA) were reported. Many algorithms were studied, such as LS, Capon and APES, and CAPES [19, 20]. In addition, sub-space methods such as estimation of signal parameters via rotational invariance techniques (ESPRIT) and multiple signal classification (MUSIC) for DOA estimation in MIMO radars can be found, for example in [21-23]. These reports were mainly focused on the usage of narrowband signals in MIMO radars, which however resulted in unstable localization due to RCS fluctuations of the target. Inspired by recent advancement in communications, the usage of wideband signals including the Ultra Wideband (UWB) in MIMO radar are also interesting and is receiving a lot of attention [24-26].

1.4. PROBLEM STATEMENT

We have presented the overview of MIMO radar technology in the previous sections, and discussed some of the problems and research gaps in the literature. Here, we summarized the current problems concerning MIMO radars which motivated the work carried out in this thesis:

i) MIMO radars consist of large numbers of transmitters and receivers distributed in the system, thus increased the system complexity compared to conventional SISO systems. This will increase the effects of hardware imperfections such as coordination of transmitting sensors, communication with the joint processing unit, and synchronization errors on the system performance, particularly in MIMO radars utilizing widely distributed antennas. One of the factors inducing these problems is the presence of jitters in the MIMO radar receivers.

ii) In the regime of target localization in MIMO radars, currently available solutions were mainly based on narrowband signal assumption. Target localization using the narrowband signal, however, was unstable due to fluctuation of target's RCS. Utilization of wideband signals might be useful in localizing target with significantly small or severely fluctuating RCS, however, conventional algorithms proposed for MIMO radars generally only consider narrowband signal.

1.5. OUTLINE OF THESIS

This thesis presents numerical and experimental studies regarding several of the problems in MIMO radar. Firstly, we carried out investigation on the effects of jitter on the detection performance of MIMO radar system, with regards to the type of signal processing scheme used. The second part of the dissertation focused on the problem of angle estimation in MIMO radar. The rest of this dissertation is organized as follows.

Chapter 2 describes the fundamentals of the radar equation and detection. Firstly, the basic radar equation were presented. Then, we derived the false alarm rate and probability of detection for monostatic coherent radars using threshold detection. Secondly, we described the fundamentals of array antenna concept that was use in parameter estimation schemes. The angle and time of arrival estimations using high resolution sub-space approach will be presented. Techniques using MUSIC algorithm will be described since we will be utilizing the method in later chapters of the dissertation. Extension to two-dimensional MUSIC and application for estimating the DOD and DOA in MIMO radar case was also be explained.

Chapter 3 presents the study on performance of target detection in MIMO radars considering jitter influence. We constructed a time domain simulation model to evaluate the detection performance of m-sequence-based MIMO radars using three different types of joint signal processing scheme, namely the non-coherent MIMO, the coherent rephrased netted radar (RPNR), and the distributed radar network (DRN) processing. The detail description of these processing schemes will

be explained in Chapter 3. The detection performance was evaluated while considering two types of jitter, which are the time and phase jitters. The effects of each type of jitter were evaluated separately in order to obtain further insight of their impacts on the performance of the MIMO radar. A MIMO radar testbed was developed for experimental evaluation of detection performance in a radio anechoic chamber.

Chapter 4 describes a joint DOD and DOA estimation scheme in a UWB MIMO radar. We first explain the proposed scheme, which were based on a two-dimensional MUSIC algorithm extended for MIMO radar using a UWB signal. The idea was to treat the UWB signal as a summation of sinusoidal waves swept throughout the UWB frequency. The DOD and DOA were estimated at each of the frequency component of the UWB signal, and combined through majority decision. The majority decision was a non-parametric approach that takes the histograms of the estimated DODs and DOAs. Searching the peak of the respective angle histograms gives us the final DOD and DOA estimation. We carried out a series of numerical simulations to evaluate the performance of the proposed scheme in detecting targets with constant and fluctuating RCS. The fluctuating target was modeled according to measurement results of vehicular RCS using a UWB signal, which resembles Weibull distribution along the UWB frequency. We will show that the proposed scheme outperforms conventional wideband estimation method such as the spectrum averaging method, especially when using significantly wide bandwidth. We then present some experimental results using the proposed scheme to detect complex target with fluctuating RCS in the radio anechoic chamber.

Chapter 5 presents extended joint DOD and DOA estimation scheme in MIMO radar incorporating adaptive techniques for improved localization accuracy. Firstly we explains a method that implements target localization in a bistatic MIMO radar, using both DOD/DOA based, and TOA/DOA based direction estimation method. We will derive the proposed scheme which applies the two-way MUSIC to detect the DOD, DOA and the TOA simultaneously. The performance of both method will be evaluated in two significant cases, which corresponds to whether the target is in close proximity or is far from the baseline. It will be shown that by selecting either of the DOD/DOA and TOA/DOA method may improve the localization accuracy.

Chapter 6 summarizes the concluding remarks of previous chapters and discusses future works and potential research topics.

Chapter 2

TARGET DETECTION AND ARRAY SIGNAL PROCESSING

2.1. TARGET DETECTION

2.1.1. RADAR EQUATION

The fundamental radar equation relates the target range from the radar to the characteristics of transmitter, receiver, antenna, the target and environment. It is a tool for understanding radar operation and as a basis for designing a radar system. This sub-section will describe the basic derivation of the radar equation in the case of a monostatic radar operating in a single-input single-output (SISO) mode.

Consider a monostatic radar detecting a target located at the far field, with range R from the radar station. Radars use directive antennas to radiate electromagnetic signal with power P_t , into a particular direction. The gain G of the antenna is a measure of the increase power radiated in the particular direction, as compared with the power of an isotropic antenna. Based on the conventional antenna theory, antenna gain G is characterized by the antenna effective aperture A_e by the equation

$$G = \frac{(4\pi A_e)^2}{\lambda^2}. \quad (2.1)$$

Hence, the power density P_D the target surface from the antenna with a transmitting gain G is

$$P_D = \frac{P_t G}{4\pi R^2}. \quad (2.2)$$

The target intercepts a portion of the incident power, inducing surface current on its surface and re-radiates the electromagnetic energy in various directions. The amount of the re-radiated energy in the direction of the radar receiver is proportional to the target size, orientation and target shape, which are denoted as the radar cross sections (RCS) σ . Therefore, the total power directed to the radar receiver is

$$P_{Dr} = \frac{P_t G}{4\pi R^2} \cdot \frac{\sigma}{4\pi R^2}. \quad (2.3)$$

Considering the antenna receiving gain and effective aperture, the total receive power at the receiving antenna is

$$P_r = \frac{P_t G}{4\pi R^2} \cdot \frac{\sigma}{4\pi R^2} A_e. \quad (2.4)$$

And substituting the value of A_e from Eq. (2.4) yields

$$P_{Dr} = \frac{P_t G^2 \lambda^2 \sigma}{(4\pi)^3 R^4}. \quad (2.5)$$

Denoting S_{\min} as the minimum detectable signal power, a simple form of the radar equation can be formed as

$$R_{\max} = \left[\frac{P_t G^2 \lambda^2 \sigma}{(4\pi)^3 S_{\min}} \right]^{1/4}. \quad (2.6)$$

Application of this radar equation enables easy visualization of how the performance of the radar equipments in the system influences the detectable range. This is useful in designing the link budget of any operating radar system. Practical systems must also consider non-ideal conditions such as the influence of the earth surface on propagation characteristics, reflections from ground, and other factors contributing to noise components of the system [2].

2.1.2. FALSE ALARM RATE AND PROBABILITY OF DETECTION

A simplified block diagram of a radar receiver conducting a threshold detection is depicted in Fig. 2.1. The receiver considered a coherent detection, consists of local oscillator and IF amplifier, envelope detection circuit and a threshold detection. The envelope detector consists of a square law detector (rectifier), and a low pass filter to eliminate the high frequency components of the carrier signal. Let the input signal to the receiver be the reflected signal $s(t)$, and the thermal noise at the receiver as white Gaussian noise $n(t)$ with zero mean and variance ψ_0 . The output of the IF amplifier is a complex sinusoidal signal $v(t)$, given by

$$v(t) = v_I \cos \omega_0 t + v_Q \sin \omega_0 t = R \cos(\omega_0 t - \varphi(t)), \quad (2.7)$$

where ω_0 is the radial frequency equals to $2\pi f_0$, $r(t)$ is the envelope of the IF output signal, $\varphi(t)$ is the phase equals to $\text{atan}(v_I/v_Q)$, and v_I and v_Q , respectively, is the magnitude of the in-phase and quadrature phase components. A threshold detection works based on the principle that a target is detected according to the below hypothesis:

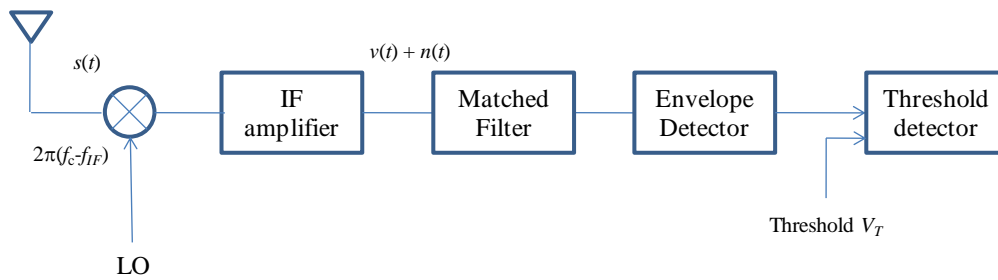


Fig. 2.1. Example of a simplified block diagram of a coherent radar receiver applying threshold detection.

$$s(t) + n(t) > V_T \Rightarrow \text{Detection}$$

$$n(t) > V_T \Rightarrow \text{False detection}$$

The probability density function (PDF) of the thermal noise is

$$p(v) = -\frac{1}{\sqrt{2\pi}\psi_0} \exp\left(-\frac{R^2}{2\psi_0}\right), \quad (2.8)$$

The probability density function of the noise voltage passed through a narrowband IF filter is shown by [2] to be

$$p(R) = \frac{R}{\psi_0} \exp\left(-\frac{R^2}{2\psi_0}\right), \quad (2.9)$$

where R is the amplitude of the envelope of the filter output. Notice that Eq. (2.8) represents the Rayleigh probability density function. Therefore, the probability that the envelope of the noise voltage will lie between the values of V_1 and V_2 is

$$p(V_1 < V_2) = \int_{V_1}^{V_2} \frac{R}{\psi_0} \exp\left(-\frac{R^2}{2\psi_0}\right) dR. \quad (2.10)$$

The probability that the noise envelope will exceed the voltage threshold V_T is

$$p(V_T < R < \infty) = \int_{V_T}^{\infty} \frac{R}{\psi_0} \exp\left(-\frac{R^2}{2\psi_0}\right) dR = \exp\left(-\frac{V_T^2}{2\psi_0}\right) = P_{fa}. \quad (2.11)$$

A target detection is considered to have occurred when the voltage of the noise envelope exceeds the threshold V_T , even if there was no target present in the system, and only noise is present. The probability of the noise envelope exceeds the threshold is referred to as the *probability of false alarm*, denotes as P_{fa} in the rest of this thesis.

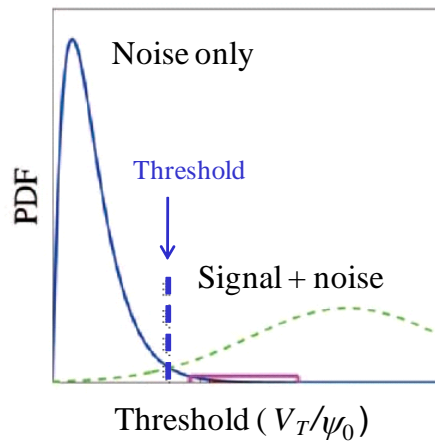


Fig. 2.2. Illustration of the relation between probability density function of noise and signal plus noise in threshold detection.

Next, consider that a target is present, and the reflected signal enters the radar receiver. In this case, the probability of the voltage of the envelopes of the signal plus noise exceed the threshold is called the *probability of detection*, denotes as P_d . Assuming the signal is a sine wave of amplitude A , the P_d is then given by [2, 27]

$$P_d = \int_{V_T}^{\infty} \frac{R}{\psi_0} \exp\left(-\frac{R^2 + A^2}{2\psi_0}\right) I_0\left(\frac{RA}{\psi_0}\right) dR, \quad (2.12)$$

where where I_0 is the modified Bessel function of zero order. Several approximations for solving Eq. (2.11) is available in literature [27], however, we omit them for the sake of simplicity. It is important to understand that Eq. (2.11) showed that the problem of deriving P_d is related to the PDF of signal and noise in the system, where the threshold value set from the PDF of the noise will be also used as the lower threshold for the signal plus noise. The illustration of the process of threshold detection is shown in Fig. 2.2.

B. Probability of False Alarm and Probability of Detection in MIMO Case.

The extension of the probability of false alarm and probability of detection in MIMO case depends on the configuration of the MIMO radar system itself. This is because the MIMO radar system may adopt different method to exploit the receiving signals entering the receiver, hence, the equation to define the P_{fa} and P_d differs for each method. Examples of the derivation of P_{fa} and P_d for various MIMO case can be found in [3, 6]. In this thesis, we will define a model of MIMO radar configuration using three different types of signal processing in Chapter 3, and the corresponding detection performance will be discussed in part of the chapter.

2.2. PARAMETER ESTIMATION SCHEMES

2.2.1. ARRAY SIGNAL PROCESSING FUNDAMENTALS

This sub-section discusses the basic principle of array signal processing for direction finding. The most important concept of the array antenna processing is the *array manifold vector* (referred to as *steering vector* throughout this thesis), which expresses the spatial characteristics of signal impinging the array elements. The steering vector is formed as a function of the signal frequency, the geometry of antenna array and the respective direction-of-arrival (DOA) of the sources. The basic model of the plane wave propagation from a far-field source towards an antenna array in a three-dimensional space is shown in Fig. 2.3. Consider an array of antennas located in the three-dimensional space with a common reference point. Assuming that there are L sources located at the far-field, the propagating wave can be treated as a travelling plane wave.

For a better understanding, we derive the model while addressing a two-dimensional uniform linear array (ULA). Consider a ULA shown in Fig. 2.4, where N antenna elements are located along the x -axis with d interval. Taking the input signal at the reference array element as $F_0(t)$, and the receive signal power at the rest of the array elements are the same, the signal at the n^{th} element can be expressed by

$$F_n(t) = F_0(t - \tau_n), \quad (n = 1, 2, \dots, N) \quad (2.13)$$

$$\tau_n = \frac{d_n \sin \theta}{c}. \quad (2.14)$$

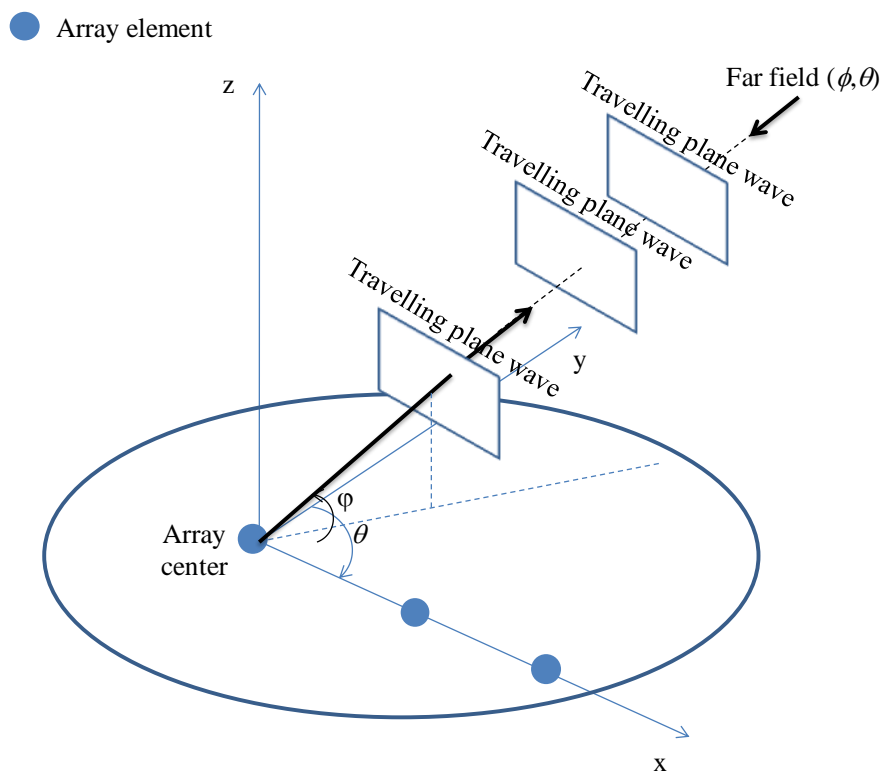


Fig. 2.3. Plane wave propagation model.

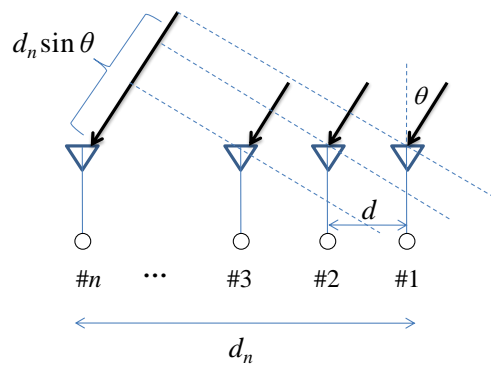


Fig. 2.4. Uniform linear array with N antenna elements.

where c is the speed of light, d_n is the position of the n^{th} element with respect to the reference element. Here, assuming that the receiving signal is narrowband with frequency f , we can derived the below equation.

$$F_n(t) = F_0(t - \tau_n) \cong F_0(t) \exp(-j2\pi f \tau_n) \quad (2.15)$$

$$= F_0(t) \exp(-j2\pi f \frac{d_n}{c} \sin \theta). \quad (2.16)$$

When considering in the function of wavelength λ (using $f = c/\lambda$), Eq. (2.15) becomes

$$F_n(t) = F_0(t) \exp(-j2\pi \frac{d_n}{\lambda} \sin \theta). \quad (2.17)$$

Hence, based on the geometry depicted in Fig. 2.4, the receive complex signal at the n^{th} element is then expressed by

$$x_n(t) = F_l(t) e^{j\phi_n(\theta_l)} + z_n(t), \quad (2.18)$$

where $F_l(t)$ is the complex signal of the l^{th} wave, z_n is the thermal noise and

$$\phi_n(\theta_l) = \frac{2\pi}{\lambda} (n-1)d \sin \theta_l. \quad (2.19)$$

Now, deriving the overall signal while considering L wave (in radar systems, the L corresponds to the number of reflected wave from L targets) impinging a ULA with N number of antenna elements, the input signal vector is given by

$$\begin{aligned} \mathbf{x}(t) &= \sum_{l=1}^L F_l(t) \mathbf{a}(\theta_l) + \mathbf{z}(t) \\ &= \mathbf{A} \mathbf{f}(t) + \mathbf{z}(t), \end{aligned} \quad (2.20)$$

where \mathbf{A} is a $N \times L$ matrix of the steering vector, \mathbf{f} is the array manifold vector consisting of spatial information of the array, and \mathbf{z} is a $N \times 1$ thermal noise vector. Here,

$$\mathbf{A} = [\mathbf{a}^L(\theta_1), \dots, \mathbf{a}^L(\theta_l), \dots, \mathbf{a}^L(\theta_L)] \quad (2.21)$$

$$\mathbf{a}^L(\theta_l) = [e^{j\phi_1(\theta_l)}, \dots, e^{j\phi_n(\theta_l)}, \dots, e^{j\phi_N(\theta_l)}] \quad (2.22)$$

$$\mathbf{f}(t) = [F_1(t), F_2(t), \dots, F_L(t)]^T. \quad (2.23)$$

where $[\cdot]^T$ is the transpose operation, ϕ_n is the phase difference at the n^{th} receive element with respect to the reference element (usually the 1st element). θ_l is the unknown angle of the l^{th} arriving signal.

2.2.2. HIGH RESOLUTION SUB-SPACE APPROACH IN PARAMETER ESTIMATION

Various schemes in estimating the angle of arrival were developed based on utilization of the characteristics of the co-variance matrix, for example the CAPON [28] method. The method works by steering the main lobe to the direction of arrival, while minimizing the radiated power in other directions by steering the null points. Later, high resolution methods exploiting the receiving co-variance matrix, eigenvectors and eigenvalues to separate the signal and noise into orthogonal sub-spaces were developed, for example MUSIC [29] and ESPRIT [30]. This study utilizes the MUSIC algorithm due to its high resolution and multi-target estimation capabilities. The next sub-sections describe the MUSIC algorithm.

A. MUSIC algorithm

MUSIC algorithm is one of the angle estimation method that exploits the eigenvalues and eigenvectors of the co-variance matrix. The MUSIC algorithm works based on sub-space approach, where signal and noise sub-space were constructed from the received signal. The orthogonal properties of the sub-spaces are exploited to achieve high resolution angle estimation.

In order to derive the MUSIC algorithm, we first revisit Eqs. (2.20) to (2.24), where we have defined the signal model, and the co-variance matrix for a K -element uniform linear array. Singular value decomposition of the co-variance matrix gives

$$\begin{aligned}
 R_{xx} &= E[\mathbf{x}(t)\mathbf{x}^H(t)], \\
 &= \mathbf{A}E[\mathbf{f}(t)\mathbf{f}^H(t)]\mathbf{A}^H + E[\mathbf{z}(t)\mathbf{z}^H(t)] \\
 &= \mathbf{A}\mathbf{S}\mathbf{A}^H + \sigma^2\mathbf{I},
 \end{aligned} \tag{2.24}$$

Here, $E[\cdot]$ denotes the ensemble averaging operation, σ is the thermal noise variance, and \mathbf{I} is the identity matrix that consists of only diagonal elements equal to 1. The co-variance matrix is a Hermitian matrix with N dimension.

Consider the case where no thermal noise is present. If the arriving waves are in-coherent with each other, the matrix \mathbf{S} will yield a diagonal matrix, with L rank. Assuming all the L waves are uncorrelated and independent from each other, the directional matrix \mathbf{A} will also resembles a full L rank matrix. Consequently, \mathbf{R}_{xx} becomes an L rank non-negative definite Hermitian matrix. The eigenvalues of this matrix are μ_i ($i = 1, 2, \dots, N$), and the corresponding eigenvectors are \mathbf{e}_i ($i = 1, 2, \dots, N$). Hence, the below relationship is established.

$$\mathbf{A}\mathbf{S}\mathbf{A}^H\mathbf{e}_i = \mu_i\mathbf{e}_i \quad (i = 1, 2, \dots, N). \quad (2.25)$$

The eigenvalues are

$$\mu_1 \geq \mu_2 \geq \dots \mu_L > \mu_{L+1} = \dots = \mu_N = 0. \quad (2.26)$$

The eigenvectors are

$$\mathbf{e}_i^H \mathbf{e}_n = \delta_{in} \quad (i, n = 1, 2, \dots, N), \quad (2.27)$$

where δ denotes the kronecker delta.

Considering the presence of thermal noise,

$$\begin{aligned} R_{xx}\mathbf{e}_i &= (\mathbf{A}\mathbf{S}\mathbf{A}^H + \sigma^2\mathbf{I})\mathbf{e}_i \\ &= \mathbf{A}\mathbf{S}\mathbf{A}^H\mathbf{e}_i + \sigma^2\mathbf{e}_i \\ &= \mu_i\mathbf{e}_i + \sigma^2\mathbf{e}_i \\ &= (\mu_i + \sigma^2)\mathbf{e}_i \quad (i = 1, 2, \dots, N), \end{aligned} \quad (2.28)$$

We can see in Eq. (2.29) that the eigenvectors with the presence of noise is identical to the eigenvectors with the absence of noise, having an additional term that contributed by the power of the thermal noise only. Here, let

$$\eta_i = \mu_i + \sigma^2 \quad (i = 1, 2, \dots, N) \quad (2.29)$$

and the eigenvalues of co-variance matrix R_{xx} be

$$\eta_1 \geq \eta_2 \geq \dots \geq \eta_L > \eta_{L+1} = \dots = \eta_N = \sigma^2. \quad (2.30)$$

Therefore, one can estimate the number of waves L by calculating the number of eigenvalues larger than the power of the thermal noise. Methods to estimate the number of L have been reported in literatures such as the minimum description length (MDL) [31], however, we omit the description of those methods in this thesis for the sake of simplicity. It is assumed that the number of L is known for the remainder of this thesis.

Focusing on the eigenvalues which are similar to the power of the thermal noise, we get

$$R_{xx} \mathbf{e}_i = (\mathbf{A}\mathbf{S}\mathbf{A}^H + \sigma^2 I) \mathbf{e}_i = \eta_i \mathbf{e}_i = \sigma^2 \mathbf{e}_i \quad (i = L+1, 2, \dots, N) \quad (2.31)$$

and

$$\mathbf{A}\mathbf{S}\mathbf{A}^H \mathbf{e}_i = 0. \quad (i = L+1, 2, \dots, N) \quad (2.32)$$

Furthermore, matrix \mathbf{A} and \mathbf{S} are full rank matrix, gives

$$\mathbf{A}^H \mathbf{e}_i = 0. (i = L+1, 2, \dots, N) \quad (2.33)$$

Hence,

$$\mathbf{a}^H(\theta_l) \mathbf{e}_i = 0. \quad (i = L+1, 2, \dots, N, l = 1, 2, \dots, L) \quad (2.34)$$

We understand from Eq. (2.35), that the eigenvectors corresponding to the eigenvalues that are equal to that of the thermal noise are orthogonal to the steering vector of the arriving waves. The eigenvectors can be regarded as the antenna weight vectors.

The eigenvectors $\{\mathbf{e}_1, \mathbf{e}_2, \dots, \mathbf{e}_K\}$ are orthogonal to each other, hence can be regarded as a Hermitian space with K dimension. We can separate the signal and noise into two separate spaces given by

$$S = \text{span}\{\mathbf{e}_1, \mathbf{e}_2, \dots, \mathbf{e}_L\} \quad (2.35)$$

$$Z = \text{span}\{\mathbf{e}_{L+1}, \mathbf{e}_{L+2}, \dots, \mathbf{e}_N\} \quad (2.36)$$

On the other hand, from Eq. (2.36) we understand that,

$$S' = \text{span}\{\mathbf{a}(\theta_1), \mathbf{a}(\theta_2), \dots, \mathbf{a}(\theta_L)\}, \quad (2.37)$$

Also corresponds to an L dimension sub-space which is orthogonal to sub-space Z . Hence, S and S' create a space which is orthogonal to Z . In other words, the eigenvalues $\{\mathbf{e}_1, \mathbf{e}_2, \dots, \mathbf{e}_K\}$ and steering vector $\{\mathbf{a}(\theta_1), \mathbf{a}(\theta_2), \dots, \mathbf{a}(\theta_L)\}$ are in the same space. The S and Z are called the signal and noise sub-spaces, respectively.

The MUSIC pseudo spectrum is given by [32]

$$P_{\text{MU}} \triangleq \frac{1}{\sum_{i=L+1}^K |\mathbf{e}_i^H \mathbf{a}(\theta)|^2} \times \mathbf{a}^H(\theta) \mathbf{a}(\theta) \quad (2.38)$$

$$= \frac{\mathbf{a}^H(\theta) \mathbf{a}(\theta)}{\mathbf{a}^H(\theta) \mathbf{e}_z \mathbf{e}_z^H \mathbf{a}(\theta)} \quad (2.39)$$

$$\mathbf{e}_z \triangleq [\mathbf{e}_{L+1}, \dots, \mathbf{e}_z] \quad (2.40)$$

P_{MU} will be maxed when θ satisfies Eq. 2.40. Searching the spectrum for L peaks gives the solution for $\{\theta_1, \dots, \theta_L\}$.

B. Extended MUSIC for two-dimensional estimation and its application to joint DOD and DOA estimation in MIMO radar.

We have presented the principle of a one dimensional MUSIC algorithm in the previous subsection. The algorithm was derived based on antenna system using a uniform linear array which was assumed to be placed along either the x or y -axis. In order to describe the application of a two-dimensional in MIMO radar, we will first show the extended version of MUSIC to a rectangular array antenna. For example, extending the array to a rectangular array consisting M elements along the x -axis and N elements along the y -axis allows the estimation of angle of arrival observed from a two dimensional plane for more accurate localization purposes [32, 33]. Similar principle was also applied to linear array aligned along the x and z -axes, or a circular array for azimuth and elevation angle of arrival estimation in [34, 35].

For the derivation of a basic two-dimensional MUSIC algorithm using the rectangular array, let the spacing along the x and y -axes be d_x and d_y , respectively. The DOA of the l^{th} source is given as θ_x and θ_y . Here, the phase difference at the n^{th} antenna along both of the x and y -axes are given by

$$\phi_x(\theta_x) = \frac{2\pi}{\lambda} (n-1) d_x \sin \theta_x \quad (2.41)$$

$$\phi_y(\theta_y) = \frac{2\pi}{\lambda} (n-1) d_y \sin \theta_y. \quad (2.42)$$

Hence, from the principles derived in [32], the array manifold vector in the two dimension case is given by

$$\mathbf{a}(\theta_x, \theta_y) = [\mathbf{a}_x(\theta_x) \mathbf{a}_y(\theta_y)^H], \quad (2.43)$$

where

$$\mathbf{a}_x = e^{j \frac{2\pi}{\lambda} (n-1) d_x \sin \theta_x} \quad (l = 1, \dots, L, n = 1, \dots, N) \quad (2.44)$$

$$\mathbf{a}_y = e^{j \frac{2\pi}{\lambda} (n-1) d_y \sin \theta_y} \quad (l = 1, \dots, L, n = 1, \dots, N). \quad (2.45)$$

$\mathbf{a}(\theta_x, \theta_y)$ is hereby resembles an $N^2 \times 1$ vector. Therefore, the two-dimensional MUSIC pseudo spectrum can be constructed as

$$P_{2\text{DMUSIC}}(\theta_x, \theta_y) = \frac{\mathbf{a}(\theta_x, \theta_y)^H \mathbf{a}(\theta_x, \theta_y)}{\mathbf{a}(\theta_x, \theta_y)^H \mathbf{e}_z \mathbf{e}_z^H \mathbf{a}(\theta_x, \theta_y)}, \quad (2.46)$$

where \mathbf{e}_z is given by Eq. (2.32). By searching the $P_{2\text{DMUSIC}}$ for the L peaks gives us the two-dimensional estimation results.

The derived two-dimensional MUSIC can also be applied in the case of MIMO radar to jointly detect the DOD and DOA. Consider the case of MIMO radar detecting L targets as shown in Fig. 2.4, where M and N are the number of transmitting and receiving antennas, and ϕ and θ are the DOD and DOA, respectively. The transmitting and receiving steering vectors are given by \mathbf{a}_t and \mathbf{a}_r , which depends on the antenna array geometry and spacing used by the MIMO radar. Adopting the virtual array concept of the MIMO radar, the array manifold vectors are expressed by the convolution of the transmitting and receiving steering vectors. Following steps given in [36, 37], the resulting array manifold vector becomes

$$\mathbf{a}(\phi, \theta) = [\mathbf{a}_t(\phi) \otimes \mathbf{a}_r(\theta)], \quad (2.47)$$

where \otimes denotes the kronecker product operator. Using the same principle as Eq. (2.46), the two-dimensional MUSIC (also denotes as two-way MUSIC) pseudo spectrum is given by

$$P_{2\text{WMUSIC}}(\theta_x, \theta_y) = \frac{(\mathbf{a}_t(\phi) \otimes \mathbf{a}_r(\theta))^H (\mathbf{a}_t(\phi) \otimes \mathbf{a}_r(\theta))}{(\mathbf{a}_t(\phi) \otimes \mathbf{a}_r(\theta))^H \mathbf{e}_z \mathbf{e}_z^H (\mathbf{a}_t(\phi) \otimes \mathbf{a}_r(\theta))}, \quad (2.48)$$

Similar as in Eq. (2.46), searching the peak of $P_{2\text{WMUSIC}}$ gives us the location of the target in terms of the DOD and DOA.

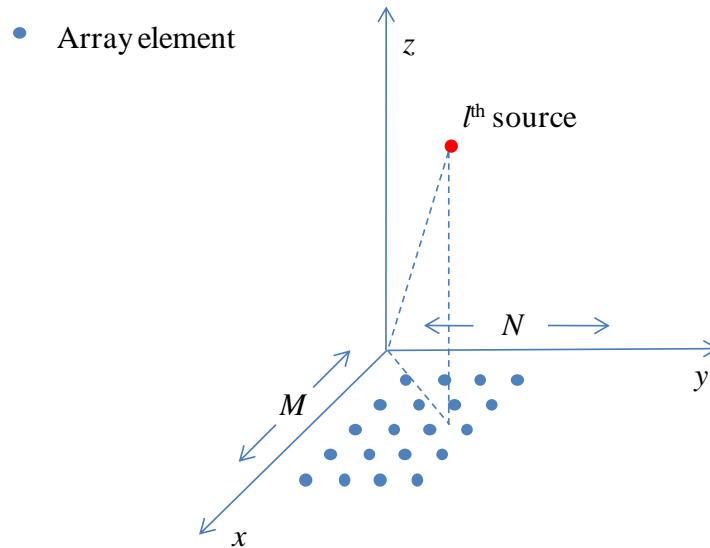


Fig. 2.3. Rectangular array antenna in angle of arrival estimation.

C. Application of two-dimensional MUSIC in joint estimation of DOD and DOA for wideband signal MIMO radar.

In general, the precision of direction of arrival estimation degrades with increasing bandwidth of the signal, since the array manifold vectors as given by Eq. (2.23), is a function with respect to the wavelength. Nevertheless, MUSIC algorithm plays an importance role in the direction estimation of wideband signals due to its high resolution and multi-target estimation capabilities. Various MUSIC algorithm of wideband signals have been developed for applications such as radar, sonar, seismology and communication. One of the basic approach is that the direction of arrival at different frequency components or sub-bands to formulate the final DOA estimation [38, 39]. However, these non-coherent processing techniques does not obtain sufficient. Improved technique based on coherent combination of data from multiple narrowband signals can be found in [40], for example by using a spatial resampling and an interpolated virtual array. If a large number of snapshots are given, these wideband direction estimation methods obtain sufficient performances. We proposed a MUSIC-based direction estimation method using a non-parametric approach for MIMO radars using wideband signals which will be described in Chapters 4 and 5.

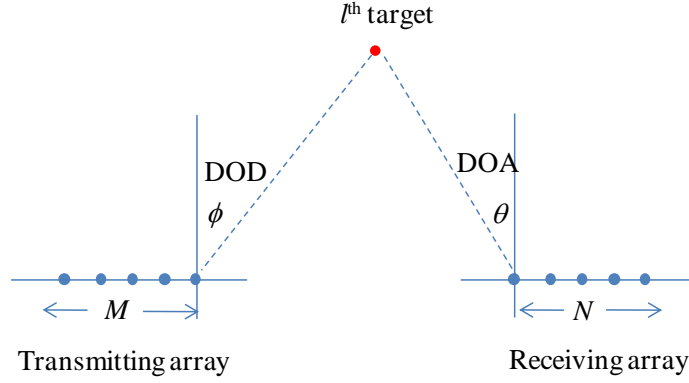


Fig. 2.4. Example of a MIMO radar array configuration in joint DOD and DOA estimation.

D. MUSIC Algorithm for Estimation of Time of Arrival.

The classical MUSIC algorithm can also be modified to estimate the time of arrival of multiple waves [41, 42]. As described in [42], the technique for estimating time of arrival using MUSIC requires signal of multiple frequencies impinging the receiving reference antenna. Each frequency component of the signal impinging the reference antenna yields slightly different phase information due to the different wavelength λ factor, hence a time delay vector can be constructed using these information. This time delay vector can be exploited in a similar way as the steering vector for time of arrival detection. To derive the MUSIC spectrum of time of arrival, consider a scenario where L waves are impinging a reference antenna as shown in Fig. 2.5, where the receiving signal consists of multiple frequency components swept over the signal bandwidth in interval Δf . The complex voltage $\mathbf{v}(f)$ of the receiving signal vector at frequency f is

$$\mathbf{v}(f) = D(f) \sum_{l=1}^L F_l \exp(-j2\pi f \tau_l), \quad (2.49)$$

where F_l is the complex amplitude of the l^{th} wave, τ_l is the propagation time, and $D(f)$ is the function of the directivity of the receiving antenna at frequency f . Thus, the receiving signal can be expressed by

$$\begin{aligned} \mathbf{x}(f) &= \frac{\mathbf{v}(f)}{D(f)} \\ &= \sum_{l=1}^L F_l \exp(-j2\pi f \tau_l). \end{aligned} \quad (2.50)$$

Considering thermal noise, Eq. (2.50) becomes

$$\mathbf{x}(f) = \sum_{l=1}^L F_l \exp(-j2\pi f \tau_l) + \mathbf{z}(f). \quad (2.51)$$

Furthermore, sweeping the frequency with frequency interval Δf along an array with N samples gives the below equations:

$$\mathbf{x} = [X_1, X_2, \dots, X_M]^T \quad (2.52)$$

$$\mathbf{A} = [\mathbf{a}^L(\theta_1), \dots, \mathbf{a}^L(\tau_l), \dots, \mathbf{a}^L(\tau_L)] \quad (2.53)$$

$$\mathbf{a}^L(\theta_l) = [\exp(-j2\pi f_1 \tau_l), \dots, \exp(-j2\pi f_k \tau_l), \dots, \exp(-j2\pi f_K \tau_l)] \quad (2.54)$$

$$\mathbf{f} = [F_1, F_2, \dots, F_M]^T \quad (2.55)$$

$$\mathbf{z} = [N_1, N_2, \dots, N_M]^T. \quad (2.56)$$

Eq. (2.54) represents the steering vector of the array, which is also referred to as the time delay vector. We notice here that the time delay vector yields similar form as the steering vector in Eq. (2.22) and hence, can be utilized by MUSIC algorithm to estimate the time of arrival of impinging waves. The correlation matrix and SVD gives us

$$R_{xx} = E[\mathbf{x}(f)\mathbf{x}(f)^H] = \mathbf{A}\mathbf{S}\mathbf{A}^H + \sigma^2\mathbf{I}, \quad (2.57)$$

Similar to the conventional MUSIC algorithm, by exploiting the orthogonality between the eigenvectors and the time delay vector, the MUSIC spectrum can be derived as

$$P_{\text{MU}}(\tau) = \frac{\mathbf{a}^H(\tau)\mathbf{a}(\tau)}{\mathbf{a}(\tau)\mathbf{e}_z\mathbf{e}_z^H\mathbf{a}(\tau)}, \quad (2.58)$$

where the peaks of the spectrum corresponds to the time of arrival τ of the impinging waves. Note here that the time delay vector was used instead of the steering vector in the case of conventional MUSIC.

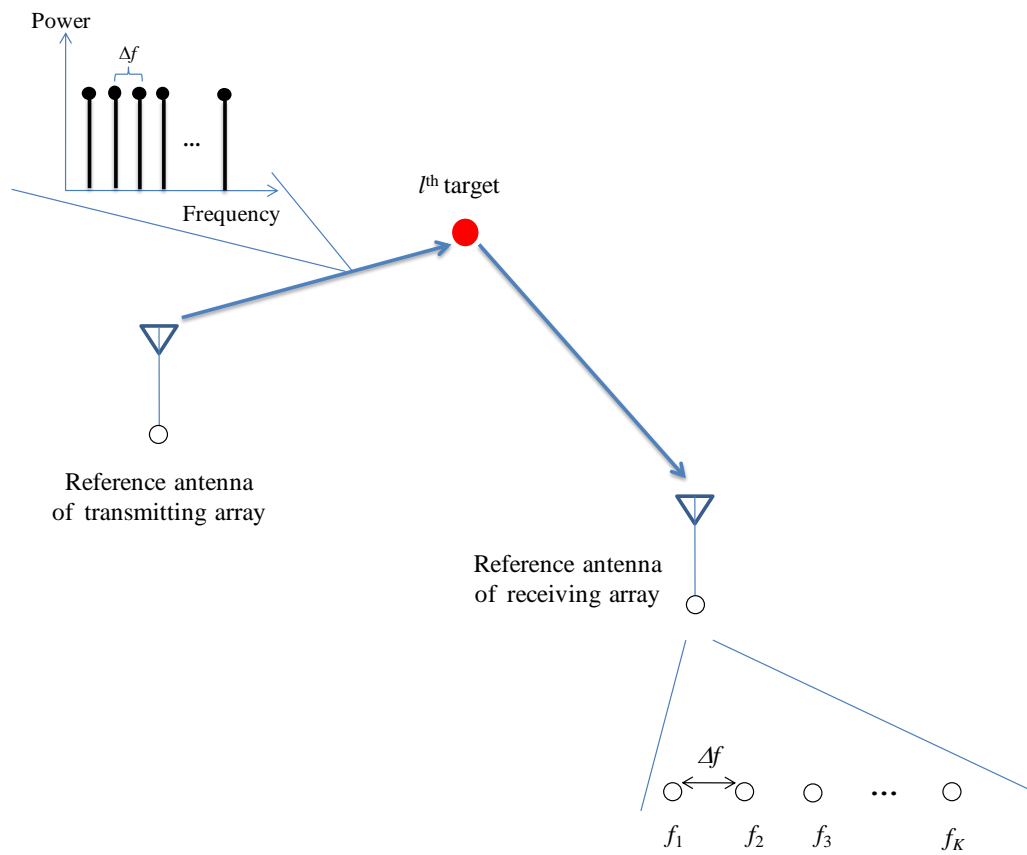


Fig. 2.5. Transmission of signal with multiple frequency components between the transmitting and receiving reference antennas.

Chapter 3

DETECTION PERFORMANCE OF M-SEQUENCE-BASED MULTIPLE-INPUT MULTIPLE-OUTPUT RADAR SYSTEMS

3.1. INTRODUCTION

This chapter discusses the detection performance of MIMO radars considering jitter effects. The study concerns the spatial MIMO radars, which is a radar system that uses multiple antennas that are widely separated in space. The spatial MIMO radar may consist of large numbers of transmitters and receivers distributed in the system, thus enhancing the system complexity compared to conventional SISO systems. This worsens the effects of hardware imperfections such as coordination of transmitting sensors, communication with the joint processing unit, and synchronization errors on the system performance, particularly in MIMO radars utilizing widely distributed antennas.

Several works evaluating the performance of MIMO radar while considering some of system imperfections were reported. For example, Chen *et al.* pointed out that calibration accuracy of antenna position in a MIMO array is essential to achieve good target location estimation [43]. Furthermore, Akcakaya *et al.* studied the performance of a coherent MIMO radar system under phase synchronization error effects due to modeling errors [44]. It was shown that synchronization mismatch degraded the detection performance severely, and an adaptive energy distribution technique to compensate the losses in signal to noise ratio (SNR) was proposed.

In this chapter, we discuss the detection performances of MIMO radar systems with widely separated antennas under ideal conditions, and investigate the influence of jitters on the radar system. The motivation of this work was to evaluate the system performance under the influence of hardware imperfections (presence of jitter), even in the absence of modeling errors. Despite the fact that radar systems suffer performance degradation in various aspects due to jitter, to the authors' knowledge, the evaluation of jitter effects on the detection performance of MIMO radar systems have not been quantitatively evaluated. Furthermore, most other reports took the approach of using Monte Carlo simulations, where random data were used as the MIMO radar signal, while assuming that the orthogonality condition was achieved in some way. The present study adopted a deterministic simulation in the time domain to model an m -sequences-based MIMO radar signal. Implementation of m -sequence codes in the simulation allows actual separation of transmitting signal entering each of the receiving antennas. This enabled us to directly evaluate the effects of jitter on the system

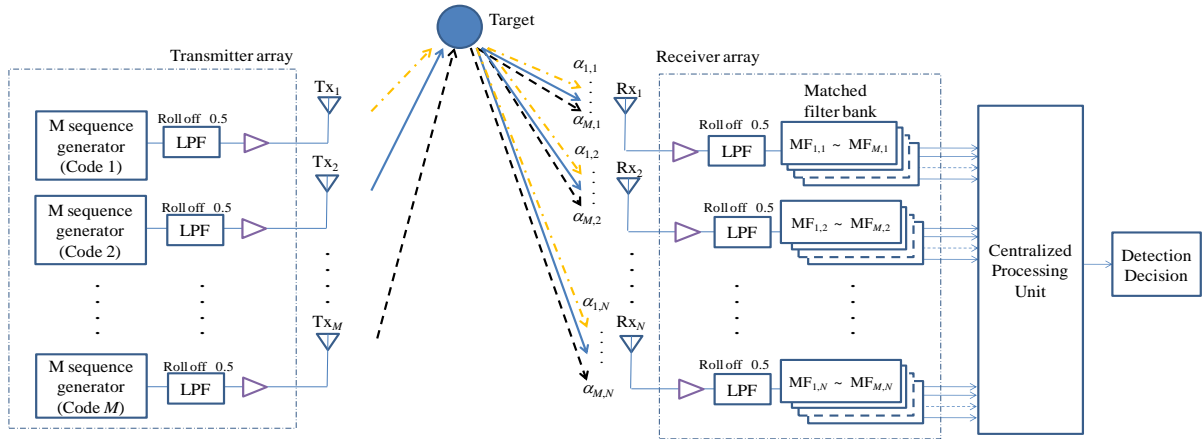


Fig. 3.1. Block diagram of the equivalent baseband model of MIMO radar system.

performance, since the statistical characteristics of the m -sequences (and their cross-correlation products) are different from randomly generated data. In addition, we developed a MIMO radar testbed from commercially available microwave components for experimental evaluations. We will describe the simulation model, conditions and results in the next section. We will also explain our developed MIMO radar testbed, and some results of experimental evaluation in a radio anechoic chamber.

3.2. M-SEQUENCE-BASED MULTIPLE-INPUT MULTIPLE-OUTPUT RADAR SIGNAL MODEL

In this section, we derive the MIMO radar signal model for our numerical simulations. The block diagram of the simulation model is depicted in Fig. 3.1. A MIMO radar system with M transmitters and N receivers was constructed in the equivalent baseband region. The system employs m -sequences as the transmit signals, generated from 7-stage shift registers. Although various types of orthogonal codes are available in literature, such as Gold, Hadamard and Walsh codes [8], we opted for m -sequences due to their simple generation procedure, and good cross-correlation characteristics, subject to proper code selection. Mathematically, the baseband representation of the signal arriving at the n^{th} receiver can be expressed by

$$r_n(t) = H_{0/1} \sum_{m=1}^M \alpha_{m,n}(\sigma) s_m(t - \tau_{m,n}) + z_n(t), \quad (3.1)$$

where $H_{0/1}$ is 0 or 1 depending on the absence or presence of target, respectively; s_m is the m^{th} transmitted signal, $\tau_{m,n}$ is the delay occurring during the path between the m^{th} transmitter, target and the n^{th} receiver, z_n is the thermal noise, and $\alpha_{m,n}(\sigma)$ is the transmission coefficient that accounts for the RCS distribution of the target.

Taking into account all receiving signals entering the receiver, the output of the h^{th} matched filter can be derived by

$$\begin{aligned} x_{h,n} &= r_n(t) * s_h(t) \\ &= H_{0/1} \sum_{m=1}^M \alpha_{m,n}(\sigma) s_m(t - \tau_{m,n}) \otimes s_h(t) + z_n(t) \otimes s_h(t) \\ &= H_{0/1} \alpha_{h,n}(\sigma) R_h(t - \tau_{h,n}) \\ &\quad + H_{0/1} \sum_{\substack{m=1 \\ m \neq h}}^M \alpha_{m,n}(\sigma) R_{m,h}(t - \tau_{h,n}) + n_{h,n}(t), \end{aligned} \quad (3.2)$$

where $*$ denotes a convolutional operation, s_h is the reference signal at the h^{th} matched filter, R_h is the autocorrelation function of s_m , $R_{m,h}$ is the cross-correlation function of s_m with s_h , and $n_{h,n}$ is the resulting noise after the h^{th} matched filter at the n^{th} receiver. Consequently, considering a MIMO radar system with M transmitters and N receivers, a total of M matched filters are adopted at each receiver, providing MN outputs, arranged as

$$\mathbf{X} = \begin{bmatrix} x_{11} & x_{12} & \cdots & x_{1N} \\ x_{21} & x_{22} & \cdots & x_{2N} \\ \vdots & \vdots & \ddots & \vdots \\ x_{M1} & x_{M2} & \cdots & x_{MN} \end{bmatrix}, \quad (3.3)$$

and can be re-arranged into a vector as

$$\mathbf{x} = [x_{11}, \dots, x_{1M}, x_{21}, \dots, x_{2M}, \dots, x_{N1}, \dots, x_{MN}]^T, \quad (3.4)$$

where $[\cdot]^T$ is the transpose operation. The resulting signal matrix is then jointly processed at a centralized processing unit, returning a detection decision based on an appropriate threshold. The detection performance of the MIMO radar systems depend on the type of processing scheme applied to the receiving signal matrix, which will be explained in the subsequent sub-section.

3.3. MIMO RADAR SIGNAL PROCESSING SCHEMES

This thesis considers three types of joint signal processing schemes which have been proposed in MIMO radar through previous literatures [6], namely the non-coherent MIMO, the re-phased netted radar (RPNR), and the decentralized radar network (DRN) processing. The non-coherent MIMO processing (afterward termed ‘‘MIMO’’) has been proposed in many initial literatures on MIMO radar as a general scheme to process the receiving signals in a non-coherent way, where a generalized likelihood ratio test is utilized. The RPNR and DRN were discussed here due to the fact that these types of processing can be applied to the same radar network while keeping its geometry fixed.

The non-coherent MIMO processing scheme is derived from the optimal Neyman-Pearson detector, where a likelihood ratio test is formulated between two hypotheses H_1 and H_0 , corresponds to the presence and absence of the target, respectively. The likelihood ratio test is therefore given by

$$\log \frac{p(\mathbf{r}(t)|H_1)}{p(\mathbf{r}(t)|H_0)} \underset{H_0}{\overset{H_1}{\geq}} \lambda, \quad (3.5)$$

where $p(\mathbf{r}(t)|H_1)$ and $p(\mathbf{r}(t)|H_0)$ are the probability density functions of the observation vector ($\mathbf{r} = [r_1, \dots, r_N]^T$) under the respective hypotheses. Following similar steps described by Fishler et al. [3], when the detector has full knowledge of the energy contained in \mathbf{x} and the noise variance, it was shown that the detector can be given by

$$\|\mathbf{x}\|^2 \underset{H_0}{\overset{H_1}{\geq}} \lambda, \quad (3.6)$$

where $\|\cdot\|$ denotes the vector norm, and λ is an appropriate threshold to keep a desired probability of false alarm (P_{fa}). This processing scheme is non-coherent since the detection is based on the received signal power alone.

On the other hand, the RPNR performs a coherent summation of the signals after they are processed through the bank of matched filters. The signals phases were re-aligned in such a way so that the summation maximizes the SNR. The detection in this type of processing is determined by

$$\left| \sum_{k=1}^N \sum_{h=1}^M x_{h,n} \exp(-j\phi_n) \right|^2 \underset{H_0}{\overset{H_1}{\geq}} \lambda, \quad (3.7)$$

where the ϕ_n is the phase of the desired signal arriving at the n^{th} receiver, when target is present. This type of processing is challenging to be implemented, since it requires the prior knowledge of the

signal path lengths. This may be obtained for example through utilization of target localization algorithm in pre-detection stage. The RPRN provides the upper bound of detection performance, and is used as a benchmark with the other processing schemes.

The DRN scheme works in a decentralized way where it implements a two-stage approach of detection. All the transmitter-receiver pairs works separately to produce its own detection decision in the initial stage using non-coherent processing, and these results are subsequently fused at the central processing unit. The output of the first stage of threshold processing at the n^{th} receiver is given by

$$v[n] = \begin{cases} 1, & \left| \sum_{h=1}^M x_{h,n} \right|^2 \geq \lambda \\ 0, & \text{otherwise} \end{cases} \quad (3.8)$$

The second stage applies another threshold processing on the output of all receivers, hence giving the detection by

$$\sum_{n=1}^N v[n] \geq L, \quad (3.9)$$

where L is an appropriate threshold to achieve the chosen P_{fa} . An illustration of the three types of processing scheme is depicted in Fig. 3.2.

It can be observed that all processing schemes utilize MN number of receiving signals for detection. This implies that the MIMO radar system's performance is a function of MN . The value of MN has a direct impact on the total receiving signal power, hence the SNR. Therefore, when M is not equal to N , the P_d will yield similar trend to the case of M equals to N , however, with a shift in SNR, depending on the value of MN . For example, a 2×4 configuration would yield a poorer P_d compared to a 4×4 system, due to loss in SNR. For the sake of simplicity, simulations in this study were conducted in cases of M equals to N . The number of antenna will also have a direct impact on the P_d of the MIMO radar system, since it governs the total number of receiving signal, MN .

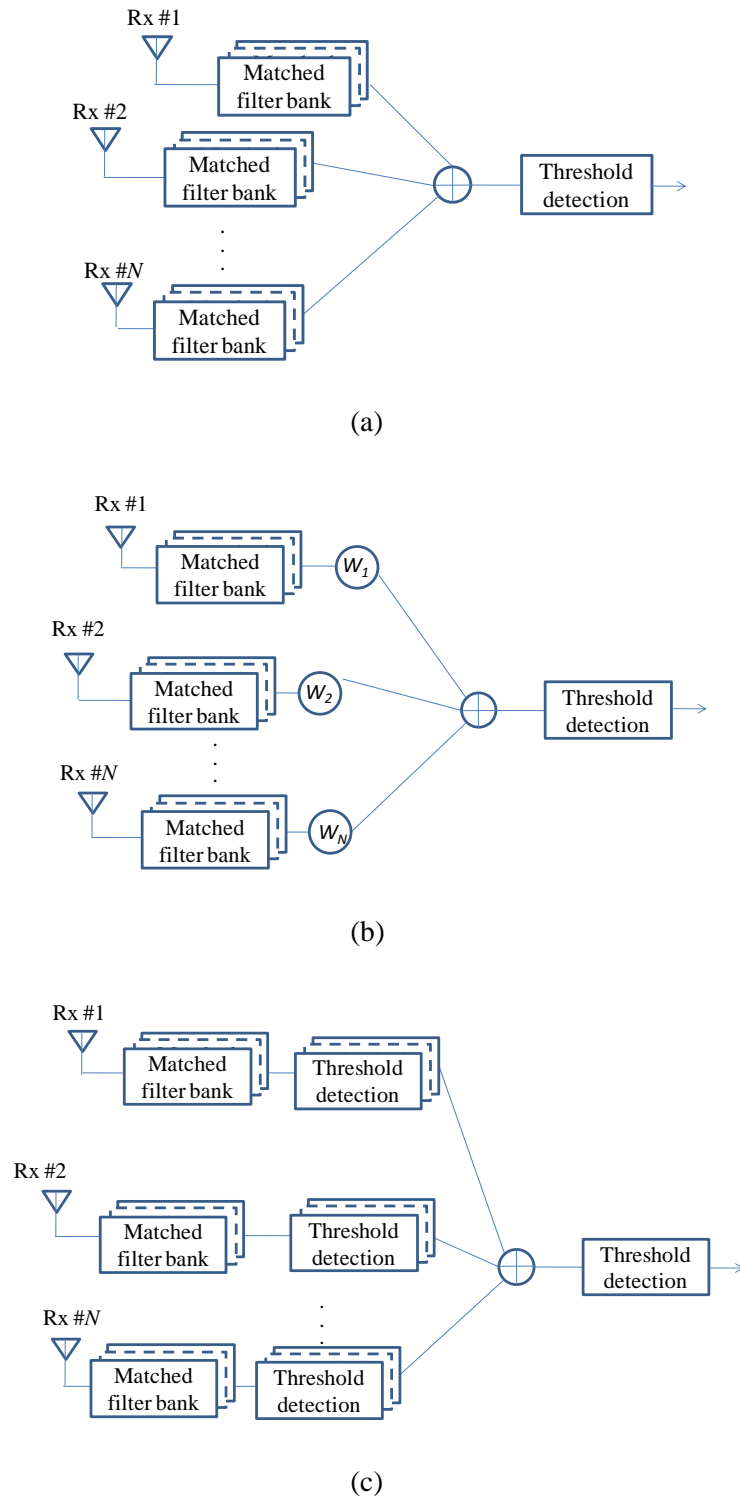


Fig. 3.2. Illustration of the three joint processing schemes us for the MIMO radar model used in this study: (a) MIMO, (b) RPNR, and (c) DRN processing schemes.

3.4. SIMULATION OF DETECTION PERFORMANCE

3.4.1. DETECTION PERFORMANCE IN IDEAL CONDITIONS

A simulation model was constructed to numerically investigate the detection performance of the m -sequence-based MIMO radar system in ideal cases, assuming perfect synchronization between each of the respective transmitter and receiver pairs. Major parameters of the simulation model are summarized in Table 3.1. Each transmitter emits a unique m -sequence which was generated by a 7-step shift registers. In order to guarantee the orthogonality between these signals, utilization of codes with low cross-correlation properties is essential. In this study, we chose a set of preferred pair m -sequences [8] as listed in Table 3.1. The signals are sampled at 2.5 GS/s, and filtered to occupy 500 MHz of bandwidth. Since this is an equivalent baseband model, the signal is centered at DC. The 500 MHz bandwidth was chosen so that we could have a parallel performance comparison with our developed MIMO radar testbed presented later in this chapter. In this study, a fluctuating RCS corresponding to Swerling I model [2] was considered, where $\alpha_{m,n}$ is represented by random variables following Chi-squared probability density function (PDF) with two degrees of freedom derived by

$$p(\sigma) = \frac{1}{\sigma_{av}} \exp\left(-\frac{\sigma}{\sigma_{av}}\right), \quad (3.10)$$

where σ_{av} is the average RCS over all target fluctuations. The Swerling I model was chosen since it is well known to approximate the RCS distribution of a moving airplane. At every receiver, a matched filter corresponding to each transmitting sequence was implemented.

The simulated MIMO radar waveforms and their cross-correlation properties are depicted in Fig. 3.3, illustrating the importance of proper code selection in order to guarantee orthogonality. The detection performance of the MIMO radar system was evaluated against varying SNR, using the three signal processing schemes explained in the previous section, namely: MIMO, RPNR and DRN. For the sake of simplicity, we simulated the detection performance using $M = N$, varying the configuration from 2×2 until 4×4 . The SNR is defined as the ratio of the average of the total signal power, to the total noise power at the receiver. In the simulations, the P_{fa} was fixed at 10^{-6} for all cases.

Table 3.1.
Simulation parameters.

Parameters	Description
Sampling rate	2.5 GS/s
Filter roll-off factor	0.5
Oversampling	5
Bandwidth	500 MHz
MIMO configuration	2×2, 3×3, 4×4
M-sequence (code length)	Order of 7 (127)
M-sequence code set	(7, 1) (7, 3, 2, 1) (7, 6, 3, 1) (7, 4, 3, 1)
Number of simulated data points in each iteration	100 000

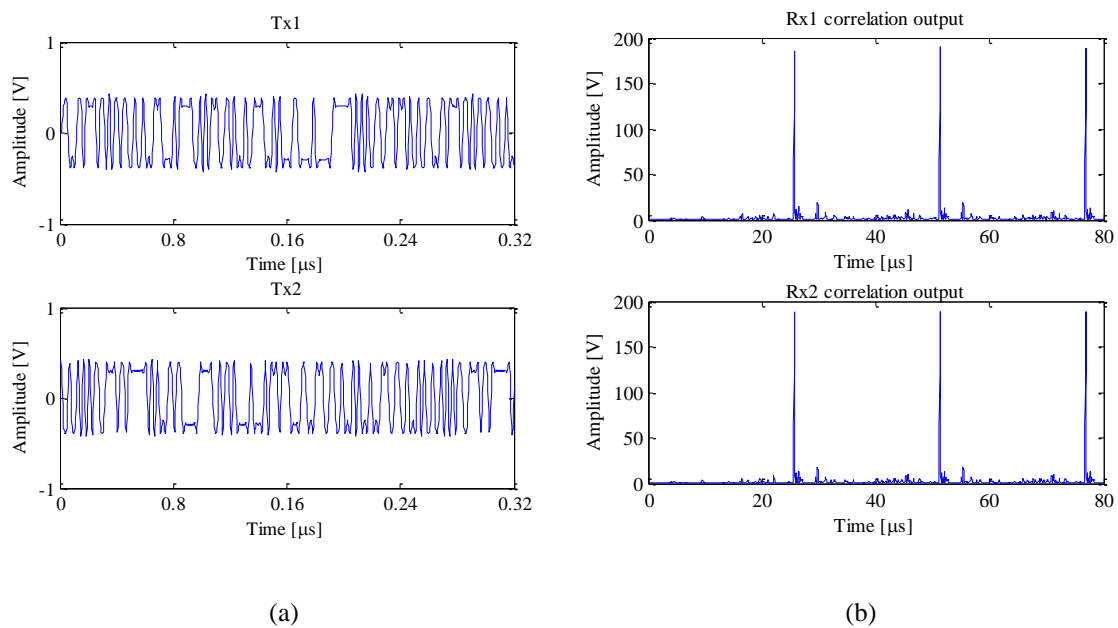


Fig. 3.3. Simulated waveforms in the time domain (SNR = 10 dB): (a) Transmitting signals with different m-sequences and (b) matched filter output.

Here we plotted the P_{fa} curve of each processing scheme as a function of threshold value where only white Gaussian noise with zero mean and normalized variance is input to the receives. Figure 3.4 shows the simulated P_{fa} of the MIMO radar for each of the processing scheme used compared to their theoretical curves. Fig. 3.4 was simulated to reproduced the curves plotted in [6]. The theoretical derivation of the P_{fa} for each processing scheme is

$$\sum_{n=1}^{MN} |z_n|^2 \geq \lambda_{\text{MIMO}} \quad (3.11)$$

for the MIMO case,

$$\left| \sum_{n=1}^N \sum_{h=1}^M z_{h,n} \right|^2 \geq \lambda_{\text{RPNR}} \quad (3.12)$$

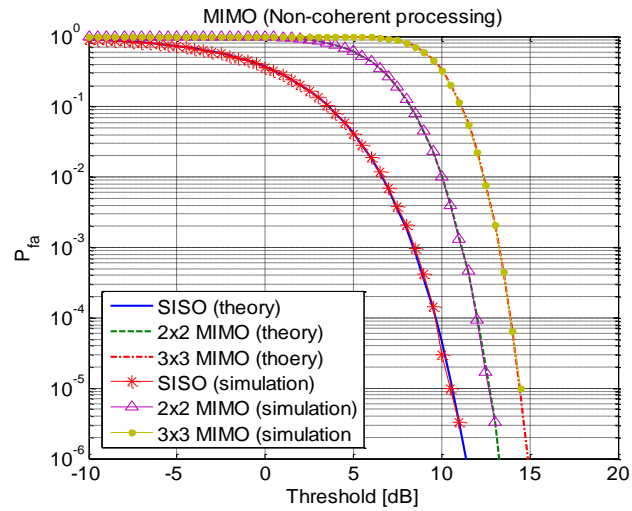
for the RPNR case, and

$$\sum_{n=1}^N v[n] \geq L, \quad (3.13)$$

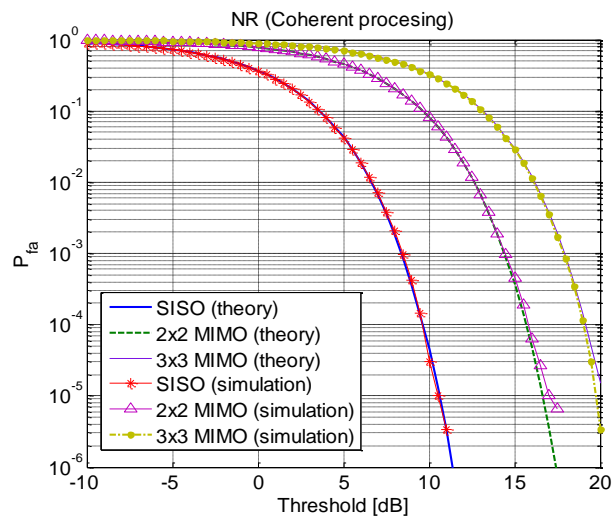
$$v[n] = \begin{cases} 1, & \left| \sum_{h=1}^M z_{h,n} \right|^2 \geq \lambda_{\text{DRN}} \\ 0, & \text{otherwise} \end{cases} \quad (3.14)$$

for the DRN case, where z is the thermal noise components at the n th receiver, $z_{h,n}$ is the thermal noise components at the h^{th} matched filter at the n^{th} receiver.

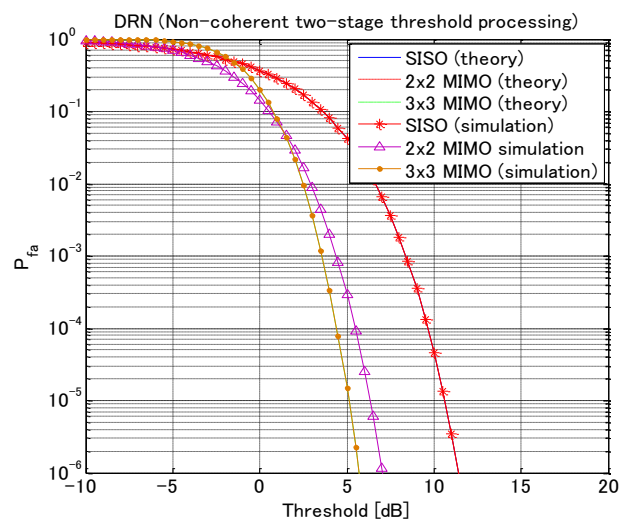
The figures could also be interpreted to represent thresholds required to achieve a chosen P_{fa} for a number of process signals. Observing at $P_{fa} = 10^{-6}$, it was shown that the non-coherent schemes such as the MIMO and DRN processing had performance advantage than coherent RPNR scheme, since they require a lower threshold to achieve the same P_{fa} as their counterpart. For instance, as depicted in Fig. 3.4 (a) when using a 2×2 MIMO radar, the value of threshold required to achieve $10^{-6} P_{fa}$ are 10 dB for MIMO, 12 dB for DRN and 15 dB for RPNR. Furthermore, in a 4×4 MIMO radar, similar trend was observed.



(a)



(b)



(c)

Fig.3.4. Probability of false alarm for different processing scheme in MIMO radar: (a) MIMO (b) NR, and (c) DRN.

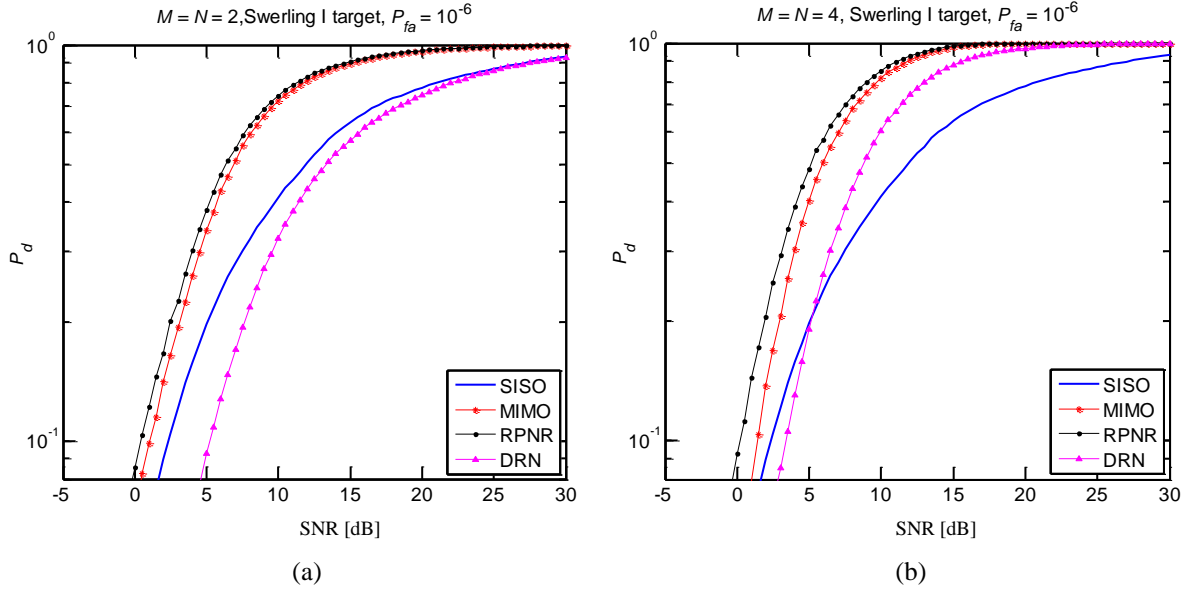


Fig. 3.5. Probability of detection of the simulated MIMO radar system in ideal cases: (a) 2×2 and (b) 4×4 configurations.

The detection performance versus SNR was plotted in Fig. 3.5. It is shown that all processing schemes yielded improvements in detection probability compared to the SISO case. At the same SNR, the RPNR yielded the best performance due to the processing gain obtained from the phase information of the signals. The MIMO processing scheme performed almost equally with RPNR, with not much difference at high SNR region, for example at $\text{SNR} = 15$ dB which corresponded to $P_d = 0.8$. The DRN yielded the worst performance, however, the P_d improved with increasing transmitter and receiver pairs, as shown in the 4×4 configuration in Fig. 3.5 (b). These P_d trends obtained from our simulation agree well with the trends showed from numerical results reported in [6], although with shifts in SNR.

3.4.2. DETECTION PERFORMANCE CONSIDERING JITTER INFLUENCE

This section presents the detection performance of MIMO radar system considering the presence of jitter in the radar system. In our study, we considered two types of jitter; namely time and phase jitter. Time jitter is defined as the uncertainty of sampling points at the receiver, due to timing impairments such as noise and inter-symbol interference, attributed to jitters in the universal clock of the system, affecting all signal processing operations that are driven by the system's clock. On the other hand, the phase jitter exists as the instability of the frequency generated by the local oscillators

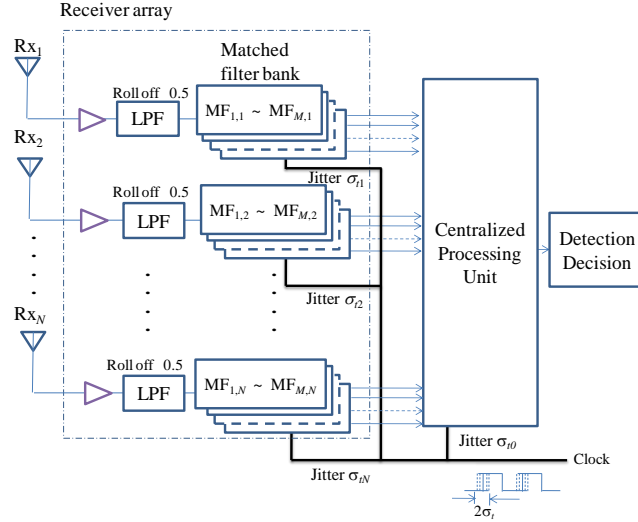


Fig. 3.6. Simulated model of time jitter in the MIMO radar receiver.

at the radar receivers. The effects of time and phase jitter were evaluated separately to provide a deeper insight on their effects on the system’s performance.

A. Simulation of Time Jitter Effects on the Detection Performance of MIMO Radar Systems.

The timing jitter was modeled in the time domain as a random jitter. The system’s clock samples at $T + \varepsilon_k$, where T was the actual clock edge, and ε_k was the variation in spacing due to time jitter. The ε_k was modeled to yield random values following a Gaussian distribution, with zero mean and standard deviation σ_t of 0.1, to 1% of the ideal clock period (5 to 500 ppm). The Gaussian assumption of the jitter distribution was supported by the fact that the primary source of the random jitter was the thermal noise; and according to the central limit theorem, the summation of many uncorrelated noise sources, regardless of their distributions, approaches a Gaussian distribution [45, 46]. Considering that the MIMO radar system consisted of multiple receivers in a widely separated location, independent timing jitter was modeled in each of the receiver, as depicted in Fig. 3.6.

Figure 3.7 illustrates the probability density function of the modeled time jitter with different values of standard deviation. It can be observed in the figure that at the sampling rate used in the simulation model, σ_t of 0.1 and 1 % corresponded to standard deviations of 0.4 and 4 ps in the time domain, respectively. These values of σ_t were chosen in similar order to standard jitter values in most high speed applications such as described in [47]. It was assumed that the transmitter side was not subject to time jitter, since it can be represented by the jitter at the receivers. An example of the eye pattern of a receiving signal with and without time jitter is shown in Fig. 3.8. It can be observed in

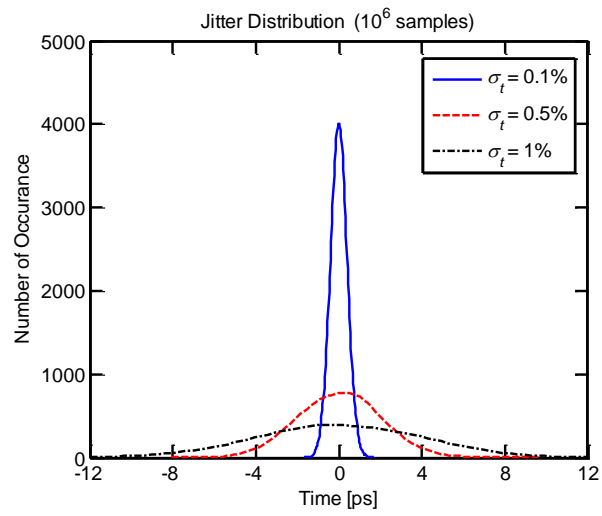


Fig. 3.7. Modeled time jitter distribution with different value of σ_t .

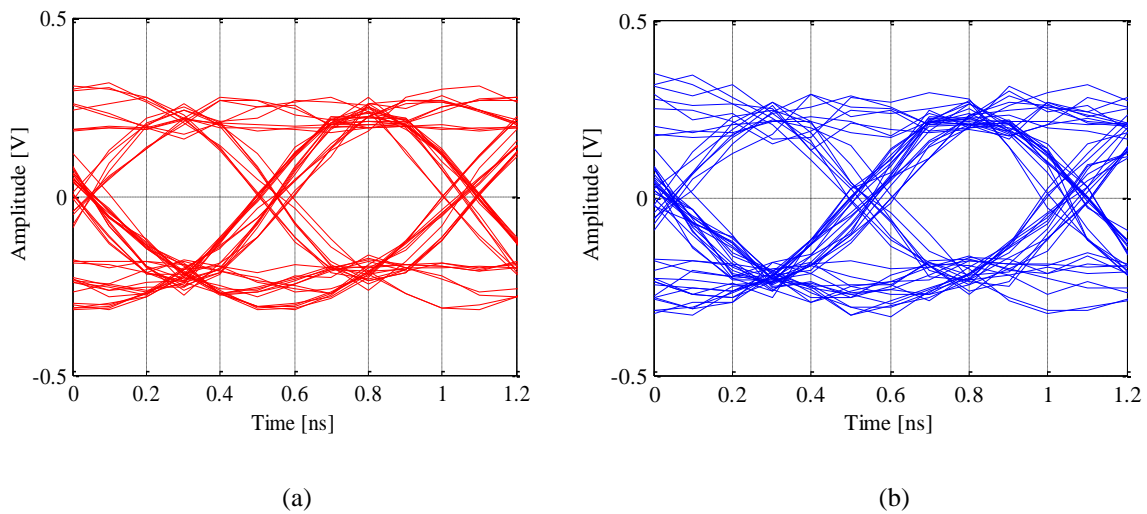


Fig. 3.8. Eye pattern plots of a receiving signal (roll-off factor 0.5, SNR = 20 dB): (a) no jitter and (b) $\sigma_t = 1\%$.

Fig. 3.8 (b) that the time jitter influenced the sampling points of the signal, and hence produced a distorted eye pattern plot.

The detection performance of the simulated MIMO radar system under the presence of jitter was presented in terms of probability of detection (P_d) versus SNR, for all type of processing schemes. The SNR here was defined by the ratio of the mean of the total signal power to the total noise power at the receiver. In the simulations, the P_{fa} was fixed at 10^{-6} for all cases.

The P_d curves in the presence of time jitter are presented in Figs. 3.9 and 3.10, while varying σ_t from 0.1 to 1% of the ideal clock. In the 2×2 case shown in Fig. 3.9 (a), negligible performance degradation was observed when $\sigma_t = 0.1\%$. However, when significant amount of jitter is present, as in the case of $\sigma_t = 1\%$, the RPNR performance degraded significantly. This is evident in Fig. 3.9 (b), where a loss of 6 dB in SNR can be observed at $P_d = 0.8$. The degradation was attributable to inaccurate sampling during the re-phasing of the receiving signal due to timing jitter. In this particular case, the MIMO processing only suffered negligible degradation, and as a result, it performed better than the RPNR. Fig. 3.10 (b) depicted similar trends in the 4×4 case, where RPNR requires 5 dB of extra SNR to perform equally with MIMO processing at $P_d = 0.8$. Here, it is also shown that the DRN outperformed the RPNR, since it did not exhibit significant degradation. The performance degradation of RPNR however will be bounded by the performance of the scheme without implementation of signal re-phasing at the receivers. The amount of P_d degradation for both 2×2 and 4×4 are plotted in Fig. 3.11. We can observe from the figure that the P_d degradation was higher with increasing SNR, indicating that the effects of jitter became dominant when the thermal noise in the system was insignificant.

It can be concluded that the presence of timing jitter had no significant impact on MIMO radar systems using the MIMO and DRN, which utilized a non-coherent detection in a joint, and decentralized processing, respectively. On the other hand, the RPNR processing scheme suffered significant degradation when large amount of jitter was present, since it required precise alignment of the receiving signals phase. This result demonstrated the robustness of the MIMO processing against the presence of time jitter, since they are based on statistical processing and the simulated amount of time jitter have less effects on the receive signal power. However, in either way, suppressing the time jitter's standard deviation below 0.1% of the ideal clock (0.4 ps in this case) was sufficient to prevent performance loss in either case of processing scheme used.

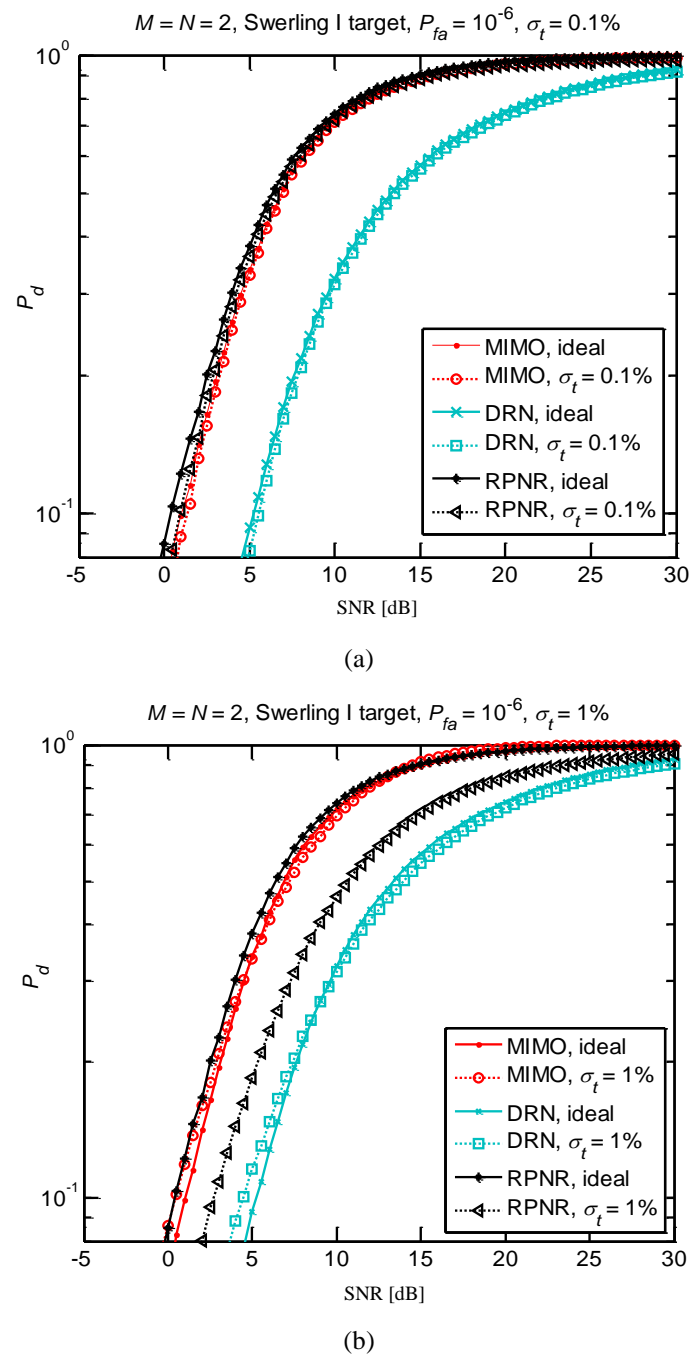


Fig. 3.9. Probability of detection under time jitter influence in a 2×2 configuration: (a) $\sigma_t = 0.1\%$ and (b) $\sigma_t = 1\%$.

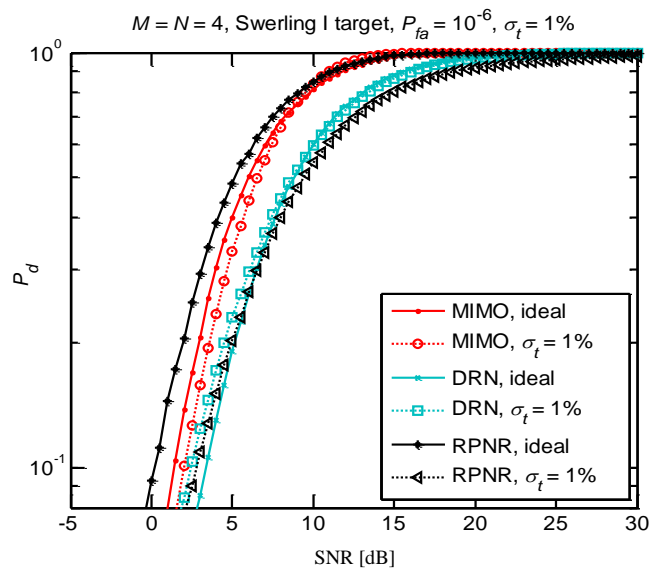
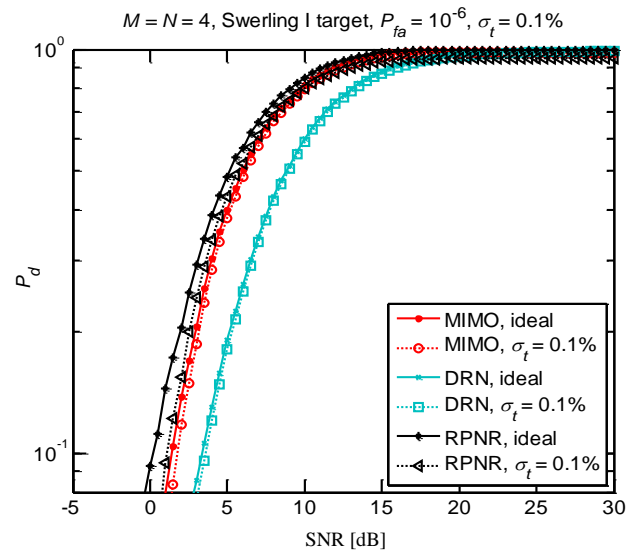


Fig. 3.10. Probability of detection under time jitter influence in a 4×4 configuration: (a) $\sigma_t = 0.1\%$ and (b) $\sigma_t = 1\%$.

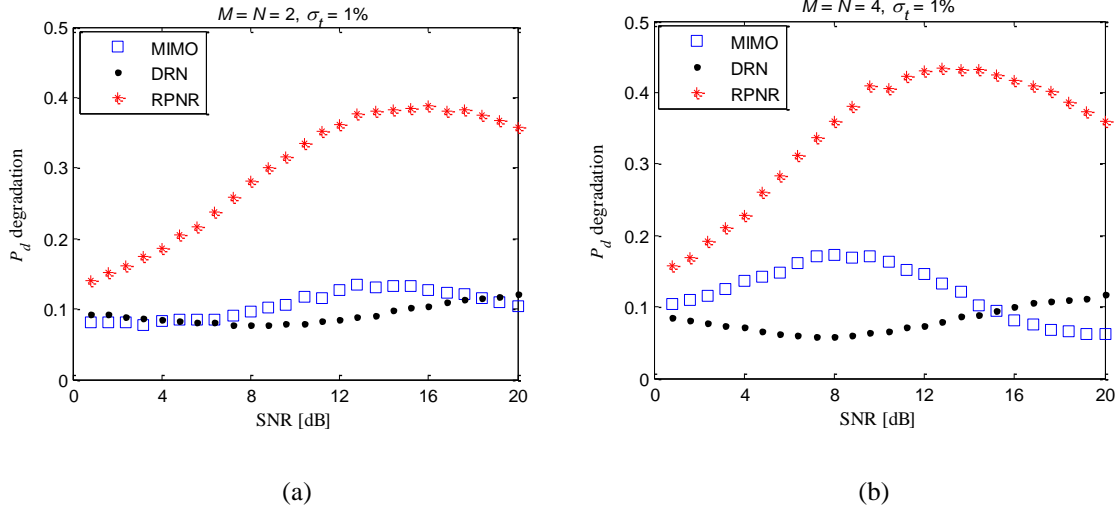


Fig. 3.11. P_d degradation under time jitter influence: (a) 2×2 and (b) 4×4 configurations.

B. Simulation of Phase Jitter Effects on the Detection Performance of MIMO Radars.

Figure 3.12 depicts the simulation model considering phase jitter in the receiver side of the MIMO radar system. Similar simulation parameters as listed in Table 3.1 were used, and each transmitting signal were up-converted to a center frequency of 1 GHz. At the receivers, the arriving signals were passed through mixers for down-converting operation, prior to matched filtering and signal processing. The mixers were fed with carrier signals from the receiver's local oscillators, which were modeled to have specific phase jitter characteristics. Ideally, the carrier signal can be expressed by

$$y(t) = A \sin(2\pi f_c t), \quad (3.15)$$

where A is the peak amplitude and f_c is the center frequency. The phase jitter was modeled in such a way that the signal in Eq. (3.16) consisted of variation of phase characterized by

$$y(t) = A(1 + \psi(t)) \sin(2\pi f_c t + \phi(t)), \quad (3.16)$$

where $\phi(t)$ was the phase variation in radian, taking values from $-\pi$ to π , and $\psi(t)$ was termed as the amplitude error which corresponded to small amplitude variations due to other noises in the system. The phase jitter was represented by $\phi(t)$, which followed Gaussian distribution, with standard deviation σ_ϕ as the controlling parameter. In this study, independent phase jitter was modeled at the each receiver. The amplitude error $\psi(t)$ was assumed to be relatively small and thus not considered in this work.

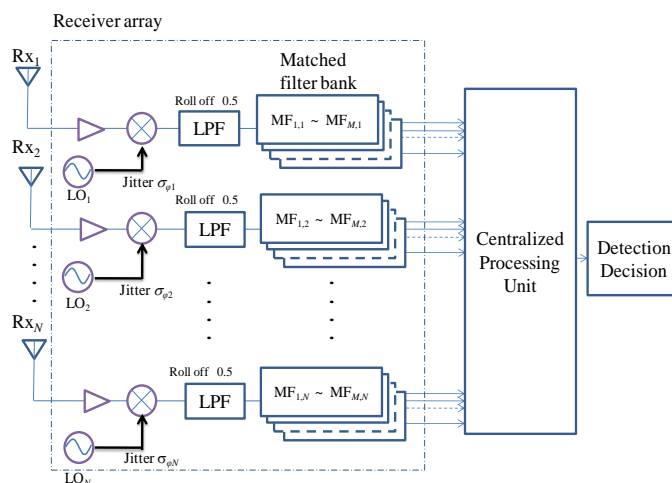


Fig. 3.12. Simulated model of phase jitter in the MIMO radar receiver.

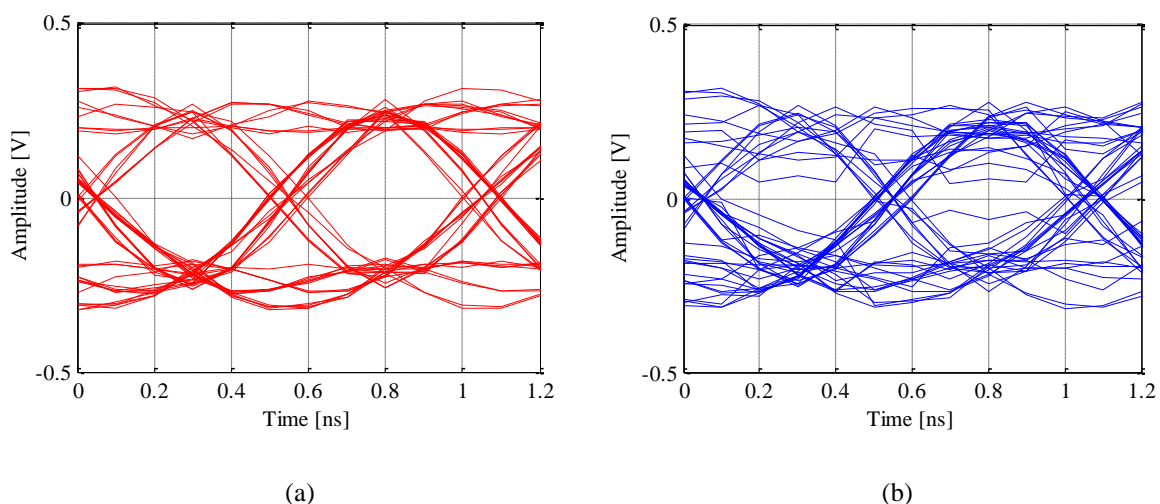


Fig. 3.13. Eye pattern plots of a receiving signal (roll-off factor 0.5, SNR = 20 dB): (a) without jitter and (b) $\sigma_\phi = 0.5$ radian.

The eye pattern of a receiving signal with and without phase jitter is shown in Fig. 3.13. It can be observed in Fig. 3.13 (b) that the presence of phase jitter influenced the quality of the eye pattern plot.

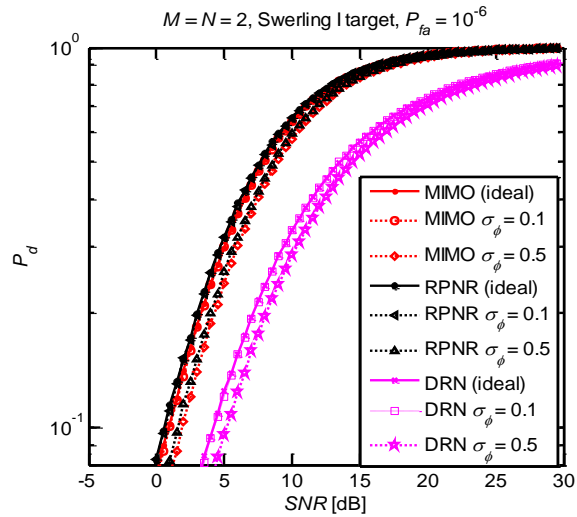
The simulation results considering phase jitter is presented in Fig. 3.14. Similar to the previous simulations, the P_{fa} was fixed at 10^{-6} for all cases. It was shown that when only phase jitter was taken into consideration, the performance of the simulated MIMO radar degraded with increasing value of σ_ϕ . Interestingly, the P_d of all types of processing schemes exhibited similar trend of degradation versus SNR, as shown in Fig. 3.14. This was evident in cases of σ_ϕ taking a large value of 0.5 radian,

where the P_d resulted in 2 dB loss at low SNR region. Nevertheless, no significant degradation was observed when σ_ϕ took values of 0.1 radian or lower (not shown here due to space consideration), indicating that the performance losses were negligible. Furthermore, referring to Fig. 3.14 (c), 4×4 configuration marked similar trend of performance degradation to the 2×2 case.

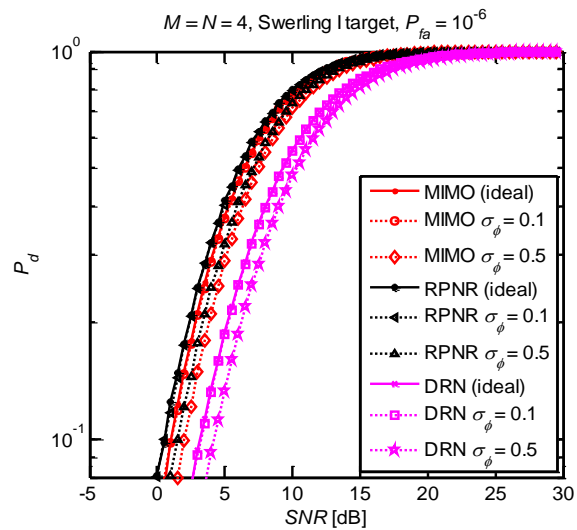
The amount of P_d degradation for both 2×2 and 4×4 are plotted in Fig. 3.15. Similarly with Fig. 3.13, the P_d degradation was higher with increasing SNR, indicating that the effects of jitter became dominant when the thermal noise in the system was insignificant. The amount of P_d degradation due to phase jitter was almost the same for all processing scheme.

Figure 3.16 shows the receiver operating curves (ROC) of the MIMO radar systems, where the P_d is plotted while varying the P_{fa} from 10^{-1} to 10^{-6} . The ROC is plotted with fixed SNR of 10 dB, and cases where the phase jitters were $\sigma_\phi = 0.1$ and 0.5 radian. This is to show that at a fixed SNR, the performance losses in P_d of all type of processing schemes were similar, even when choosing different P_{fa} . It can be observed in Fig. 3.16 (a) that at $P_{fa} = 10^{-6}$, all processing schemes marked approximately 5% loss of P_d , when σ_ϕ took values of 0.5 radian. The degradation amount gradually decreased with increasing P_{fa} , for example, to 2% at $P_{fa} = 10^{-2}$. Figure 3.16 (b) shows that the 4×4 case yielded similar trend, however, with slightly larger P_d degradation. The P_d degradation of all processing schemes at $P_{fa} = 10^{-6}$ and $\sigma_\phi = 0.5$ were calculated and summarized in Table 3.2, and Fig. 3.17. From the table, it was evident that the DRN processing indicated significant P_d degradation with increasing numbers of antenna. The P_d degraded approximately 2% when scaling up the MIMO configuration from 2×2 to 3×3, and another 2% to 4×4. This result implied that when a large MIMO configuration was used (e.g. 10 to 100 elements), the phase jitter could significantly degrade the P_d when σ_ϕ was sufficiently large, especially for the DRN.

Summarizing the above results, it can be concluded that phase jitters directly affects the SNR yielding equivalent performance of the MIMO radar systems, regardless of the types of processing scheme used. Although the degradation was negligible when phase jitter was insignificant, it is worth to consider the degradation amount, especially when the system does not have sufficient SNR margin, and when the MIMO configuration is large. This is because the performance degradation scaled up with increasing antenna elements in the MIMO radar system. Implementing a large MIMO configuration up to 100 elements and above as described in [48] could suffer significant performance degradation due to phase jitter. Therefore, in severe cases, it is recommended to utilize adaptive techniques to compensate the SNR loss, for example, an optimal energy distribution method proposed in [44].

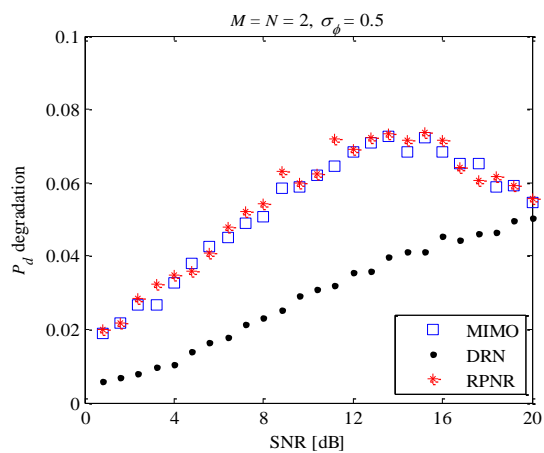


(a)

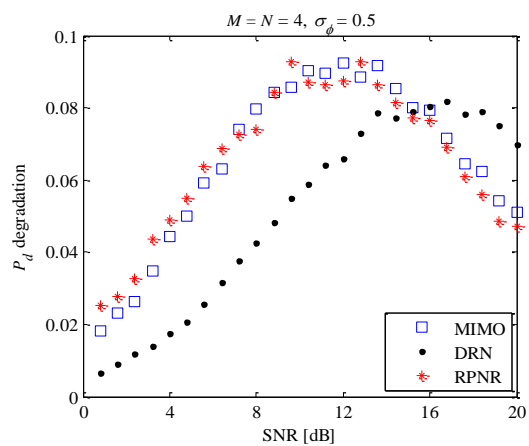


(b)

Fig. 3.14. Simulated probability of detection of MIMO radar system under phase jitter influence: (a) 2×2 , and (b) 4×4 configurations.

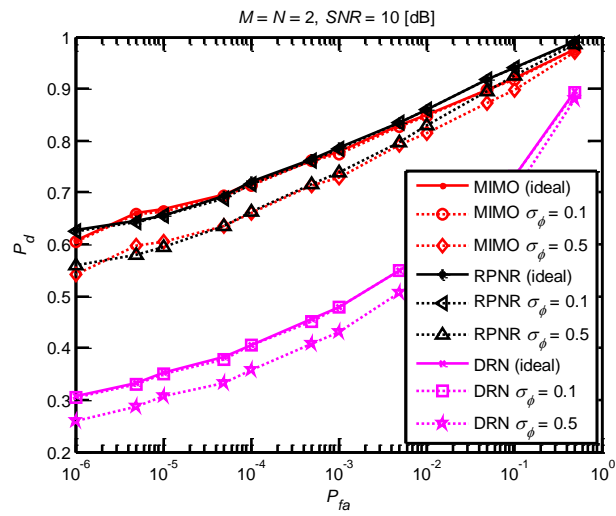


(a)

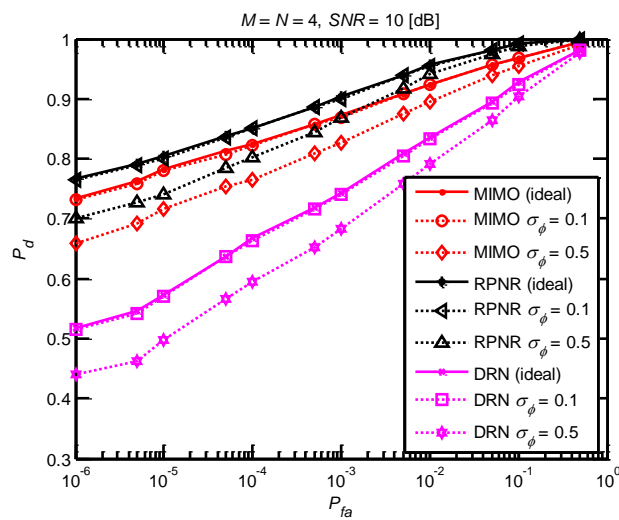


(b)

Fig. 3.15. P_d degradation phase jitter influence: (a) 2×2 and (b) 4×4 configurations.



(a)



(b)

Fig. 3.16. Receiver operating curves of the simulated MIMO radar systems with presence of severe phase jitter: (a) 2×2 and (b) 4×4 configurations.

Table 3.2. Probability of detection degradation for increasing transmit-receive elements in MIMO radar

($P_{fa} = 10^{-6}$, $\sigma_\phi = 0.5$, SNR = 10 dB)

MIMO configuration	P_d Degradation		
	MIMO	RPNR	DRN
2×2	0.061	0.063	0.046
3×3	0.061	0.064	0.066
4×4	0.067	0.065	0.084

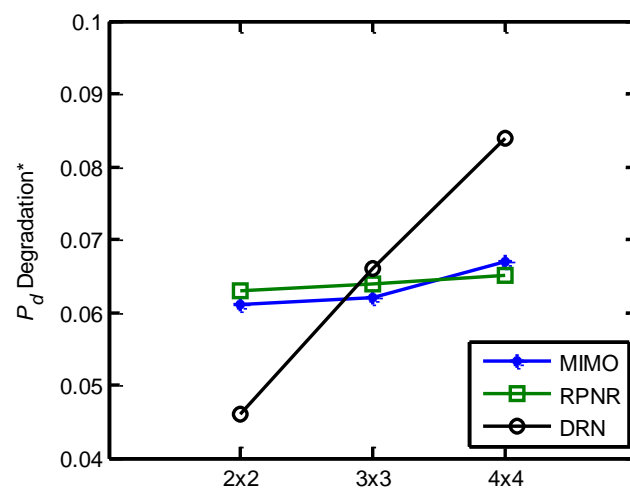


Fig. 3.17. Probability of detection degradation for increasing transmit-receive elements in MIMO radar.

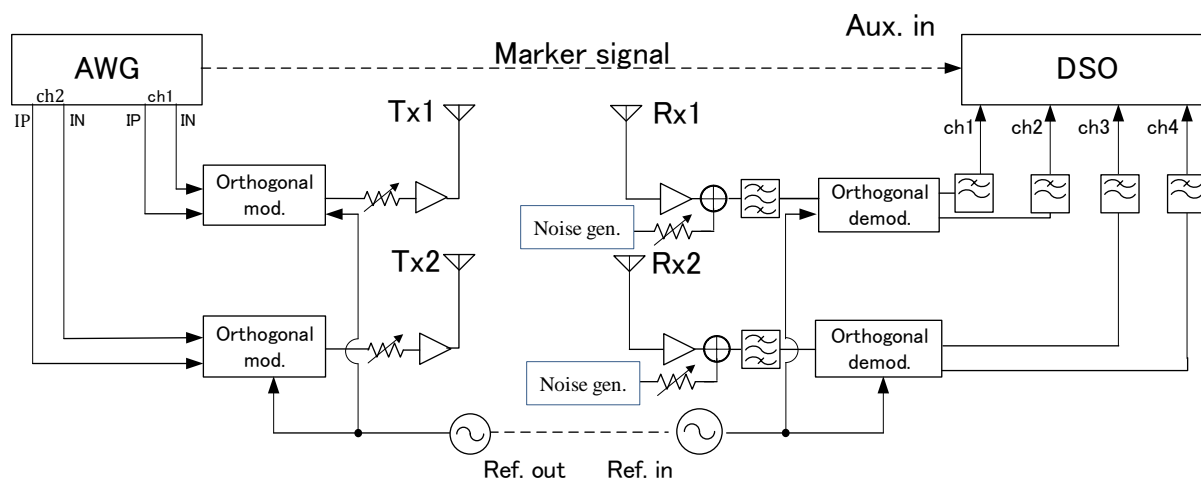
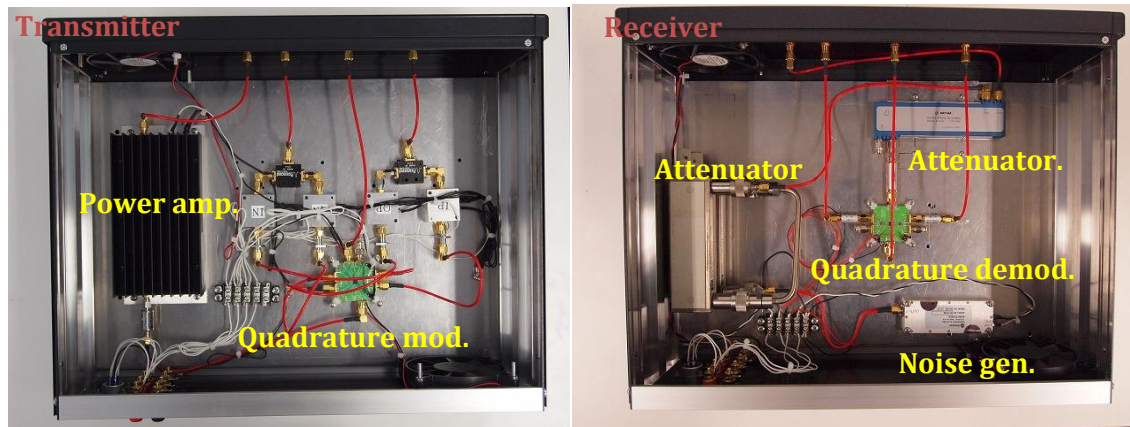


Fig. 3.18. The diagram of the developed MIMO radar testbed.

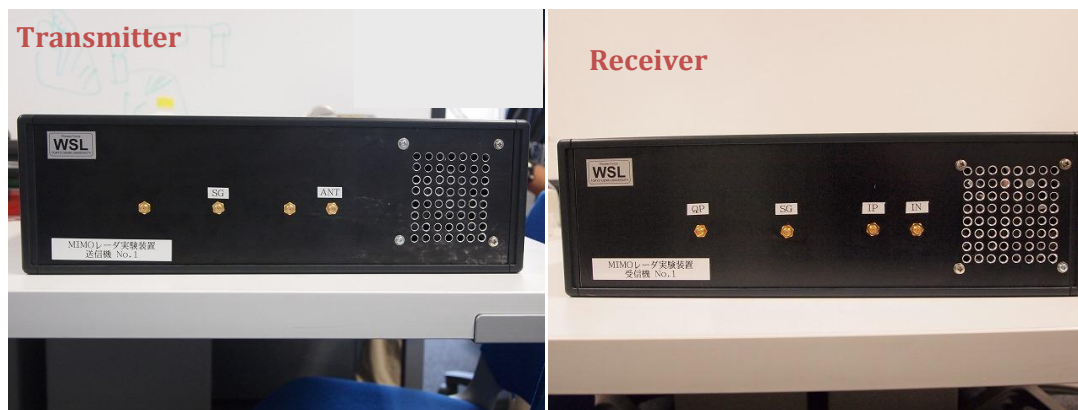
3.5. DEVELOPMENT OF MIMO RADAR TESTBED AND EXPERIMENTAL RESULTS

A MIMO radar testbed system was developed to evaluate the performance of the M-sequenced-based MIMO radar through experimental evaluation. This section describes the developed MIMO radar testbed and discussed its performance from results obtained from experimental evaluation in a radio anechoic chamber. The block diagram of the testbed system is depicted in Fig.3.18. The transmitter side consists of an arbitrary wave generator (AWG), quadrature modulator, stepped attenuator, hybrid coupler, band pass filter (BPF), and the transmitting antenna. The specification of the AWG is listed in Table 3.3. We used a UWB horn antenna with average gain of 15 dBi as the transmitting and receiving antennas. A differential signal generated from the AWG is sent to the modulator using binary phase shift keying (BPSK) through in-phase positive (IP) and in-phase negative (IN) lines. Although the modulator is capable of handling both in-phase and quadrature-phase components, we only utilized the in-phase lines for the BPSK transmission. The modulated signal with center frequency of 3.5 GHz and 500 MHz bandwidth is transmitted from the UWB antenna.

The receiving system consists of quadrature demodulators and a digital sampling oscilloscope (DSO). Noise generators (NG) were used at each of the receivers to adjust the thermal noise composition in the MIMO radar system. This enables us to evaluate the detection performance of the system against varying SNR. All the received signals captured by the DSO were jointly processed through offline processing routine implemented in MATLAB. The developed MIMO radar transmitter



(a)



(b)

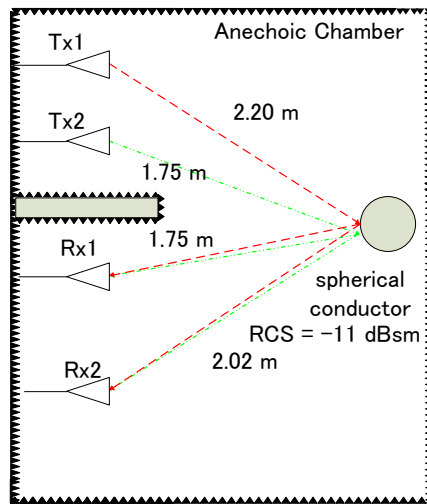
Fig. 3.19. The developed transmitter and receiver the MIMO radar testbed system: (a) Internal parts and (b) front panels.

Table 3.3. Specification of AWG.

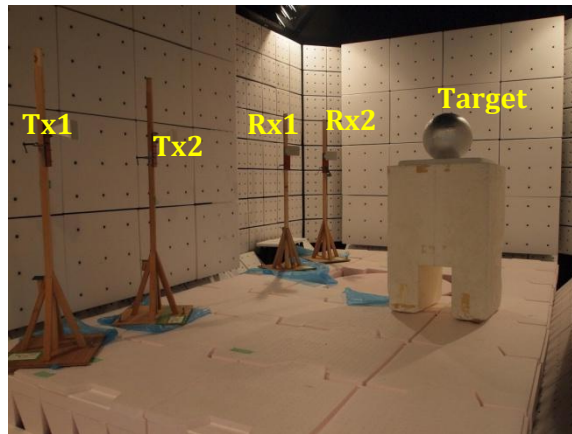
Parameters	Description
Manufacturer	Tektronix
Model	AWG7102
Maximum sampling rate	10 GS/s
Maximum memory length	32 MB
Output ports	2 analog output (each with inverse channel and marker signal)

Table 3.4. DSO specification.

Manufacture	Tektronix
Model	TDS6154c
Max sampling rate	40 GS/s
Max memory length	64 MB
Input port	4 channel



(a)



(b)



(c)

Fig. 3.20. Scenario of experiment in a radio anechoic chamber: (a) Experimental layout, (b) measurement scenario, and (c) usage of microwave absorber to suppressed direct wave.

and receiver module are shown in Fig. 3.19. Prior to the signal processing routine, the received signal was cross-correlated with the reference signal to detect the start and end bit. Refer to the appendices for detail specifications of the equipment used.

A measurement campaign was conducted to evaluate the detection performance of MIMO radar based on the developed testbed system. The measurement was conducted in a radio anechoic chamber, using a 2×2 MIMO radar configuration detecting a spherical target located at the middle part of the chamber. Detail positions of the target and the antennas are shown in Fig. 3.20 (a). In order to emulate the spatial MIMO radar conditions derived in Eq. (1.1), the antennas spacing are in similar order with the target distance from each antennas, as shown in Fig. 3.20 (b). In order to suppress the direct wave, we positioned some microwave absorbers between the transmitting and receiving antennas. This measurement scenario is depicted in Fig. 3.20 (c).

Figure 3.21 shows the generated m -sequences waveforms from each of the transmitting antennas. We could observe the different codes were assigned to each of the transmitting signal. The corresponding frequency spectrum of one transmitting signal is shown in Fig. 3.22. Comparison of the eye pattern plot of the generated and simulated signal is depicted in Fig. 3.23. The generated signal marked a slightly distorted pattern compared to the simulated one, due to system's noise. The frequency spectrum was observed using a spectrum analyzer on the output of the quadrature modulator of one of the transmitters (an attenuator was used to avoid over voltage at the input port of the spectrum analyzer). We can see from the figure that the signal was upconverted to 3.5 GHz, and the SNR is approximately 17 dB in this case.

The performance of the system in terms of P_{fa} and P_d was shown in Fig. 3.24. It was observed that at $P_{fa} = 10^{-6}$, the threshold of MIMO, and NR are larger than that of the DRN processing. This agreed with the simulation results. The P_d obtained from the measurement also showed similar trend with the simulations, where the RPNR marked the best P_d at 80% detection line. The MIMO processing sits between the RPNR and the DRN. All MIMO processing scheme marked better P_d than the SISO case. In this measurement, the results were considered to include jitter influences in the hardware. It is difficult to create and emulate arbitrary jitters into the developed system due to hardware limitation. However, the experimental results obtained using the developed MIMO radar testbed provide us with fundamental understanding of the capability of the system.

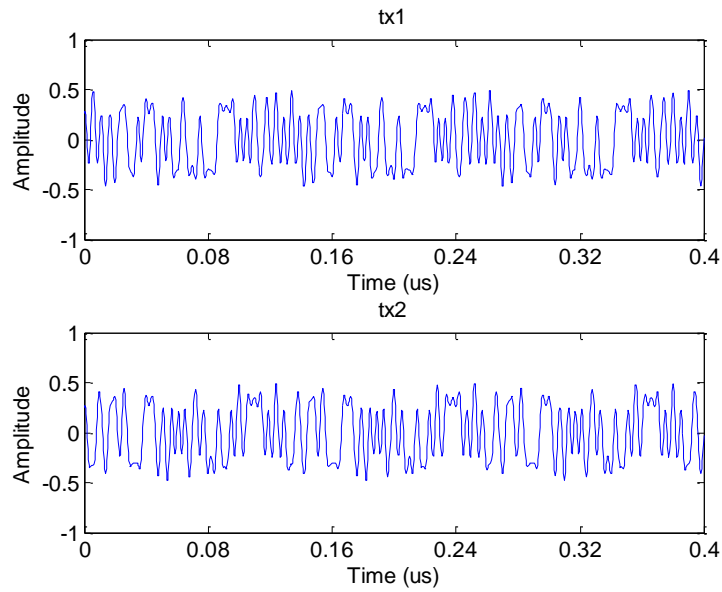


Fig. 3.21. The waveforms of transmitting signals.

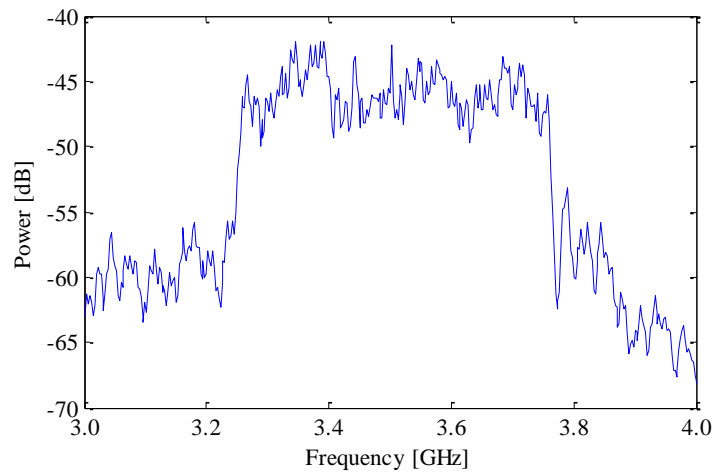


Fig. 3.22. Measured frequency spectrum of the transmitting signal from Tx 1.

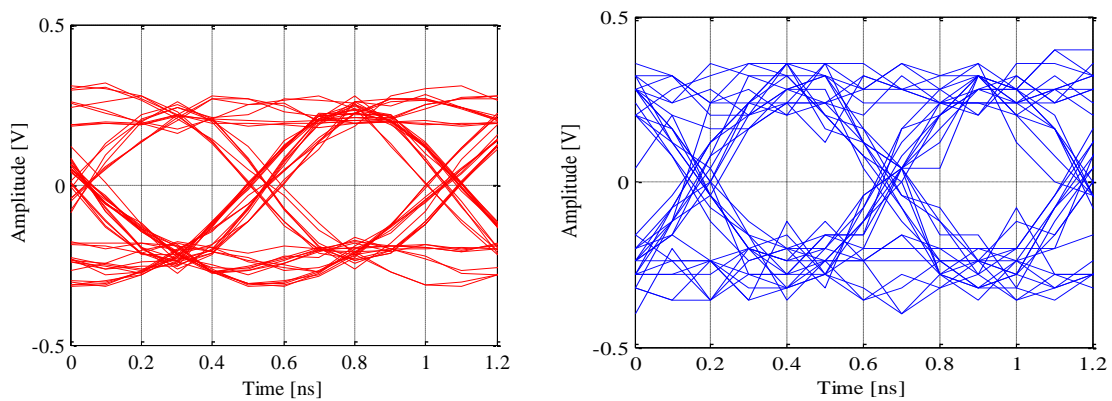
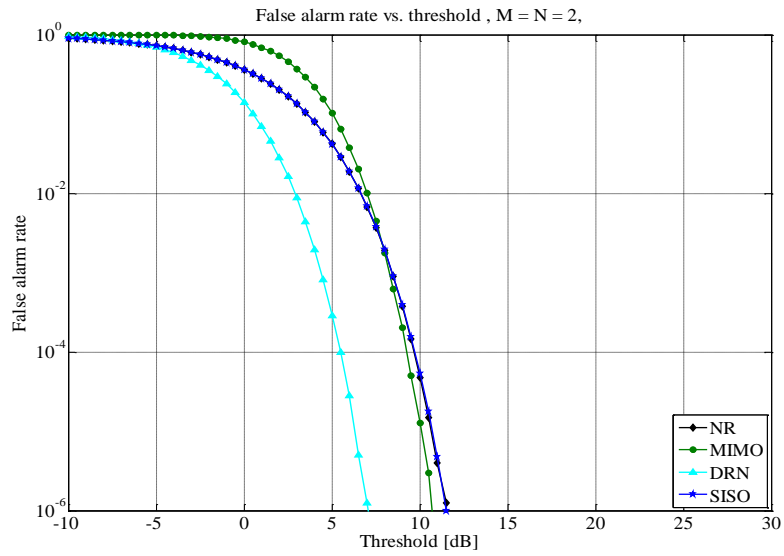
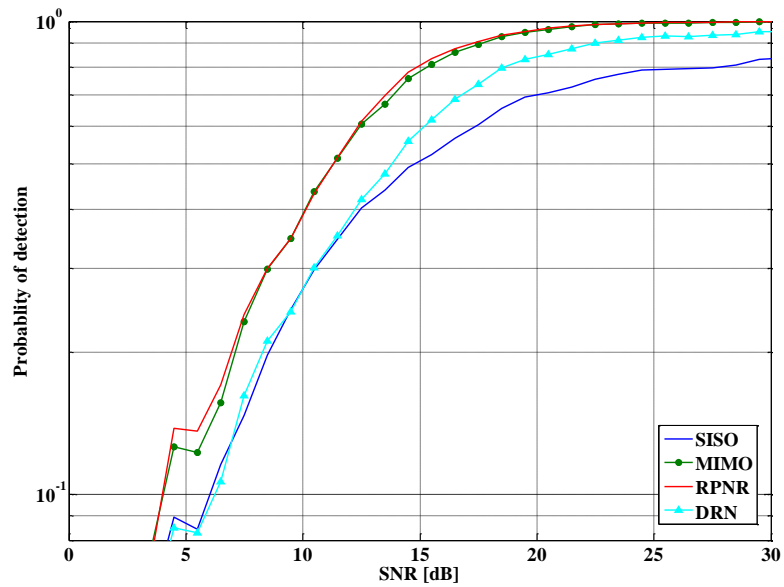


Fig. 3.23. Eye pattern plots of a receiving signal (roll-off factor 0.5, SNR = 20 dB): (a) simulated and (b) measured.



(a)



(b)

Fig. 3.24. Performance of the MIMO radar obtained from measurements in radio anechoic chamber: (a) Probability of false alarm and (b) probability of detection curves.

3.6. SUMMARY

The detection performance of m -sequence-based MIMO radar systems was evaluated through numerical simulations and experiments in radio anechoic chamber. Time domain simulations were carried out to evaluate the MIMO radar detection performance in both ideal conditions, and while considering the presence of jitter. Jitters were modeled as time and phase jitter in the MIMO radar receiver. The study considered three processing schemes for the MIMO radar, namely the MIMO, RPNR and DRN processing. The probability of detection P_d of the MIMO radar system for each processing scheme was evaluated against SNR while varying the amount of jitter present in the system.

Firstly, it was observed that the effects of time jitter on the detection performance of MIMO radar were negligible when a non-coherent MIMO and DRN processing scheme were used. However, the detection performance of RPNR scheme degraded significantly when the standard deviation of the timing jitter was 1 % of the ideal clock (50 ppm). The results implied that the effects of time jitters were significant only in the case of a coherent processing where precise timing is essential in maximizing the SNR at the receiver. Therefore careful consideration of time jitter should be given when using this type of processing. We can derive from the results that commercially available crystal oscillators with jitters in the range of 50 -500 ppm could bring considerable performance degradation to the system, while a more stable oscillators such as the temperature compensated voltage controlled, and rubidium oscillators are the more suitable options to drive the MIMO radar universal clock.

Secondly, it was shown that phase jitter at the local oscillator of each receiver directly degraded the SNR yielding similar probability of detection of the MIMO radar system, regardless of processing scheme chosen. Nevertheless, the results showed that the performance degradation due to phase jitter was negligible if the amount of jitter was limited to below 0.1 radian. We also observed that increasing P_d degradation with the number of antennas, which may significantly affect the system performance when using a large MIMO array in low SNR condition.

A MIMO radar testbed system was developed for experimental evaluations in a radio anechoic chamber. The developed testbed system was capable of operating in 2×2 MIMO mode, which transmits two different m -sequence-codes and received them simultaneously. The received signal was processed through offline processing to calculate the P_d of the developed MIMO radar system. The P_d was observed to be of similar order with the simulated results. Although the developed testbed system did not have the capacity to operate in larger MIMO configuration such as 3×3 and 4×4 , we considered that the current hardware system successfully validated the simulated results based on the 2×2 MIMO case. We are looking forward to extend the existing hardware to be able to support larger

MIMO configurations in the near future, for example to a 3×3 configuration. In addition, the hardware will be also modified to be able to generate pre-known jitter characteristics for experimental evaluation of jitter effects on the MIMO radar system.

Chapter 4

JOINT DIRECTION-OF DEPARTURE AND DIRECTION-OF-ARRIVAL ESTIMATION IN ULTRA WIDEBAND MIMO RADARS

4.1. INTRODUCTION

Target localization in radar has been intensively studied in literatures since the early years of radar. In general, radar systems estimate the target position by means of trilateration or triangulation. Trilateration can be implemented by using a minimum of two stations, however, the localization resolution is limited by the signal bandwidth, and usage of multiple stations is required to avoid ambiguities (ghost targets). On the contrary, triangulation is based on the angles of targets observed from the radar stations, and hence it does not suffer from the bandwidth constraint in a direct sense. In MIMO radar, it is possible to jointly estimate the direction-of-departure (DOD) and direction-of-arrival (DOA) by implementing array processing at both of the transmitting and receiving array, as depicted in Fig. 4.1. This makes it suitable for triangulation-based localization.

Numerous works on DOD and DOA estimation have been reported [37, 49, 50]. Nevertheless, these studies were mainly based on narrowband signal assumption. Target localization using the narrowband signal, however, was unstable due to fluctuation of target's radar cross section (RCS). In order to overcome this problem, MIMO radars using multiple sub-carriers and an orthogonal frequency division multiplexing (OFDM) waveforms were proposed [39, 51]. Those schemes, however, only discussed one-dimensional angle estimation of a single target, and implementation of limited number of sub-bands. Utilization of wider signal bandwidth might be useful in localizing target with significantly small or severely fluctuating RCS. One of the most promising technologies with wideband capability is ultra wideband (UWB) systems. The usage of UWB signal for angle estimation in MIMO radar, however, has not being given much attention, limiting the study to medical imaging and through-the-wall radars [52, 53]. Application of conventional angle estimation methods (*e.g.* Capon, multiple signal classification (MUSIC), and estimation of signal parameters via rotational invariance (ESPRIT)) to a UWB signal is a challenge since those methods inherently assume narrowband signals.

The present authors proposed a joint DOD and DOA estimation in a UWB MIMO radar using the combination of a two-way MUSIC and angle histograms. The basic idea in the proposed scheme

was to treat the UWB signal as a summation of sinusoidal waves swept over the frequency band, and angle estimation was done at each of the frequency by means of two-way MUSIC. The estimation results were then combined using majority decisions formulated using angle histograms [54].

It is important to mention here that the RCS fluctuation problem have been continuously studied in the radar community. Until recently, special attention has been given to the subject in the case of MIMO radar, since the usage of MIMO configuration offers further degrees of freedom in the forms of spatial, frequency and also waveform diversity. For example, the works in [55] employed spatial and waveform diversity in MIMO radars to increase the probability of detection and direction finding performances when detecting fluctuating target. This present study employs different approach from those reports since we focused on the utilization of frequency diversity. Studies regarding MIMO radars utilizing frequency diversity in detecting fluctuating RCS were studied, for instance in [56, 57], where several sub-bands with substantially wide frequency spacing were used for angle estimation. This study differs from those works from a point of view that we employ the diversity among a large number of sub-bands throughout the frequency bandwidth of a UWB system to enhance target localization performance, and specifically demonstrated the application to MIMO radar.

4.2. PROPOSED SCHEME

Consider a MIMO radar with M transmitting and N receiving elements, illuminating L uncorrelated targets located at the far field of transmit and receive arrays. At the transmitting side, M orthogonal UWB signals are emitted, each consists of multiple sinusoidal waves swept over the UWB bandwidth. Here, we define the complex transmitting signal waveform vector by $\mathbf{s}(t) = [\mathbf{s}_1(t), \dots, \mathbf{s}_M(t)]$, where each term contains K frequency components. The orthogonality between the transmitting signals can be achieved through time division scheme, where each transmitting antenna emits the UWB signal in separate time slots. Figure 4.1 illustrates an example of the transmitting signal which uses 3.1 to 10.6 GHz of sinusoidal waves in 1 MHz intervals. The receiving signal of the k^{th} frequency component can be expressed by

$$\mathbf{x}_k(t) = [\mathbf{a}_t(\phi) \otimes \mathbf{a}_r(\theta)]\mathbf{s}^{(k)}(t) + \mathbf{n}(t), \quad (4.1)$$

where \otimes denotes the Kronecker product, \mathbf{a}_t and \mathbf{a}_r are the transmit and receive steering vectors, respectively, ϕ and θ are the corresponding transmit and receive angles, $\mathbf{s}^{(k)}(t)$ represents the k^{th}

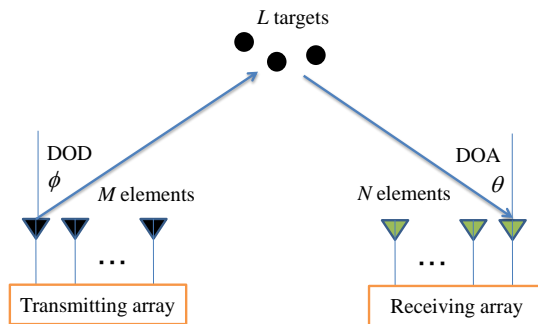


Fig. 4.1. Overview of angle estimation in MIMO radar.

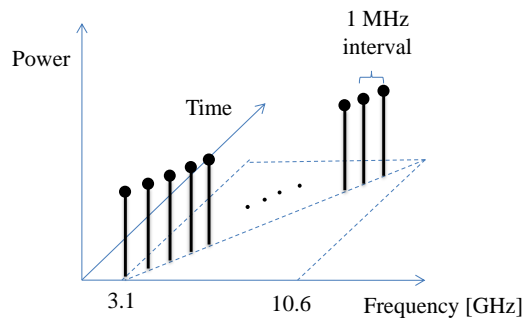


Fig. 4.2. The proposed UWB signal for MIMO radar angle estimation.

frequency component of the transmit signal vector $\mathbf{s}(t)$, and $\mathbf{n}(t)$ is the total additive white Gaussian noise. The receiving signal covariance matrix of the k^{th} frequency component is given by

$$\mathbf{R}_{xx_k} = E[\mathbf{x}_k(t) \cdot \mathbf{x}_k(t)^H], \quad (4.2)$$

where $E[\cdot]$ is the ensemble average, and $[\cdot]^H$ represents the conjugate transpose operation. Here, singular value decomposition (SVD) of the covariance matrix gives

$$\mathbf{R}_{xx_k} = \mathbf{E}^{(k)} \mathbf{V}^{(k)} \mathbf{E}^{(k)H}, \quad (4.3)$$

where $\mathbf{V}^{(k)}$ is a diagonal matrix whose diagonal elements contain the signal and noise eigenvalues for the k^{th} frequency, and $\mathbf{E}^{(k)}$ is the corresponding eigenvectors of the signal and noise components. The

two-dimensional spatial MUSIC spectrum at the k^{th} frequency component can be constructed using the function:

$$P_{\text{MU}_k}(\phi, \theta) = \frac{1}{[\mathbf{a}_t(\phi) \otimes \mathbf{a}_r(\theta)]^H \mathbf{e}_Z^{(k)} \mathbf{e}_Z^{(k)H} [\mathbf{a}_t(\phi) \mathbf{a}_r(\theta)]}, \quad (4.4)$$

where $\mathbf{e}_Z^{(k)}$ is the noise eigenvectors obtained from the eigendecomposition of the receive signal covariance matrix in Eq. (4.2). Here, we have the L largest peaks which correspond to the DOD and DOA of the targets at each frequency component. The wideband DOD and DOA is decided by taking the majority of estimated angles among all the estimates at each frequency. This is denoted by ‘majority decision’ in this study. The majority decision is formulated by initially combining DOD and DOA estimates at the K frequencies into a vector, and arranging them in the form of angle histograms as depicted in Fig. 4.3. The angle histogram can be viewed as a function of angle i from -90° to 90° at intervals of, for example, 0.5° . The normalized number of occurrence of the peak angle is then given by

$$\hat{r}^{(i)} = \frac{1}{u} p^{(i)}, \quad (4.5)$$

where $p^{(i)}$ is the number of occurrences of the angle i , and u is the normalized coefficient given by

$$u = \arg \max \hat{r}^{(i)}. \quad (4.6)$$

The majority decision is obtained by searching the peak of the histogram. As a benchmark, the performance of the proposed scheme will be compared with the conventional spectrum averaging method [38] used in existing sub-band processing scheme for angle estimation. The spectrum averaging method adopts an approach which takes the average of the estimated MUSIC spectra of all K frequency components:

$$P_{\text{MU}_{\text{ave}}}(\phi, \theta) = \frac{1}{K} \sum_{k=1}^K P_{\text{MU}_k}(\phi, \theta). \quad (4.7)$$

Then the wideband DOD and DOA is estimated from the L largest peaks of $P_{\text{MU}_{\text{ave}}}$. We will demonstrate in Section 4.3.2 that the majority decision technique performs better than the spectrum averaging method. Figure 4.4 depicts the block diagrams of the proposed and conventional schemes.

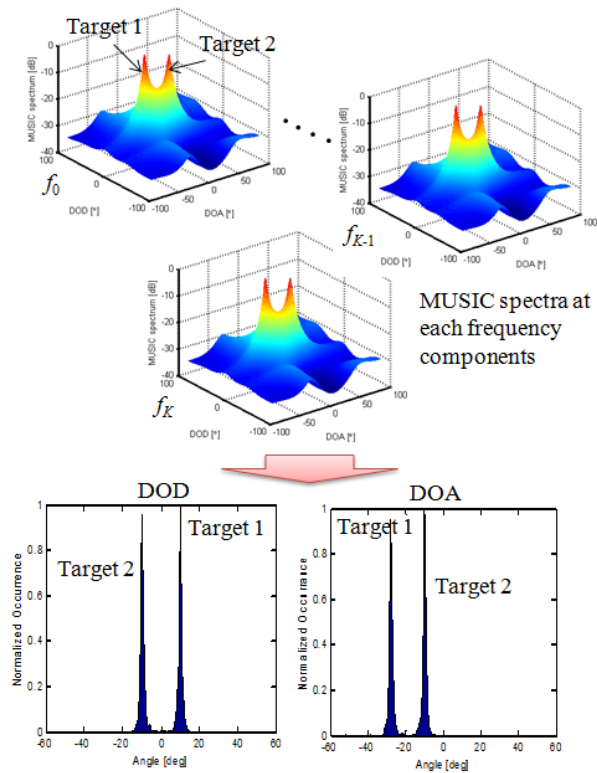


Fig. 4.3. Formulation of angle histograms from two-way MUSIC spectra at each frequency component.

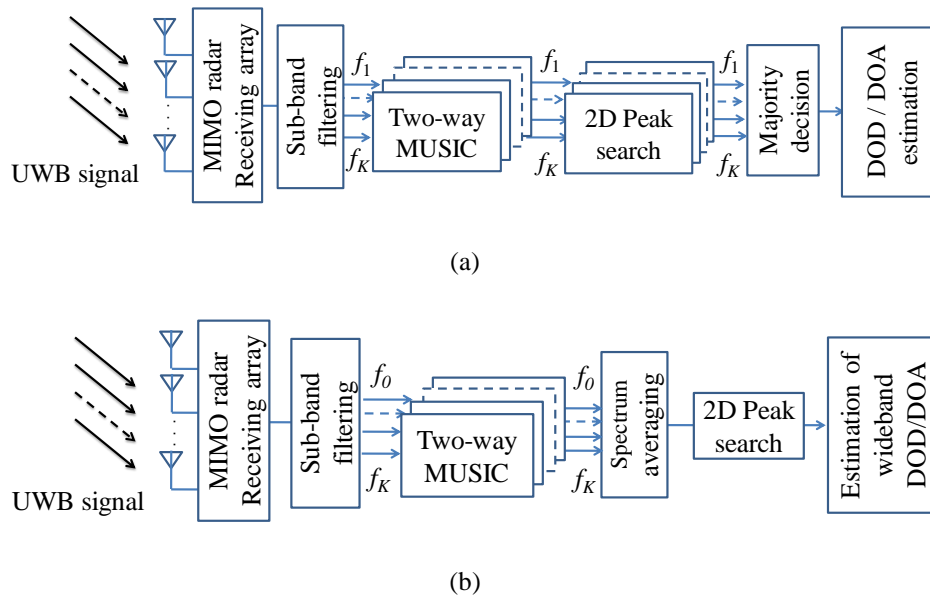


Fig. 4.4. Block diagrams: (a) proposed and (b) conventional schemes.

B. MIMO radar array configuration

The main advantage of a MIMO radar system is that the degrees of freedom can be enhanced by using the concept of virtual array [6, 58]. When orthogonal signals were transmitted from different antennas, the back scatter returns of each orthogonal signal will carry independent phase information that forms a new virtual array steering vectors at the receiver. The virtual array can be characterized by convolution of the transmitting and receiving antenna positions. Given a MIMO radar using M transmitting and N receiving antennas, it is possible to form a full virtual array with non-overlapping MN elements, by optimizing the antenna positions. Larger numbers of M and N contribute to construction of longer virtual array, which means further enhancement in angle estimation performance. Thus, from a signal processing point of view, it is generally important to use a larger virtual array. However, in practical applications, it is often beneficial to limit the number of antennas for the sake of cost and space. In this study, we demonstrate the proposed algorithm using a 4×4 MIMO array, and discuss the performance within that limitation.

A full $M \times N$ virtual array can be constructed, for example, by using transmitting antennas with spacing of Nd , and receiving antennas with d spacing, However, as shown in Fig. 4.5 (a), utilizing a two-way MUSIC using this array configuration resulted in spurious peaks in the MUSIC spectrum, since the receiving array's spacing is much larger than the distance of half wavelength. This problem can be overcome by limiting the scan range, but in the cost of narrower coverage area.

In this study, we employed a non-uniform array configuration as shown in Fig. 4.6 to reduce the spurious peaks. This array configuration was chosen due to the minimum number of redundant elements that could be obtained in the virtual MIMO array. The resulting virtual MIMO array obtained from this configuration is illustrated in Fig. 4.7, where we could see that 10 unique elements were constructed out of maximum 16, which cannot be achieved using conventional ULA, for example as depicted in Fig. 1.4 (a). The basic antenna spacing of $d = 15$ mm (corresponds to half wavelength of 10 GHz) was used to avoid the problems of grating lobes when using the UWB signals that consist of up to 10.6 GHz of frequency. Figure 4.5 (b) depicts the resulting MUSIC spectrum using the non-uniform array, where we could observe that the spurious were eliminated, and the resulting spectrum peak sharpness is comparable to a full MN array with limited range scan. Figure 4.5 (c) shows that the spectrum is comparable with a 1×16 SIMO radar using uniform linear array.

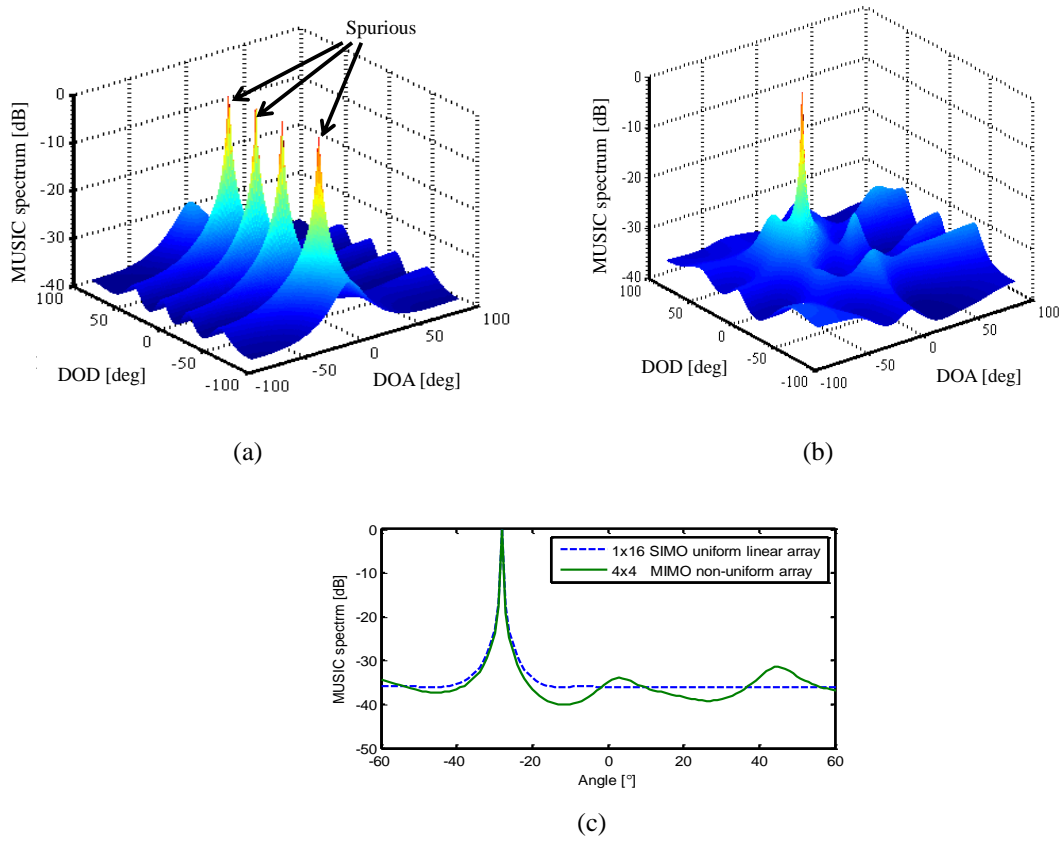


Fig. 4.5. Example of spurious in a simulated MUSIC spectrum ($f_k = 5.0$ GHz).

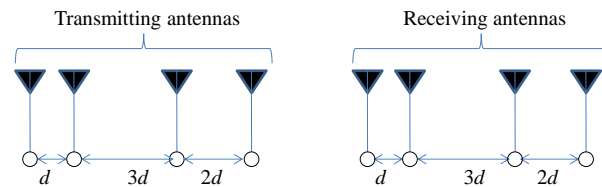


Fig. 4.6. Non-uniform array configuration used in the study ($d = 15$ mm).

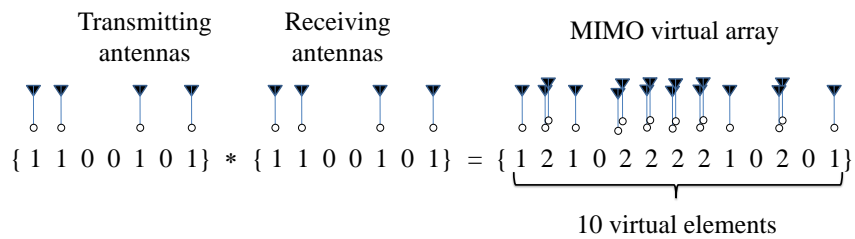


Fig. 4.7. Resulting MIMO virtual array from the non-uniform array configuration used.

C. Complexity Analysis

This sub-section presents the analysis of the computational complexity of the proposed scheme. The computational burden of a conventional 2D-MUSIC has been reported in [37]. For the sake of clarity, we broke down the complexity analysis of the proposed scheme in terms of SVD operation and searching algorithm computational costs, expressed using the O notation [59]. The conventional spectrum averaging method was also analyzed for comparison.

In general, the computation cost for an SVD operation on a square matrix with dimension $u \times v$ is known to be in the order of $u^2v + v^3$ based on Golub and Reinsch algorithm [59]. Considering the total K frequency components used, applying SVD operation on the receiving covariance matrix generally costs $O(K\{u^2v + v^3\})$. Here, from the receiving covariance matrix formulation, u and v are given by M^2 and N^2 , respectively. This is the same for both the proposed and the spectrum averaging schemes. In terms of peak search operation, the proposed scheme performs two-dimensional peak search on the MUSIC spectrum, which costs $O(i^2KL)$, where i is the number of angle bins during search operations. In addition, the majority decision routine costs $O(2\{i+K\}) + O(2\{iL\})$, where the first term corresponds to the histogram formulation of K total estimates, and the second term represents the one-dimensional peak search to identify the angles of L targets. On the other hand, the computational burden of the spectrum averaging method is $O(K) + O(i^2L)$, where the first term corresponds to the spectrum averaging and the second term to the two-dimensional peak search carried out on the averaged spectrum.

The computational complexity against MN antennas is plotted in Fig. 4.8. It was shown that the proposed scheme marked larger computational burden than the spectral averaging method, particularly when the number of MN was small, for example below 30. However, the difference of complexity is reduced with increasing number of antennas, and converges when MN approaches 81. This is because the cost of SVD operation becomes dominant with larger dimension of receiving covariance matrix, thus resulting in similar order of total computational complexity in both methods.

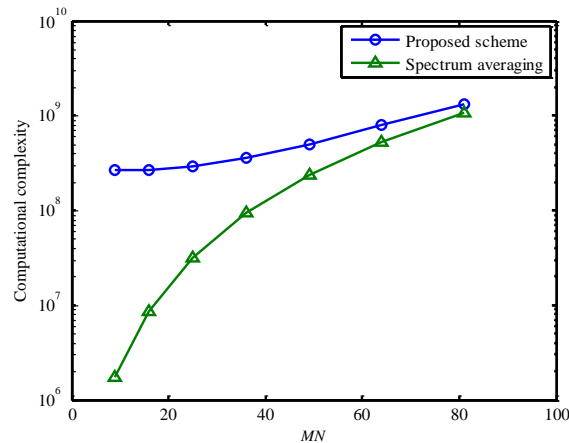


Fig. 4.8. Computational complexity of the proposed scheme against MN antennas ($K = 1000$, $L = 2$)

4.3. SIMULATIONS OF ESTIMATION PERFORMANCE

This section presents numerical simulation to validate the proposed scheme. Firstly, we show the performance of the proposed scheme while detecting fix point target, which were assumed to have a constant RCS. This is to demonstrate the workability of the proposed scheme. The later part of this section presents the performance of the proposed scheme in detecting targets with fluctuating RCS.

4.3.1. PERFORMANCE DETECTING TARGETS WITH CONSTANT RADAR CROSS SECTIONS

The proposed scheme was first simulated to demonstrate its capabilities in utilizing UWB signal in estimating the DOD and DOA of a target. A case of 4×4 MIMO radar detecting a target located at $(\phi, \theta) = (10^\circ, -28^\circ)$ is presented. A non-uniform array using configuration illustrated in Fig. 4.6 was used for this simulation, where $d = 15$ mm (corresponds to the half wavelength of 10 GHz) was used. For the UWB signal, a full-band UWB from 3.1 to 10.6 GHz at 10-MHz intervals was used. The example two-dimensional MUSIC spectrum and the corresponding angle histograms obtained from the simulation are depicted in Fig. 4.9. It was shown from the figure that the peaks of the simulated MUSIC spectrum at 3.1, 8, and 10 GHz precisely corresponded to the target position. We can also observe that the peak at 10 GHz was slightly sharper than that of the 3.1 GHz, due to higher resolution obtained from the high frequency component. Figure 4.10 depicts the estimated

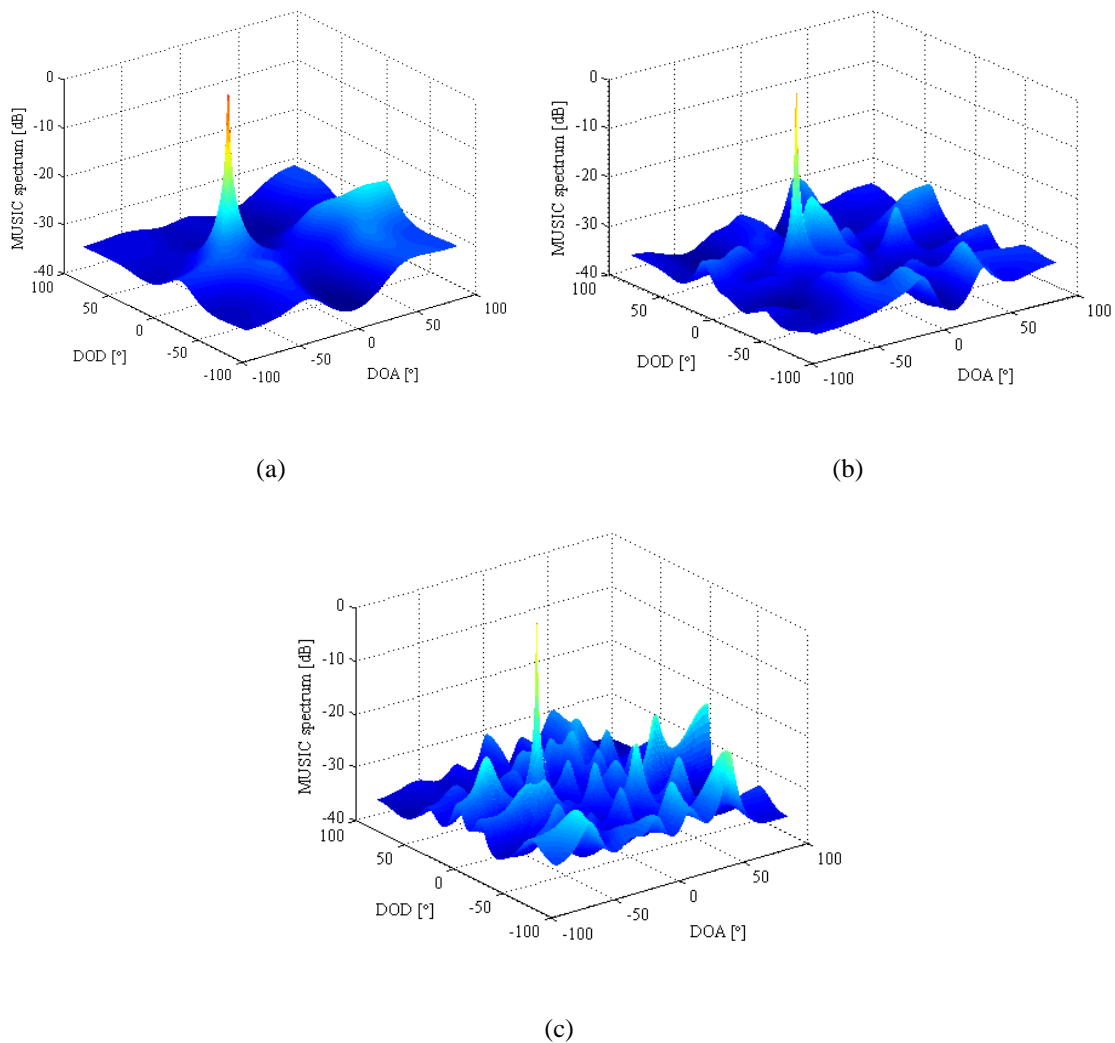


Fig. 4.9. Examples of simulated two-dimensional MUSIC spectrum ($M = 4$, $N = 4$, $L = 1$, SNR = 15 dB, snapshot = 100): (a) $f_k = 3.1$ GHz, (b) $f_k = 6.85$ GHz, and (c) $f_k = 10$ GHz.

angles obtained from the MUSIC spectrum at K frequency components, and the corresponding angle histograms. We can observe from Fig. 4.10 (a) that the estimated angles were found to be distributed around the actual target's angle, however, taking the majority of the estimation from the angle histograms as in Figs. 4.10 (b) and (c) gives us the precise DOD and DOA values.

The performance of the proposed scheme was compared with conventional narrowband estimation using individual frequencies, for example 3.1, 5, 8, and 10 GHz. The results are presented in terms of root mean square error (RMSE) against SNR. Each plot represents the average of 100 independent trials. The performance bound calculated from the Cramér-Rao bound (CRB) when the

DOD and DOA of a stationary target are estimated individually were also plotted in the figure given by [32]

$$C = \frac{1}{G} \left[\frac{1}{ASNR} + \frac{1}{(ASNR)^2} \right] \frac{6}{(N^2 - 1)}, \quad (4.8)$$

where G is the number of snapshot, N is the number of antenna elements and $ASNR$ equals to $N \times SNR$. It can be observed that angle estimation done individually at the respective single frequencies resulted in large estimation errors, which were attributable to the fixed antenna spacing used for the MIMO array, where the spacing d corresponded to a half wavelength of 10 GHz. The larger difference between the frequency of the signal used and the half wavelength's frequency induced

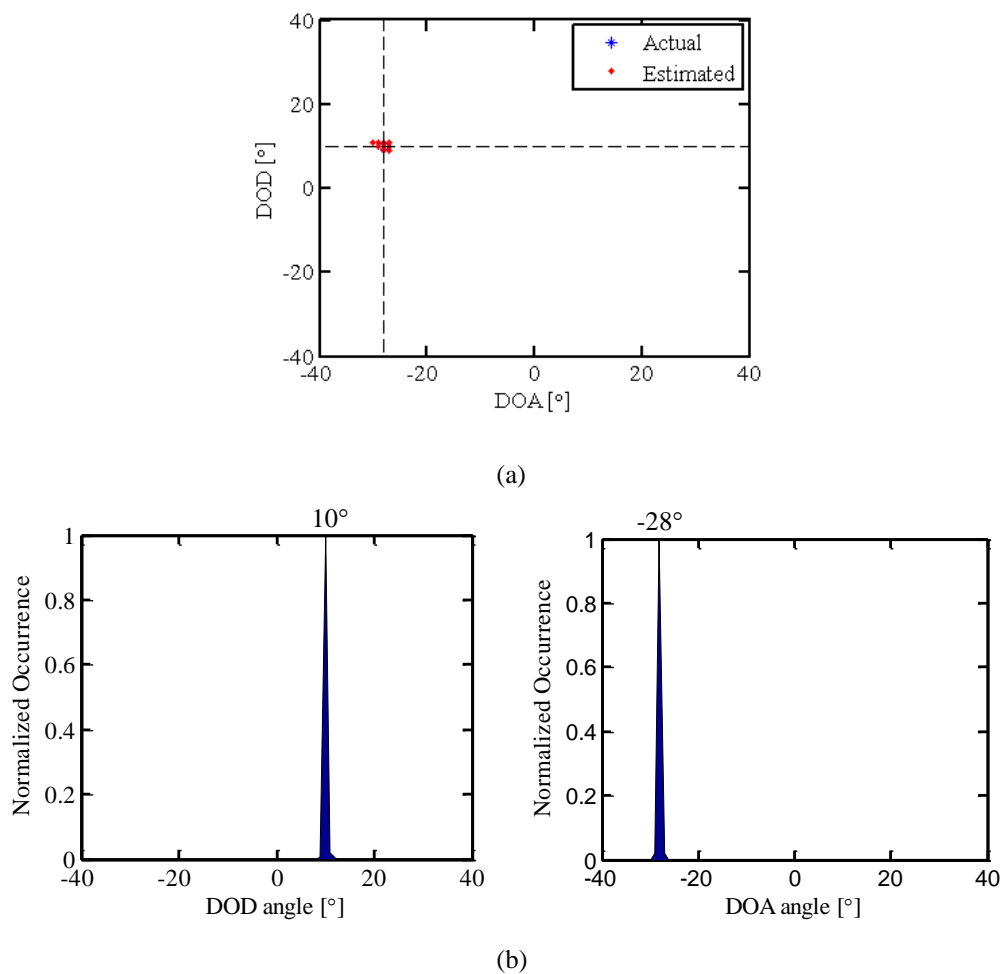


Fig. 4. 10. Example of estimated angles for all K frequencies, and the corresponding angle histograms ($M = 4$, $N = 4$, $L = 1$, $SNR = 15$ dB, snapshot = 100): (a) Estimated DOD and DOA and (b) angle histograms.

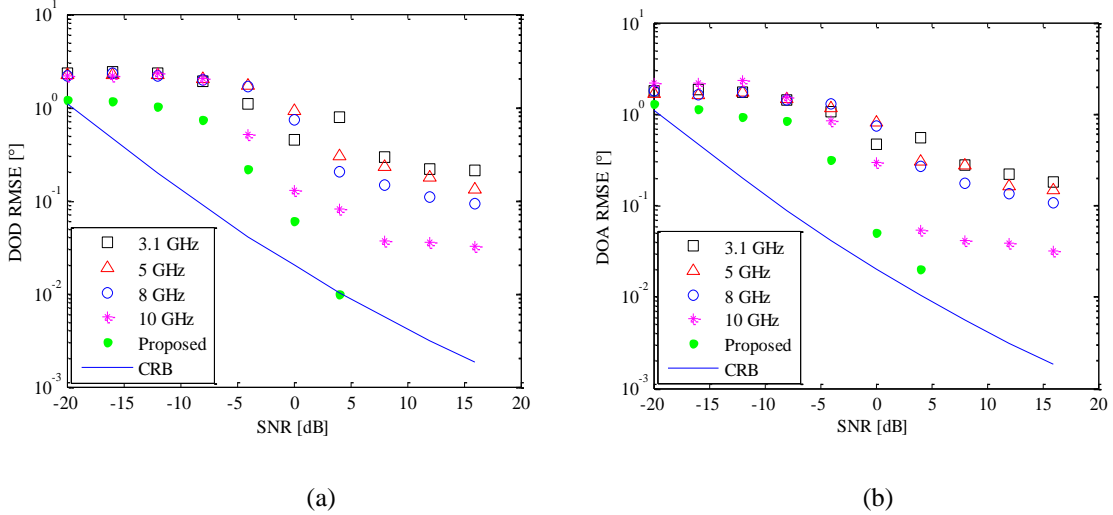


Fig. 4. 11. Simulated RMSE performance of the proposed scheme in comparison with individual narrowband estimations: (a) DOD and (b) DOA.

larger RMSE, as evident in the figure. Estimation at frequencies that are further from 10 GHz marked larger RMSE. Furthermore, searching the MUSIC spectrum at 0.5° also contributes to larger RMSE compared to the CRB curve. On the other hand, as shown in both Figs. 4.11 (a) and (b), estimates using the angle histograms yielded the best performance, where the RMSE curve was closest to the CRB. This result demonstrated the capability of using the proposed scheme in dealing with wide range of frequencies, and its better robustness to SNR compared to conventional narrowband methods.

In the following simulations, the performance of the proposed technique to detect two targets located at $(\phi_1, \theta_1) = (10^\circ, -28^\circ)$ and $(\phi_2, \theta_2) = (-10^\circ, -10^\circ)$ was simulated to demonstrate its capability of detecting multiple targets ($L > 1$). In this simulation, we used 50 snapshots, because we want to apply a fair comparison with experimental evaluations explained later in this chapter (hardware limitation prevented us taking more than 50 snapshots due to insufficient memory for capturing measurement data from the experimental equipments). Other parameters were the same with the previous simulations. Examples of two-dimensional MUSIC spectrum and the corresponding angle histograms obtained from the simulation are shown in Fig. 4.12. It can be observed that the MUSIC spectrum yielded two peaks corresponding to the targets positions. The angle histograms were plotted in Fig. 4.13. We could also see that the peaks of the angle histograms precisely estimated the DOD and DOA of both targets, indicating that the proposed scheme are also capable to handle multiple targets.

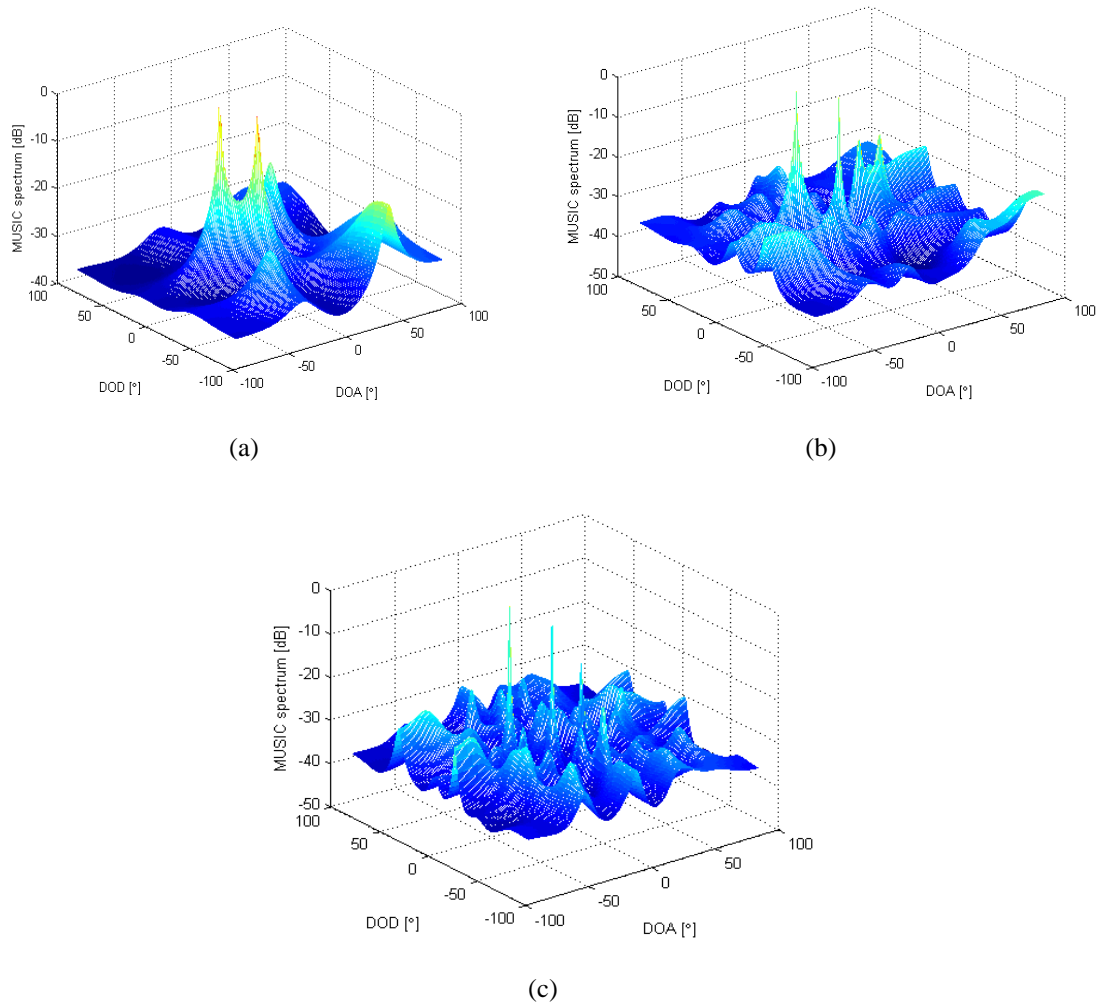


Fig. 4.12. Example of the simulated two-dimensional MUSIC spectrum angle histograms: (a) DOD and (b) DOA. ($M = N = 4$, $L = 2$, SNR = 15 dB, snapshot = 50).

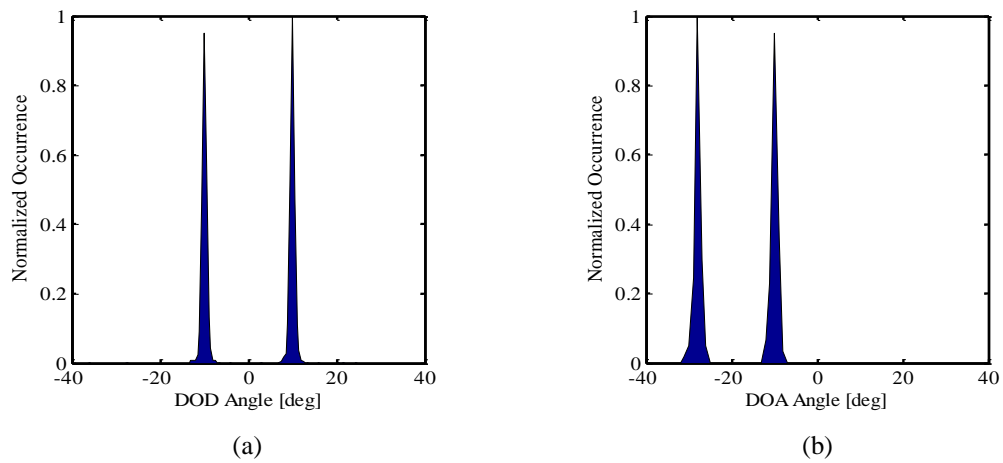


Fig. 4.13. Example of the formulated angle histograms ($M = N = 4$, $L = 2$, SNR = 15 dB, snapshot = 50) : (a) DOD and (b) DOA.

4.3.2. PERFORMANCE UNDERTAKING TARGETS WITH FLUCTUATING RADAR CROSS SECTIONS

This sub-section discusses the performance of the proposed scheme while detecting targets with fluctuating RCS. As the MIMO radar uses a UWB signal, the effectiveness of using the wide bandwidth will be demonstrated through numerical simulations, with comparison of using conventional narrowband scheme. As will documented in literatures, a fluctuating target yielded varying values of RCS when observed in different angles, due to its complex form factor and movement [2, 60]. In this study, we modeled the target RCS based on actual RCS measurement data using UWB signal. In order to show the advantages of using the wide bandwidth of the UWB signal, the RCS values at each frequency component will be taken into account. The performance of the proposed scheme will be shown while comparing the case of target with constant and fluctuating RCS, and the performance of conventional estimation algorithm using narrowband [36] and wideband signal, such as the spectrum averaging method [38].

The proposed algorithm was simulated according to the parameters listed in Table 4.1. As mentioned in the previous sections, the UWB signal considered in the proposed scheme contains multiple sinusoidal ranging from 3.1 to 10.6 GHz at 1 MHz intervals. Here, selection of the start and stop frequencies within the frequency range determines the total bandwidth of the signal used. The signal bandwidth is defined by

$$\text{Bandwidth} = f_H - f_L, \quad (4.9)$$

where f_H and f_L are the highest and lowest frequency components, respectively. The simulations will be conducted while varying the signal bandwidth from 10 to 1000 MHz, at different center frequencies, f_c , for example, from 3.6, 5, 8.4, to 10 GHz.

Two different scenarios were simulated, where the MIMO radar was detecting either a target with constant or fluctuating RCS. The target with constant RCS was modeled using a constant coefficient g , which was normalized to the value of SNR. For the targets with fluctuating RCS, we incorporated an RCS model based on actual measurements using UWB signal. This is because the existing RCS models such as the well known Swerling 1 to 4 models [2] only considers narrowband signals, where the RCS were modeled at a single frequency. In the case of a UWB MIMO radar, a model that considers the RCS throughout the UWB signal bandwidth is required. In this study, targets with fluctuating RCS were modeled by Weibull distribution, since it was shown in literatures that measured RCS of complex targets such as automobiles and small cars follows Weibull distribution [60]. Our measurement data [61] also showed that at a given observation angle, the RCS against

Table 4.1. Simulation parameters.

Parameters	Description
Total signal bandwidth	3.1 to 10.6 GHz (1 MHz interval)
Number of transmitting antennas, M	4
Number of receiving antennas, N	4
Number of targets, L	2
Signal to noise ratio, SNR	15 dB
Number of snapshots	50
Target positions	$(\phi_1, \theta_1) = (10^\circ, -28^\circ)$ $(\phi_2, \theta_2) = (-10^\circ, -10^\circ)$
Type of targets	Weibull targets

frequency (using 7 GHz bandwidth) also follows similar distribution (refer to Appendix B for examples of the analyses result for the RCS distribution of automobiles against frequency). Therefore, the targets considered in the simulation were modeled to have Weibull distributed RCS throughout the UWB frequency range, whose cumulative distribution function is given by

$$f(x) = \begin{cases} 1 - \exp^{-x/a)^b} & x \geq 0 \\ 0 & x < 0, \end{cases} \quad (4.10)$$

where a and b are the shape and scale parameters, respectively. The values of a and b were selected so as to equal the RCS medians of the Weibull target and the targets with constant RCS. Figure 4.14 plots the RCS versus frequency (expressed in signal power), and Fig. 4.15 depicts the corresponding cumulative distribution. We demonstrate the performance of the proposed scheme when detecting 2 targets located at $(\phi_1, \theta_1) = (10^\circ, -28^\circ)$ and $(\phi_2, \theta_2) = (-10^\circ, -10^\circ)$. The signal to noise ratio (SNR) was 15 dB, and the number of snapshot was 50.

The examples of simulated two-dimensional MUSIC spectra in two different frequencies experiencing different reflection coefficient g are shown in Fig. 4.16. Figure 4.16 (a) depicts the MUSIC spectrum at a frequency where no RCS fluctuations took place. We can see from the figure that the spectrum yielded two sharp peaks above the noise floor (around -35 dB), which corresponded to the target's angles. In contrast, the spectrum at a different frequency where there was 15 dB of RCS fluctuations as shown in Fig. 4.16 (b), the spectrum becomes distorted, an several spurious peaks appeared. The location of the peaks of the spectrum also shifted from the actual values. These factors will resulted in large DOD and DOA estimation errors at the particular frequency. That is why it is important to be able to utilize a wideband signal that consists of multiple frequency components, such

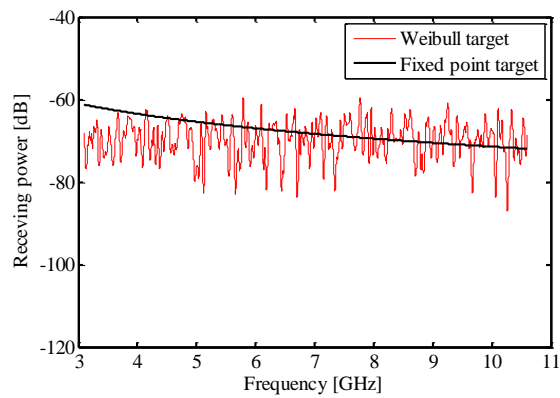


Fig. 4.14. Simulated RCS of a simulated Weibull target in comparison with a fixed point target considering propagation loss in frequency domain.

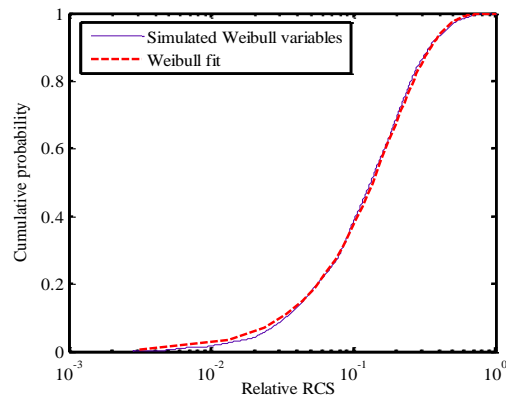


Fig. 4.15. Cumulative distribution of the simulated RCS of a Weibull target in frequency domain.

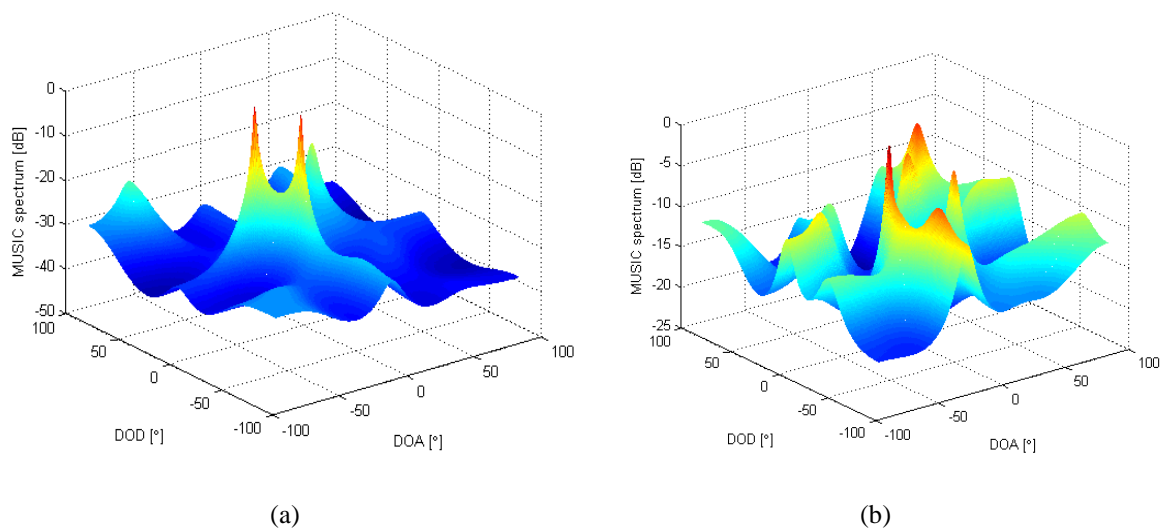


Fig. 4.16. Examples of simulated MUSIC spectra: (a) no RCS fluctuations and (b) RCS fluctuations of 15 dB.

as the proposed UWB signal, so that we could exploit the frequency diversity to improve our estimation accuracy.

Figures 4.17 and 4.18 show examples of the simulated angle histograms, obtained using the proposed scheme detecting targets with constant and Weibull RCS. Two cases of different signal bandwidth used to illuminate the targets were presented. Figure 4.17 shows the examples of simulated angle histograms at $f_c = 3.6$ GHz, when the MIMO radar was detecting the targets with constant RCS. It can be observed that the angle histograms were more or less similar when using either 1000 MHz or 50 MHz of signal bandwidths. Both cases marked sharp histogram peaks, which corresponds to the respective targets. This deduced that when detecting fixed point targets, the bandwidth has minimal effects on the angle estimation performance. The estimation using a 50-MHz signal bandwidth however, yielded an error of 1° . On the other hand, the angle estimation of the Weibull targets marked outstanding outliers in the angle histograms, particularly when using a 50-MHz signal bandwidth, as depicted in Fig. 4.18 (a). These outliers were attributable to spurious in the MUSIC spectrum due to small RCS values at certain frequencies. However, taking the majority decisions from the histograms, the targets were successfully estimated within 2° of estimation error. It was also shown in Fig. 4.18 (b) that by taking a larger bandwidth, for example 1000 MHz, the peaks of the outliers were suppressed compared to using a 50-MHz signal bandwidth.

The performance of the proposed scheme was evaluated in terms of average estimation error of the DOD and DOA, given by $\Delta\phi$ and $\Delta\theta$. Here,

$$\Delta\phi = \frac{1}{W} \sum_{w=1}^W |\phi - \phi_{est}| \quad (4.11)$$

$$\Delta\theta = \frac{1}{W} \sum_{w=1}^W |\theta - \theta_{est}|, \quad (4.12)$$

where W is the number of iterations, ϕ and θ are the actual DOD and DOA, and ϕ_{est} and θ_{est} are the estimated DOD and DOA, respectively. The estimation error against signal bandwidth using $f_c = 3.6$ GHz was plotted in Fig. 4.19, comparing the performance when detecting targets with constant and Weibull RCS, with 100 iterations and SNR = 15 dB. Comparison with a conventional spectra averaging method was also presented. It can be observed that the proposed scheme yielded improved estimation performance when taking larger signal bandwidth. This was true when detecting both type of targets, however, the improvement was more significant in the case of Weibull targets. On the other hand, the estimation error increased with larger bandwidth when conventional spectra averaging method was applied. This is attributed to large number of outliers which significantly influenced the averaging result. This result demonstrated the effectiveness of the proposed method in detecting targets with severely fluctuating RCS.

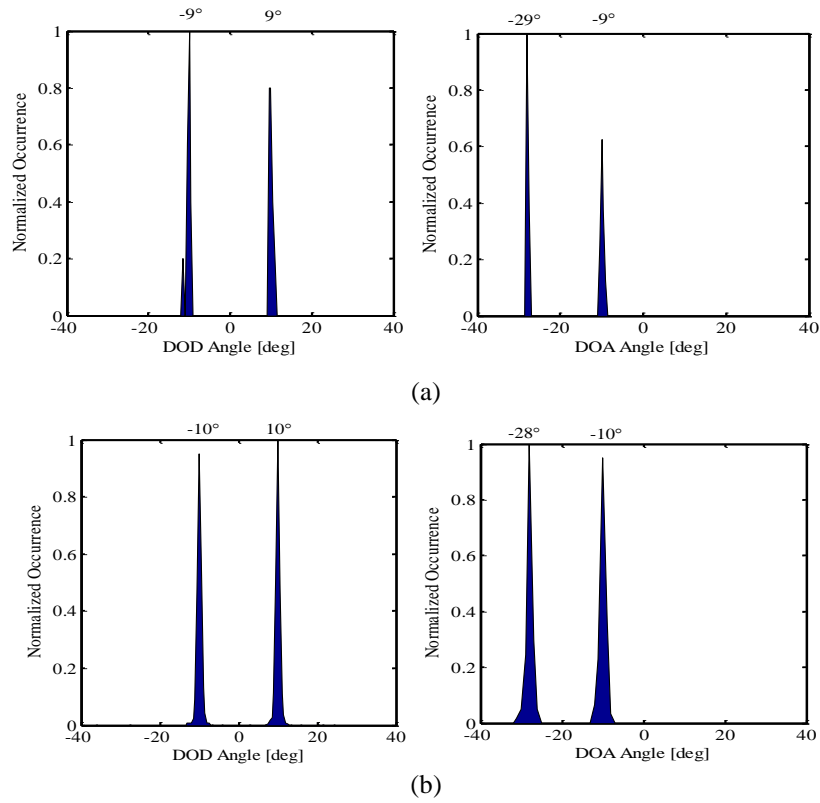


Fig. 4.17. Angle histograms of estimated DODs and DOAs in detecting targets with constant RCS using a signal bandwidth of: (a) 50 and (b) 1000 MHz.

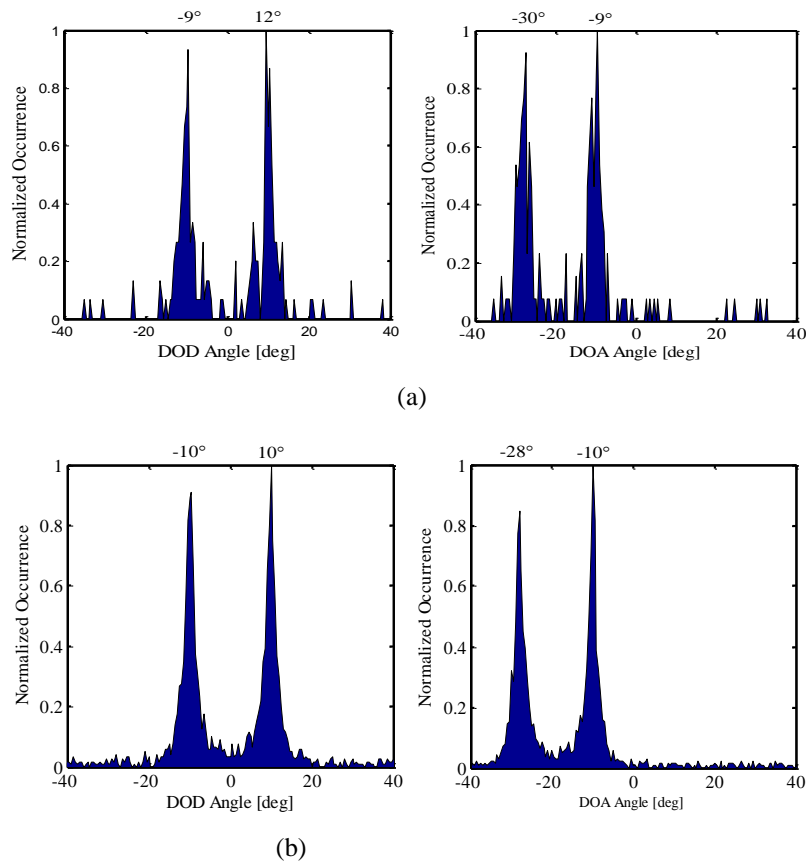


Fig. 4.18. Angle histograms of estimated DODs and DOAs in detecting Weibull targets using a signal bandwidth of: (a) 50 and (b) 1000 MHz.

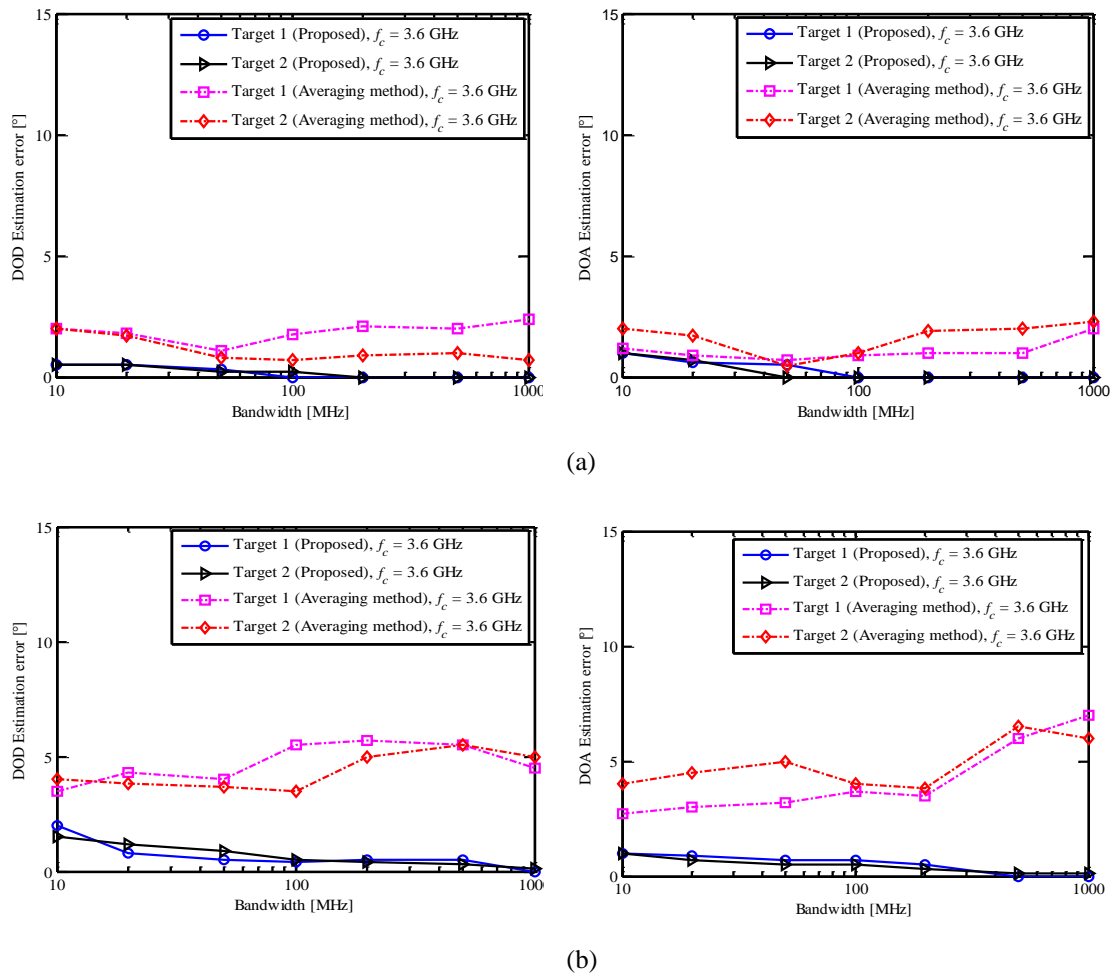
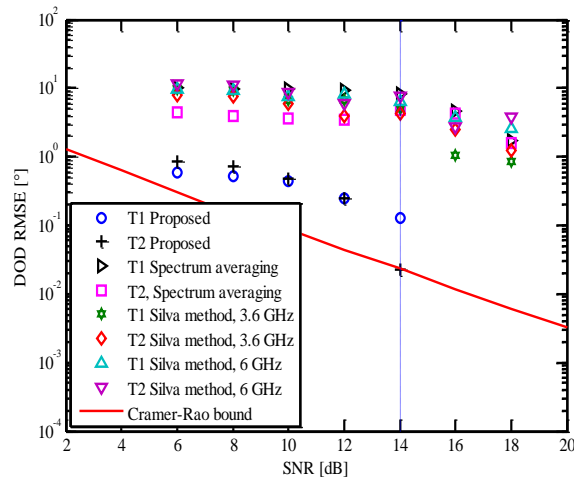
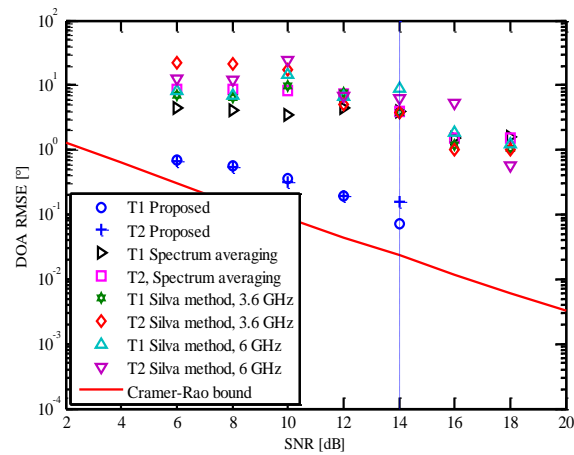


Fig. 4.19. Estimation errors against bandwidth while detecting targets with: (a) constant and (b) Weibull RCS.

The performance of the proposed scheme in terms of RMSE against SNR is plotted in Fig. 4.20. Performance of the spectrum averaging method, and another conventional method by Silva et. al [36] was also presented for benchmarking purposes. The Silva method adopted a two-way MUSIC algorithm to jointly estimate the DOD and DOA in MIMO radar using a narrowband signal. Simulation was carried out assuming all methods use a 4×4 MIMO non-uniform array detecting two Weibull targets. The performance of the proposed and spectrum averaging schemes were shown when they are using a 1000 MHz bandwidth with $f_c = 3.6$ GHz, while Silva method was presented at several frequencies (3.6 and 6.0 GHz) since it is a narrowband-based angle estimation. The performance bound calculated from the Cramér-Rao bound (CRB) when the DOD and DOA of a stationary target are estimated [32] individually were also plotted in the figure, given by Eq. (4.8)



(a)



(b)

Fig. 4.20. RMSE performance of the proposed scheme: (a) DOD and (b) DOA.

The impact of number of antennas on the performance of the proposed scheme was plotted in Fig. 4.21. The RMSE was computed in 50 independent trials against MN , when using a signal bandwidth of 1000 MHz and $\text{SNR} = 8$ dB and $L = 1$. Although M and N can take any number of positive integer, for the sake of simplicity, only specific cases of $M = N = 3, 4, 5$ and 6 were simulated. It is shown in the figure that increasing number of antennas yielded improvement in RMSE performance, even in the low SNR condition.

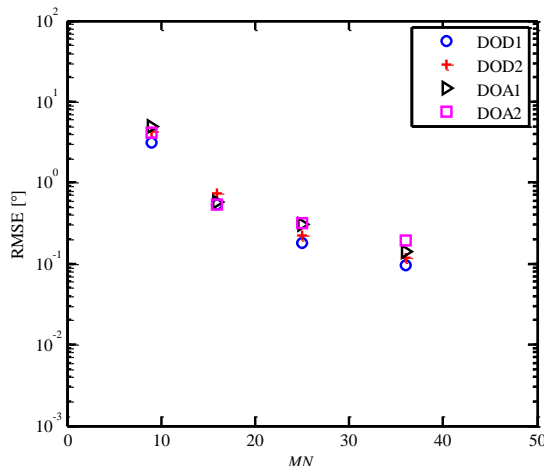


Fig. 4.21. RMSE of the proposed scheme against MN (Bandwidth = 1000 MHz, $L = 1$, $SNR = 8$ dB, target = Weibull).

4.4. EXPERIMENTAL EVALUATIONS IN RADIO ANECHOIC CHAMBER

Experiments were conducted to verify the results of the numerical simulations. The measurements were done in a radio anechoic chamber, using a measurement setup illustrated in Fig. 4.22. The setup consists of a vector network analyzer (VNA) and GPIB-controlled scanners which were used to virtually construct the MIMO arrays at both transmitting and receiving side. The VNA was used to generate UWB signals from 3.1 to 10.6 GHz in 1 MHz intervals, which were used as the transmitting signal. The total measurement points is 7501 which took approximately 10 minutes in the case of a 4×4 MIMO. The IF bandwidth setting of the VNA was set to 5 kHz, and the transmitting power to 5 dBm. The VNA was adopted due to its good calibration functions and time gating capability to cancel out direct coupling effects between transmitting and receiving antennas. Wideband horn antennas with average gain of 12.5 dBi were used as both transmitting and receiving antennas. The measurement scenario is depicted in Fig. 4.23. The SNR of the system is defined as the ratio of the receiving signal average power to the thermal noise. Figure 4.24 depicts the measured frequency domain data of the VNA, showing the case of 15 dB of average SNR. The time domain data of the VNA is shown in Fig. 4.25. We can see in the figure that two peaks appeared around 15 and 19 ns, which correspond to the reflection from the targets. The direct wave (supposed to be visible around 6 ns) was omitted from the measurement through the time-gating function of the VNA.

The setup were used to localize two targets positioned at $(\phi_1, \theta_1) = (10^\circ, -28^\circ)$ and $(\phi_2, \theta_2) = (-10^\circ, -10^\circ)$, similar with the condition in previous simulations. Two types of targets were used, which were conductive spheres, and complex shaped targets, both fabricated using polystyrenes and aluminum foil. The conductive spheres have 25 cm of diameters which yield RCS of

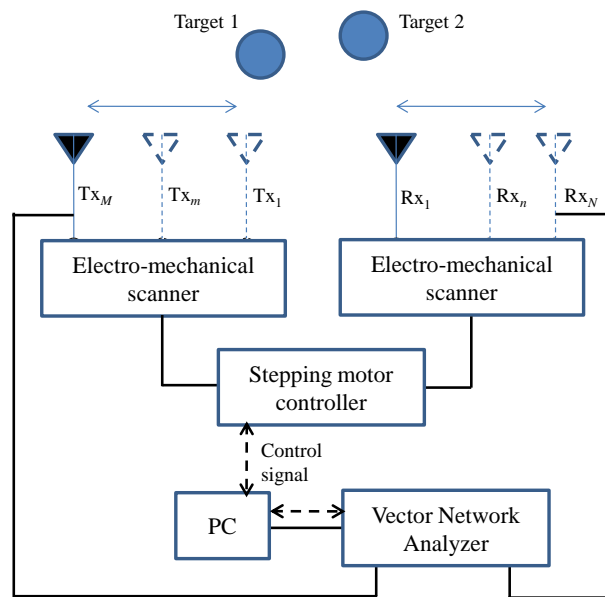


Fig. 4.22. Experimental setup for the measurement in radio anechoic chamber.

approximately -10 dBm^2 . The complex targets were used to emulate fluctuating RCS returns in the frequency domain. An example of the complex target is shown in Fig. 4.26. Figure 4.27 shows the measured frequency domain data of the complex targets, where ψ is the angle of observation. From the figure, we could observe that the receive signal fluctuates severely against frequency, compared to that of sphere targets. The complex targets marked several frequency regions with fluctuations of more than 15 dB at different angles, compared to sphere targets with only 5 dB of maximum fluctuations. The targets were positioned at 2.27 m (target 1) and 2.8 m (target 2) from the baseline of the transmitter and receiver.

The estimation errors from measurement campaign were plotted in Fig. 4.28. In the figure, the estimation errors were shown using signal bandwidths from 10 to 1000 MHz, and f_c of 3.6, 5.0 and 8.4 GHz. Data at 10 GHz was omitted for the sake of clarity of the figure. As demonstrated in the numerical simulations, the measurement results also indicated a decreasing trend in estimation errors with increasing signal bandwidth, especially in the case of complex targets. The estimation errors of complex targets were worse than the sphere targets, where maximum of 7° of estimation errors were observed. Both cases marked poorer performance compared to the simulations since the experimental measurement included plane wave modeling errors, and other maneuvering factors. Furthermore, no significant difference in estimation performance was observed when choosing different center frequencies.

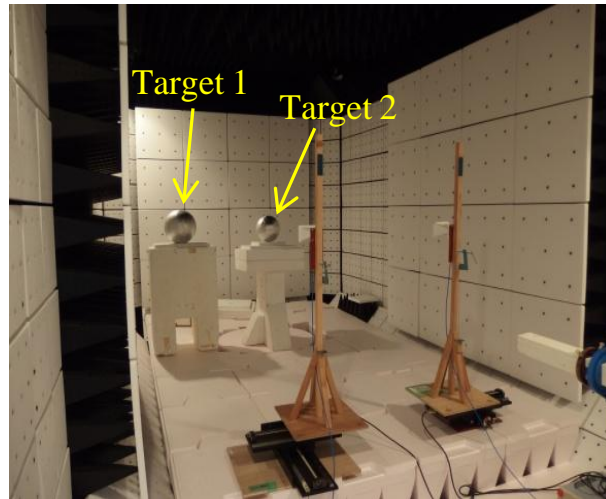


Fig. 4.23. Scenario of the measurement in a radio anechoic chamber.

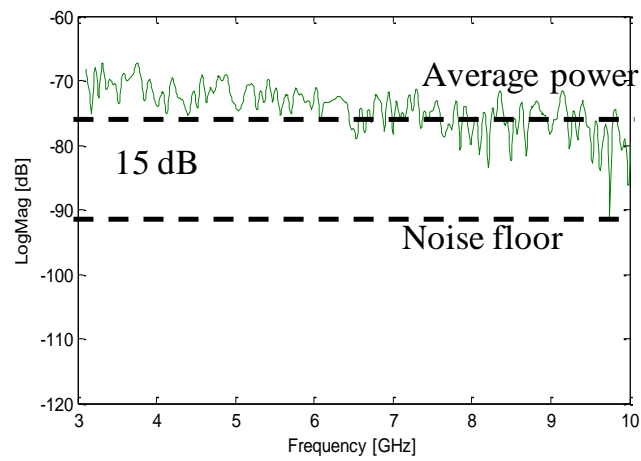


Fig. 4.24. The SNR definition during measurement based on frequency-domain data (spherical target).

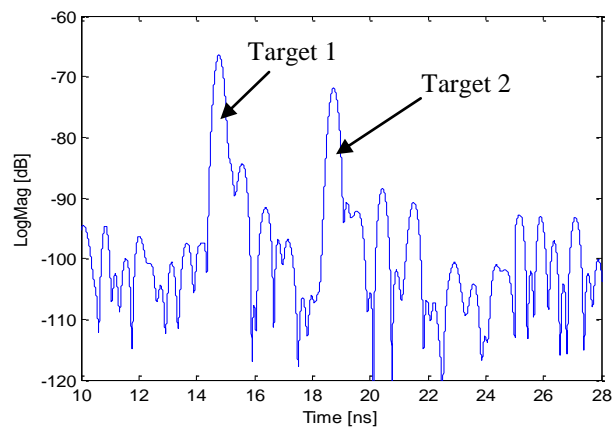


Fig. 4.25. The time-domain data of the VNA after applying time-gating.



Fig. 4.26. Example of a fabricated complex target.

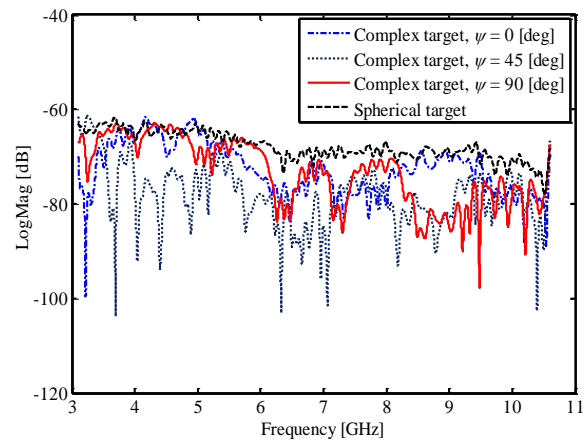


Fig. 4.27. Measured frequency-domain data of the fabricated targets.

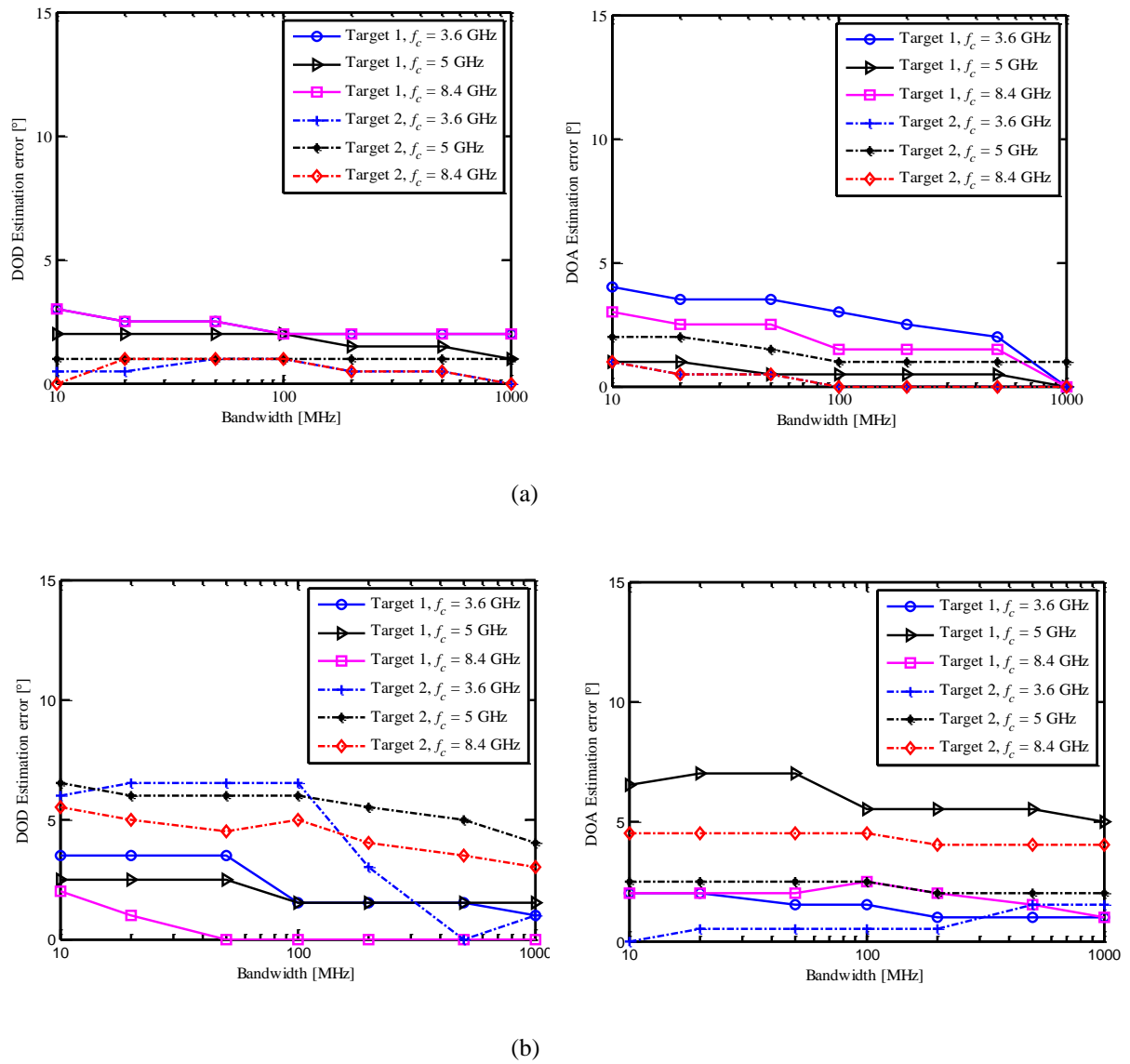


Fig. 4.28. Estimation errors against bandwidth obtained from measurements: (a) spherical and (b) complex targets.

An additional series of experiments was conducted to evaluate the localization performance of the proposed scheme. A single complex target was positioned in several locations in the radio anechoic chamber. The positions of the target are summarized in Table 4.2. The target was localized using the standard triangulation method, adopting the proposed scheme. In addition, localization using DOA and time-of-arrival (TOA) was also performed for comparison. The TOA/DOA proposed method uses the DOA formulated from majority decisions of estimations at each sub-frequency, and the TDOA were obtained from the time of arrival of the radar signal observed at Tx1-Rx1 antenna pair. The same MIMO array configuration as in previous experiments were utilized, and the number of snapshots was 50. Considering the target location in an x - y plane, the localization errors are defined as:

$$\Delta R = \sqrt{(\Delta x^2 + \Delta y^2)}, \quad (4.13)$$

where Δx and Δy is the ranging errors along the x and y axis. The results of the measurements were plotted in Fig. 4.29. In the case of triangulation, less than 1 m of error was obtained when using signal bandwidth of 1000 MHz. Using a 50-MHz signal resulted in lower accuracy. The TOA/DOA method also produced good results when using a 1000-MHz signal, and marked poor accuracy when using a 50-MHz bandwidth, due to low range resolution of TOA. Both localization methods showed slightly lower accuracy when the target is further away from the radar due to decrease in SNR.

TABLE 4.2. TARGET POSITIONS IN A RADIO ANECHOIC CHAMBER.

Target positions	Actual DOD and DOA	Target distance from radar
A	$(\phi, \theta) = (15^\circ, -43^\circ)$	1.5 m
B	$(\phi, \theta) = (-3^\circ, -24^\circ)$	2.2 m
C	$(\phi, \theta) = (-17^\circ, -1^\circ)$	3.0 m
D	$(\phi, \theta) = (-21^\circ, 5^\circ)$	3.3 m

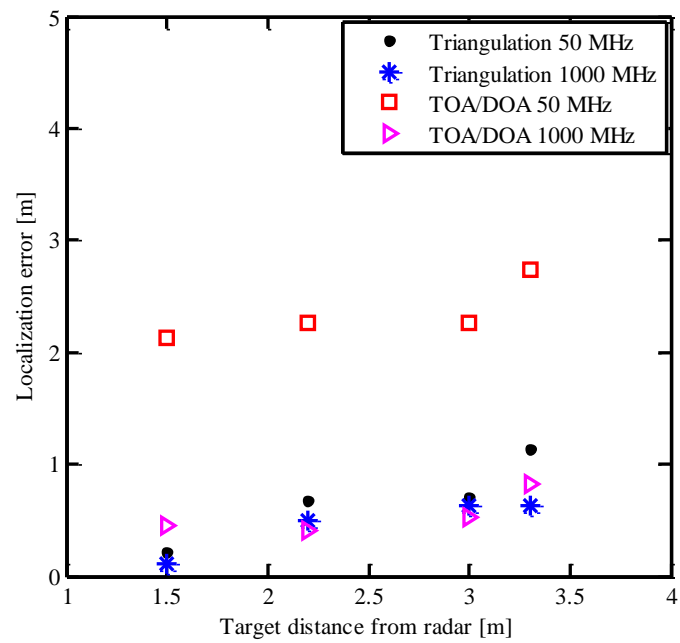


Fig. 4.29. Localization errors from measurements in a radio anechoic chamber.

4.5. SUMMARY

A new joint DOD and DOA estimation scheme in a UWB MIMO radar was proposed and described in this chapter. The scheme utilizes a UWB signal consists of multiple sinusoidal waves swept over the frequency bandwidth. Two-way MUSIC algorithm was adopted to estimate the DOD and DOA at each frequency component of the UWB signal, and combined them using majority decision. The majority decision was done by searching the peak of angle histograms which was formulated from the estimated DOD and DOA at all frequency component of the UWB signal.

First we mathematically derived the signal model of the proposed scheme, and discussed the complexity analysis compared to conventional wideband angle estimation scheme. Based on the analysis presented in the chapter, we identified that the proposed scheme requires a considerably heavy computation since two-dimensional search at each of the frequency component. However, the complexity converges with the conventional spectrum averaging method when the number of antennas and frequency components was large. The convergence was achieved because the SVD operation became dominant in the mentioned conditions for both cases. Furthermore, we also described the non-uniform MIMO array configuration used to construct a larger virtual MIMO array compared to the ULA case, for the sake of improving the performance of the angle estimation algorithm.

Numerical simulations and experimental evaluations were carried out to validate the performance of the proposed scheme. We have presented the performance of the proposed scheme in detecting targets with constant and a fluctuating RCS. From the investigation, it was found that the proposed scheme works well in detecting targets with constant RCS, and it clearly outperformed estimation using single frequencies (narrowband signals) in terms of RMSE versus SNR. Our simulations concluded that the proposed scheme is capable of utilizing the UWB signal in estimating the DOD and DOA of the both single and multiple targets scenarios. In the case of targets with fluctuating RCS (in this case Weibull distributed RCS against frequency), it was found that the proposed scheme performed better than the narrowband estimation, due to the benefit of frequency diversity using the UWB signal. We also found that it is essential to use larger signal bandwidth to reduce the estimation error using the proposed algorithm. When taking wider signal bandwidth, the usage of majority decisions from the angle histograms resulted in good estimation performance compared to the conventional spectrum averaging method. Experimental evaluation in a radio anechoic chamber verified the findings in our simulations.

We concluded based on the work that the proposed scheme was a suitable candidate to implement joint angle estimation in MIMO radar using ultra wideband signal. It was demonstrated that utilization of wider bandwidth in the proposed scheme leads to improvement of estimation performance, considering that the targets have fluctuating RCS in the frequency domain.

Chapter 5

ADAPTIVE TARGET LOCALIZATION SCHEME IN BISTATIC ULTRA WIDEBAND MULTIPLE-INPUT MULTIPLE-OUTPUT RADARS

5.1. INTRODUCTION

The previous chapter presented a joint DOD and DOA estimation scheme in UWB MIMO radars. It was shown that the proposed scheme marked good target localization performance due to the utilization of frequency diversity of the UWB signal. While we did not discuss the radar geometry earlier, depending on the actual operation conditions, the system may be monostatic or bistatic in principle. This is due to the fact that if the target distance is in similar order with the distance between the transmitting and the receiving array, the radar resembles a bistatic geometry [62], and vice versa. In monostatic radar, range resolution and target separation is determined by the transmission signal properties (e.g. signal bandwidth) and the characteristics of localization algorithm. However, in bistatic radar, the resolution and target separation also depends on positional relationship among the target, transmission and receiving stations.

The target localization in the bistatic case can be implemented through several methods, such as trilateration and triangulation. Trilateration uses the target range (generally based on TOA), and triangulation uses the target angles from the respective radar stations. These two methods yielded different range resolution depending on the positional relationship of the target (Refer Appendix C). Meanwhile, a conventional bistatic radar uses both the TOA and the target angles for target localization [62]. Each method has its own benefits and disadvantages depending on the positional relationship. Hence, better localization accuracy can be obtained if we are able to utilize the advantages of each methods effectively, according to the position of the target.

In this chapter, we proposed an adaptive method of target localization in a bistatic UWB MIMO radar, by using a combination of a DOD/DOA and a TOA/DOA based localization scheme. We extend the proposed joint DOD and DOA estimation scheme for UWB MIMO radars explained in Chapter 4, to also accommodate a TOA/DOA localization scheme using the same configuration of transmitting and receiving antennas. The idea was to implement a system that exploit the positional relations of the targets to adaptively select the either the DOD/DOA or the TOA/DOA method for localization. We will first explain the principle of proposed scheme in the next section, and we will show the performance while detecting target for different scenarios of target position through

numerical simulations and experimental evaluation. Finally, we will show the possibility of improving the localization accuracy.

5.2. PROPOSED SCHEME

A. DOD, DOA and TOA Estimation Method.

This section explains the UWB MIMO radar configuration and operational condition, and the algorithm used for estimating the DOD, DOA and the TOA. The MIMO radar consists of M transmitting and N receiving elements, illuminating target located at the far field of transmit and receive arrays. The transmitting and receiving arrays are separated by distance R_b . At the transmitting side, M orthogonal UWB signals are emitted, each consists of multiple sinusoidal waves swept over the UWB bandwidth. Here, we define the complex transmit signal waveform vector by $\mathbf{s}(t) = [s_1(t), \dots, s_M(t)]$, where each term containing K frequency components. The orthogonality between the transmit signals can be achieved through time division scheme.

For the DOD and DOA estimation, the same procedures as the scheme proposed in Chapter 4 were used, where narrowband estimation was done at each frequency component of the UWB signal and combined them through majority decision. The receiving signal of the k^{th} frequency component can be expressed by

$$\mathbf{x}_k(t) = [\mathbf{a}_t(\phi) \otimes \mathbf{a}_r(\theta)] \mathbf{s}^{(k)}(t) + \mathbf{z}(t), \quad (5.1)$$

where \otimes denotes the Kronecker product, \mathbf{a}_t and \mathbf{a}_r are the transmitting and receiving steering vectors, respectively, and θ are the corresponding transmitting and receiving angles, $\mathbf{s}^{(k)}(t)$ represents the k^{th} frequency component of the transmit signal vector $\mathbf{s}(t)$, and $\mathbf{z}(t)$ is the total additive white Gaussian noise. The receiving correlation matrix of the k^{th} frequency component is given by

$$\mathbf{R}_{xx_k} = E[\mathbf{x}_k(t) \mathbf{x}_k(t)^H], \quad (5.2)$$

where $E[\cdot]$ is the ensemble average, and $(\cdot)^H$ represents the conjugate transpose operation. The DOA and DOD estimation at the k^{th} frequency component can be estimated using conventional two way-MUSIC given by

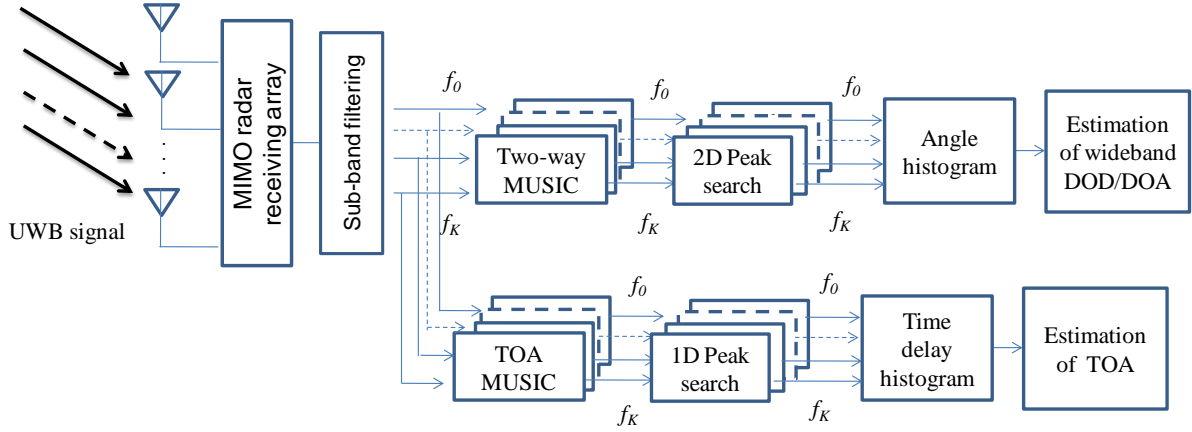


Fig. 5.1. Block diagram of the proposed scheme.

$$P_{\text{MU}_k}(\phi, \theta) = \frac{1}{[\mathbf{a}_t(\phi) \otimes \mathbf{a}_r(\theta)]^H \mathbf{e}_z^{(k)} \mathbf{e}_z^{(k)H} [\mathbf{a}_t(\phi) \otimes \mathbf{a}_r(\theta)]}, \quad (5.3)$$

Where $\mathbf{e}_z^{(k)}$ is the noise eigenvectors obtained from the eigen decomposition of the receive signal covariance matrix in Eq. (5.2). The DOD and DOA at each frequency component can be estimated from peak searching operation of the resulting two-dimensional MUSIC spectrum. Angle histograms are then formulated by combining the estimation results at all K frequency components of the UWB signal. Here the total number of estimated angles is given by KL , where L is the number of targets. The angle histogram can be viewed as a function of angle i from -90° to 90° at intervals of, for example, 0.1 deg. the peak angle is then given by

$$\hat{r}^{(i)} = \frac{1}{u} p^{(i)}, \quad (5.4)$$

where $p^{(i)}$ is number of occurrences of the angle i , and u is the normalized coefficient given by

$$u = \arg \max \hat{r}^{(i)}. \quad (5.5)$$

The peaks of the histograms correspond to the wideband DOD and DOA.

The TOA was also estimated by means of MUSIC algorithm, where the extended MUSIC for detecting TOA was applied. Since the receiving signal already contains multiple frequency components of the UWB signal, the MUSIC for TOA can be directly applied to detect the TOA. For the TOA estimation, the steering vector is replaced by the time delay vector given by

$$\mathbf{a}(\tau) = [\exp(-j2\pi f_1 \tau), \dots, \exp(-j2\pi f_k \tau), \dots, \exp(-j2\pi f_K \tau)], \quad (5.6)$$

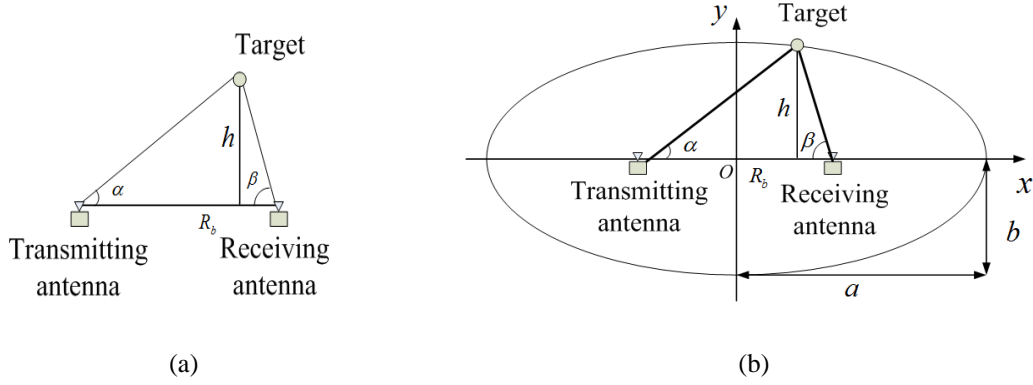


Fig. 5.2. Target localization methods: (a) DOD/DOA-based and (b) TOA/DOA-based.

where τ is the time delay between the transmitting and receiving reference antennas, f_k is the k^{th} frequency components used when sweeping the frequency. In this study, we chose the 1st transmitting and receiving antennas as the reference antennas, and f was chosen among 16 frequencies swept based on a center frequency f_c . Total of 16 frequency components was chosen because the it was sufficient to achieve considerably good MUSIC pseudo spectrum resolution of TOA, and larger K would lead to excessive computational burden. The f_c was decided by the k^{th} frequency component used in estimating the DOD and DOA. The MUSIC spectrum for TOA estimation is then formulated by

$$P_{MU}(\tau) = \frac{\mathbf{a}^H(\tau)\mathbf{a}(\tau)}{\mathbf{a}(\tau)\mathbf{e}_Z\mathbf{e}_Z^H\mathbf{a}(\tau)}, \quad (5.7)$$

where \mathbf{e}_Z is the noise eigenvectors obtained from the eigendecomposition of the receive signal covariance matrix. The peaks of the spectrum corresponds to the time of arrival τ of the impinging waves. The estimated TOA at all K frequencies (in our case $K = 16$) is then combined into time delay histograms in similar way with the DOD and DOA.

From the estimated DOD, DOA and TOA, the location of the target can be further localized and mapped to the x - y plane. The next section will describe the following two methods used to localize the target. The block diagram of the proposed scheme is depicted in Fig. 5.1.

B. DOD/DOA-Based

The target localization using the estimated DOD and DOA is shown in Fig. 5.2 (a). This method utilizes the angles α and β , which can be obtained from the DOD and DOA estimated from

the MUSIC algorithm, and the baseline length R_b between the transmitting and receiving antennas to calculate the vertical distance h to the target. Using the relationship between the angles within the triangle, the following equation can be derived:

$$R_b = \frac{h}{\tan \alpha} + \frac{h}{\tan \beta} \quad (5.6)$$

and hence

$$h = R_b \cdot \frac{\sin \alpha \sin \beta}{\sin(\alpha + \beta)}. \quad (5.7)$$

It is possible to estimate the target position (vertical range h from the baseline) by the angles from the transmitting and receiving antenna to be calculated from Eq. (5.7).

C. TOA/DOA-Based

For the TOD-DOA based method, the geometry in Fig. 5.2 (b) was considered. A locus maintaining $\tau = \text{constant}$ is an ellipse that has focal points $(-R_b/2, 0)$ and $(R_b/2, 0)$ at the reference transmitting and receiving antennas:

$$\frac{x^2}{a^2} + \frac{y^2}{b^2} = 1 \quad (5.8)$$

where

$$a = \frac{c\tau}{2} \quad (5.9)$$

(c is the velocity of electromagnetic wave) and

$$b = \sqrt{a^2 - (R_b/2)^2}. \quad (5.10)$$

The τ in Eq. (5.9) will use the estimated TOA using the MUSIC algorithm explained in the previous sub-section. The TOA here is defined by the traveling time τ of the radar signal between a reference transmitting and reference receiving antennas via the target. These antennas are selected among the multiple transmitting and receiving antennas. Finally, the location of the target is determined by an

intersection of the ellipse and a straight line that passes the receiving antenna and inclines at the β (obtained from estimated DOA) from the baseline, as shown in Fig. 5.2 (b).

5.3. NUMERICAL SIMULATION

A series of numerical simulations were conducted to evaluate the joint TOA, DOD and DOA estimation algorithm. The MIMO radar was simulated using both the DOD/DOA-based and the TOA/DOA-based method, detecting targets in two different scenarios emulating different positional relationship between the target range, and the transmitting and receiving antennas. A bistatic 4×4 MIMO radar using uniform linear array detecting two targets was considered. The targets were modeled to have RCS following Weibull distribution. Table 5.1 lists the major parameters of the simulation. Since the estimation accuracy depends on, the simulations were conducted in two different in Scenarios A and B, where different target distance h from the baseline was modeled. The baseline distance $R_b = 5$ m. This is because the estimation accuracy depends on $2h/R_b$ (refer Appendix C). The array spacing equaled 0.015 m.

The simulation results are shown in Figs. 5.3 and 5.4. Examples of the obtained histograms of TOA, DOD, and DOA for scenario A are shown in Fig. 5.2. It can be observed that the histograms marked yielded precise DOD, DOA and TOA estimations, with acceptable errors from the actual values. These peaks of the DOD, DOA and TOA were used to localize the target, by calculating the target range h using both the DOD/DOA-based and TOA/DOA-based methods.

Figure 5.4 shows the RMSE of estimated h for Scenarios A and B, plotted against SNR. The RMSE performance was calculated in 100 independent trials. In Scenario A, we used $h < 5$ m, which corresponds to $2h/R_b < 2$. For Scenario A, the TOA/DOA-based and the DOD/DOA-based method yielded similar order of performance, as shown in Fig. 5.4 (a). The DOD/DOA-based method however marked slightly better performance in higher SNR region, for example, at SNR 6 dB and above, the DOD/DOA-based requires 2 dB less SNR to achieve the same performance with the TOA/DOA-based method. This may be due to the face that the localization using the TOA/DOA based includes errors from both the TOA and DOA estimations.

In Scenario B, $h > 30$ m was used, corresponding to $2h/R_b > 12$. In this case, the TOA/DOA-based method always outperformed the DOD/DOA-based, as shown in Fig. 5.4 (b). The RMSE was one order smaller than the DOD/DOA-based method at all SNR. The accuracy obtained with the TOA/DOA-based method was approximately independent of the distance.

Table 5.1. Simulation parameters

Parameters	Description
Bandwidth	3.1 to 4.6 GHz
Array configuration	4×4 uniform linear array
Number of targets	2
Target locations	
Scenario A	$\left\{ \begin{aligned} (\phi_1, \theta_1) &= (-10^\circ, -28^\circ), h_1 = 2.81 \text{ m} \\ (\phi_2, \theta_2) &= (10^\circ, -10^\circ), h_2 = 2.84 \text{ m} \end{aligned} \right.$
Scenario B	$\left\{ \begin{aligned} (\phi_1, \theta_1) &= (-4.8^\circ, -4.8^\circ), h_1 = 30.0 \text{ m} \\ (\phi_2, \theta_2) &= (0.0^\circ, -8.2^\circ), h_2 = 35.0 \text{ m} \end{aligned} \right.$
SNR	-10 to 10 dB
Number of snapshots	50
RCS model	Weibull
Number of trials	100

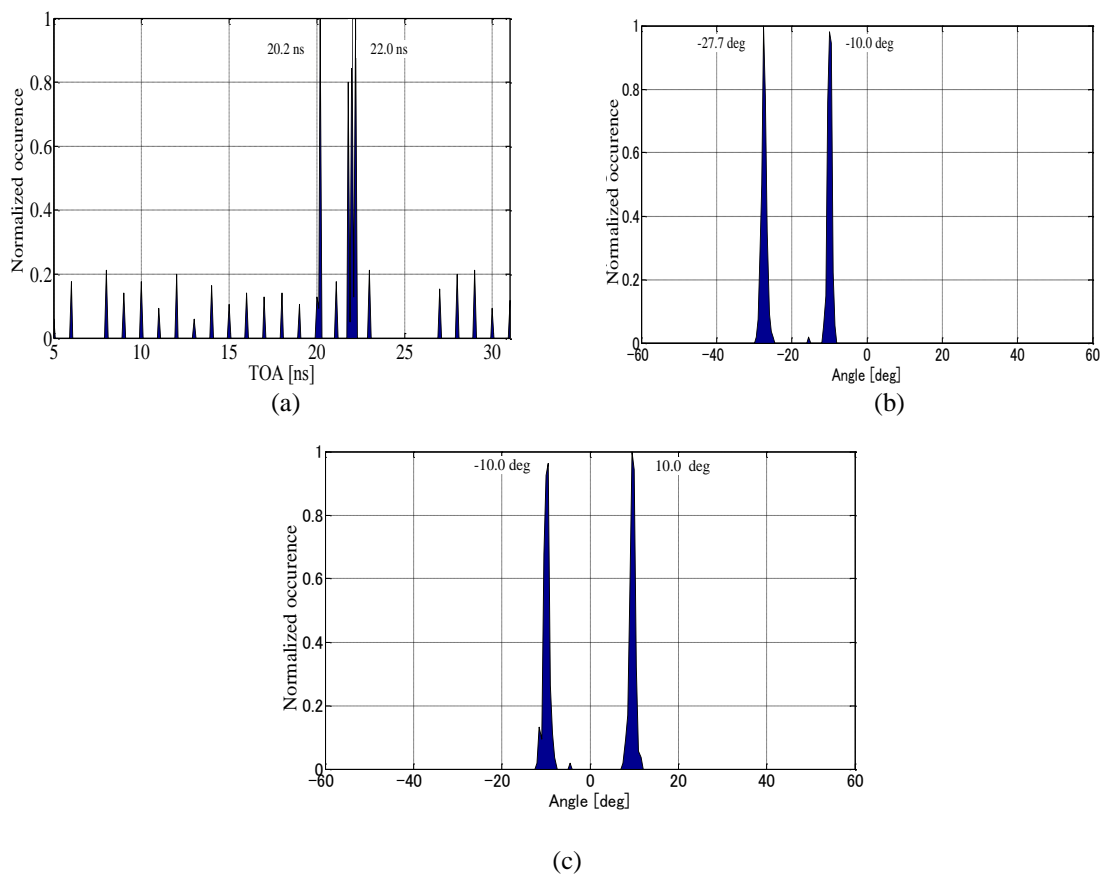


Fig. 5.3. Example of simulated angle and distance histograms in Scenario A (SNR = 10 dB): (a) TOA, (b) DOD and (c) DOA.

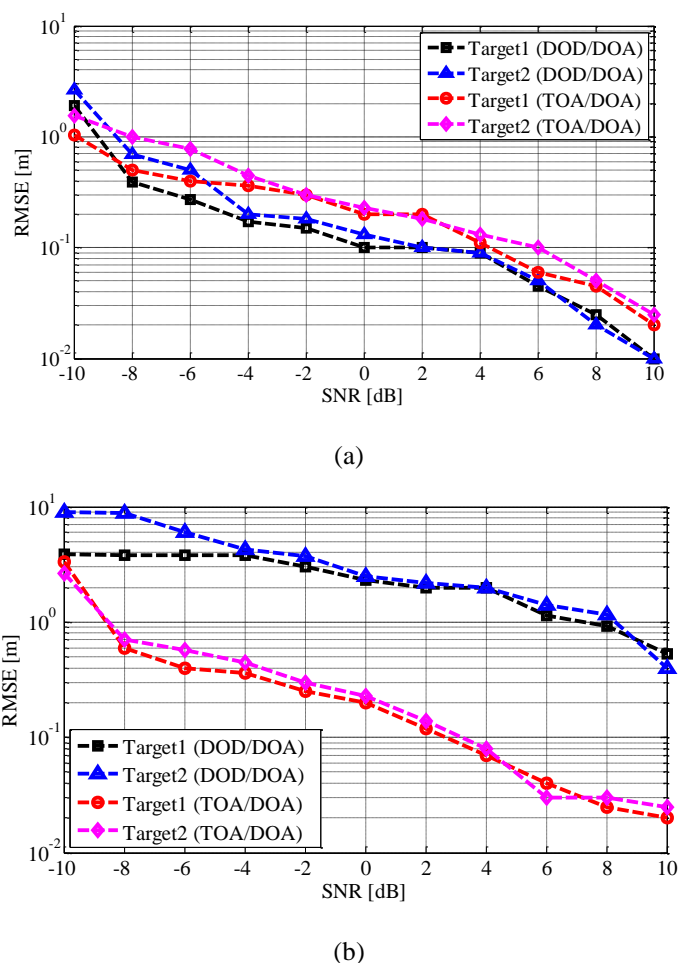


Fig. 5.4. RMSE against SNR: (a) Scenario A and (b) scenario B.

5.4. EXPERIMENTAL EVALUATION

Experimental evaluation was conducted to verify the simulation results. Similar experimental setup as explained in Section 4.4 was used for the experiments since the setup was capable of realizing the proposed scheme as the TOA estimation routine was added in the post-measurement offline processing. Table 5.2 lists the experimental parameters. Since the size of the anechoic chamber was limited, we only reproduced the conditions similar to scenario A in the previous simulation. Antenna configuration, and target location were the same as scenario A in the simulation. Similarly, this experiment also uses a pseudo-MIMO system which was constructed by moving the antenna using electro-mechanical scanners, and by repeating the measurement of each transmitting and receiving antenna pair. Two conductive spheres were used as the radar targets.

The experimentally-derived TOA, DOD, and DOA histograms roughly reproduced the simulated results described in section 4, as shown in Fig. 5.4. The estimated distances from the baseline to the targets 1 and 2 were 2.79 and 2.84 m with the DOD/DOA-based method, and 2.69 and 2.91 m with the TOA/DOA-based, respectively. The estimation errors were one-order larger using the TOA/DOA-based than the DOD/DOA-based. As the simulated result, the experiment also showed that the DOD/DOA-based performed slightly better than the TOA/DOA when the $2h/R_b$ is small (in this case $2h/R_b = 1$).

Table 5.2 Experimental parameters

Parameters	Description
Bandwidth	3.1 to 4.6 GHz
Frequency sweep of VNA	1501 points, 1 MHz interval
Array configuration	4×4 Uniform Linear Array
Target locations	$(\phi_1, \theta_1) = (-10^\circ, -28^\circ), d_1 = 2.81$ m $(\phi_2, \theta_2) = (10^\circ, -10^\circ), d_2 = 2.84$ m
Number of targets	2
SNR	10 dB
Number of snapshots	50
Antennas	UWB horn antennas

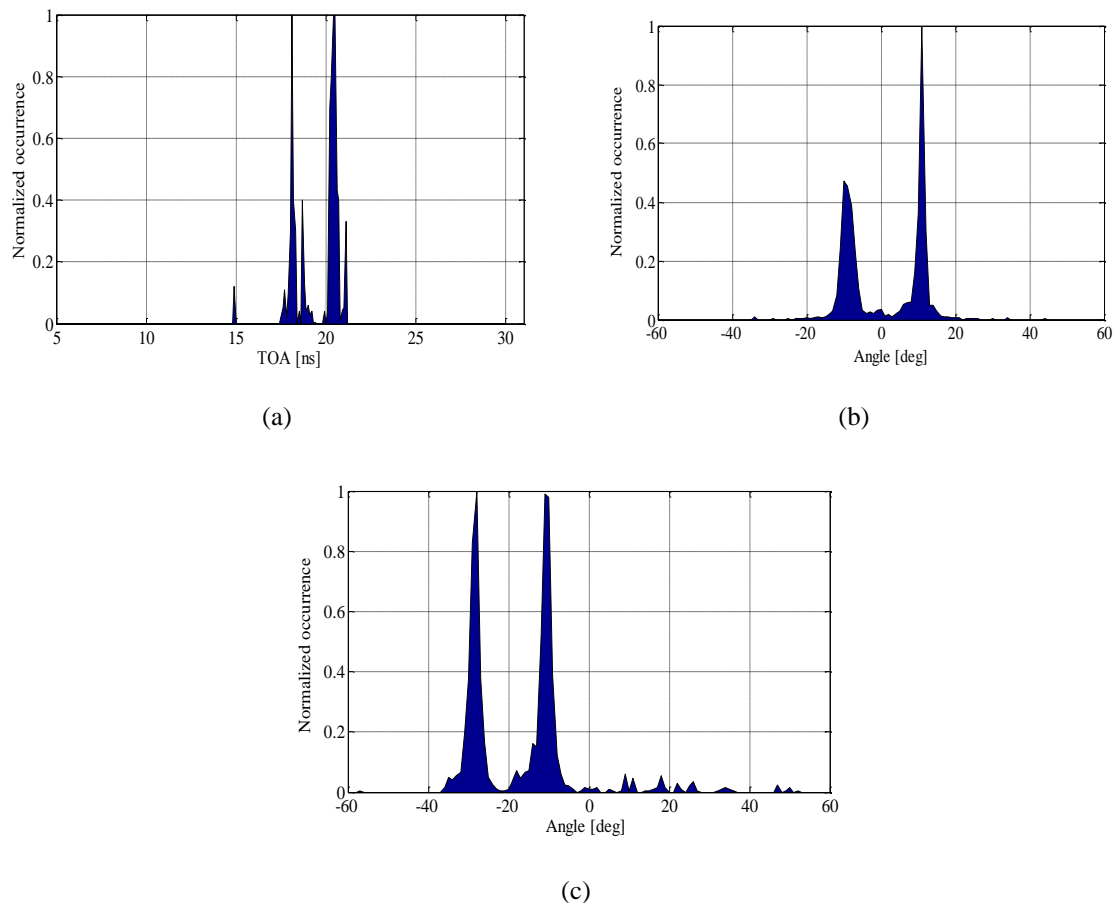


Fig. 5.5. Angle and distance histograms in obtained from measurement in a radio anechoic chamber: (a) TOA, (b) DOD and (c) DOA.

5.5. DISCUSSION OF RESULTS AND PROPOSAL OF ADAPTIVE LOCALIZATION SCHEME

A. Localization accuracy

From the previous results from the numerical simulations and experimental evaluation, we have demonstrated that the localization accuracy using the DOD/DOA-based and TOA/DOA-based methods depend on the positional relationship of the targets and the baseline connecting the transmitting and receiving antennas. Specifically, we observed that the DOD/DOA-based yielded slightly better accuracy when the target was relatively close to the baseline. The TOA/DOA-based are superior when the target was relatively far. In order to the ability of both the localization method, we propose an implementation of adaptive scheme that selects the optimum method based on the estimated target range h during the initial scan. The system will evaluate the values of h , and adaptively selects the optimum localization method based on formulated values of $2h/R_b$, as depicted

in Fig. 5.6. The adaptive scheme is considered to be able to capitalize the benefit of selecting the better method to localize the target based on its range to the radar, and hence improving the accuracy of the system. It is worth to note that this discussion did not consider the effects of signal bandwidth and grazing angle of the target. Although the DOD/DOA-based are only slightly better than the TOA/DOA-based at close range ($2h/R_b$ is relatively small), the TOA estimation are limited by the signal bandwidth, hence the accuracy will worsen when using a narrower signal bandwidth. Furthermore, the accuracy of the localization scheme does not only depend on the h , but also on the angle of the target due to the usage of linear array configuration. It was known that the accuracy worsen when the incident wave impinged a linear array at a low grazing angle (angle almost parallel to the baseline of the radar) [62-64]. The evaluation and discussion of these factors on the system performance will be included in future works of the study.

B. Computational Complexity

Considering the dimensions of the covariance matrix is $u \times v$, and the total K frequency components used, as described in section 4.2-C, the computational complexity of the DOD/DOA-based in terms of the singular value decomposition SVD costs $O(K\{u^2v + v^3\})$, where $u = MM$ and $v = NN$ in the case of the UWB MIMO radar. The searching algorithm and majority decision routine cost $O(i^2KL)$, and $O(2\{i+K\}) + O(2\{iL\})$, respectively. Here, i is the number of bin during search operations. On the other hand, the TOA/DOA-based using the same MIMO radar configuration requires both the TOA and the DOA estimation routine. The TOA estimation individually costs $O(K\{u^2v + v^3\})$ for the SVD operation, and $O(iKL)$ for the peak search as it only requires one-dimensional search. The majority decision requires $O(i+K) + O(iL)$. On top of this, the DOA estimation further consumes $O(K\{u^2v + v^3\}) + O(iKL) + O(i+K) + O(iL)$. This differs from the DOD/DOA estimation, where the i in the second term is in the order of 1, since only the DOA is needed for localization. Table 5.3 summarizes the complexity analysis of the proposed scheme. Figure 5.7 plots the computational complexity versus the number of antenna MN . It can be observed that the the MIMO radar using the DOD/DOA-based have larger complexity than using the TOA/DOA-based when MN is smaller than 60. Meanwhile, the TOA/DOA-based marked higher complexity when MN is larger than 60. From this result, we can conclude that the utilization of the adaptive localization scheme at larger MN can reduce the computational complexity of the overall system, particularly by selecting the DOD/DOA-based when the target is close to the radar. Constantly using only the TOA/DOA-based method requires larger computation resources, and on the other hand, using only the DOD/DOA-based suffers from accuracy point of view when the target is relatively far.

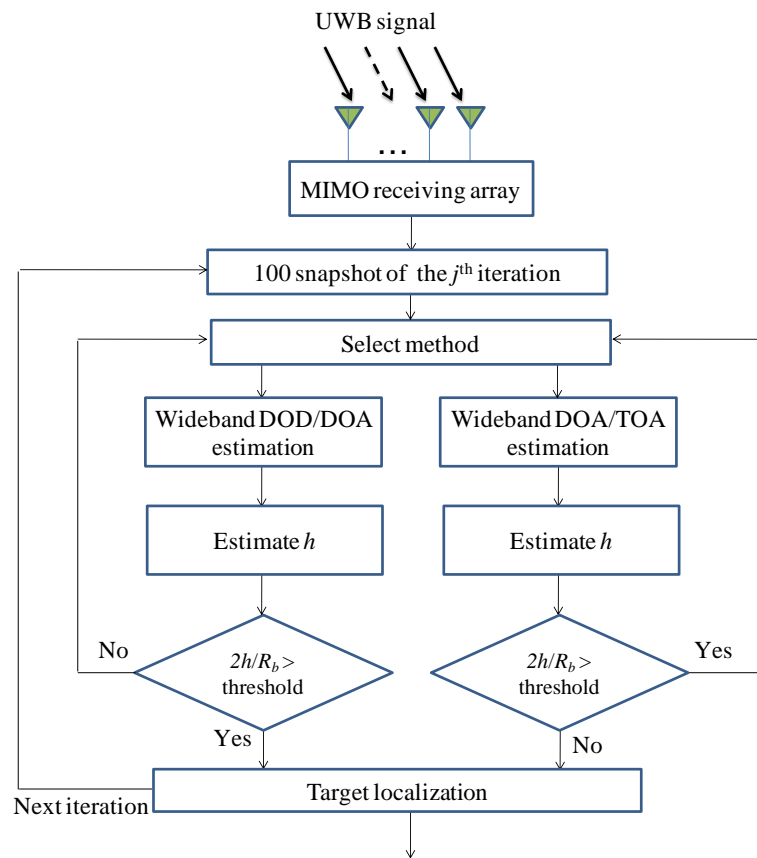


Fig. 5.6. Block diagram of the proposed adaptive target localization scheme.

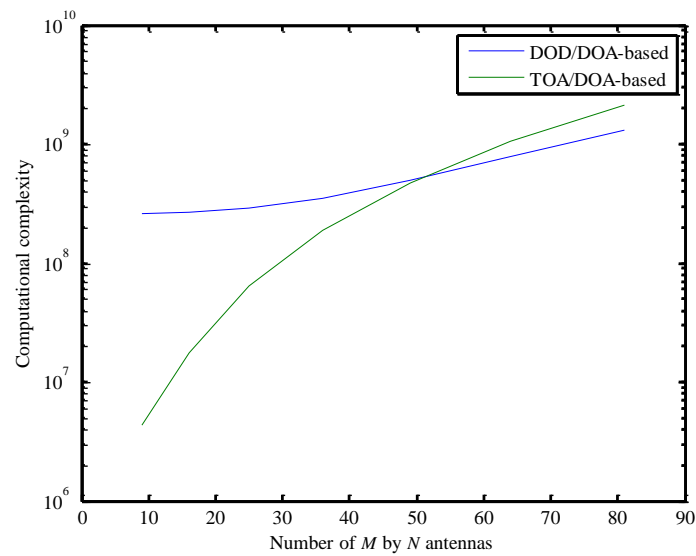


Fig. 5.7. Comparison of computational complexity of the proposed DOD/DOA-based and TOA/DOA based method.

Table 5.3. Computational complexity of DOD/DOA-based and TOA-DOA-based method.

DOD/DOA-based	$O(K\{u^2v + v^3\}) + O(i^2KL) + O(2\{i+K\}) + O(2\{iL\})$
TOA/DOA-based	$2 \times \{O(K\{u^2v + v^3\}) + O(iKL) + O(i+K) + O(iL)\}$

5.6. SUMMARY

In this chapter we presented a proposal of an adaptive target localization method in a bistatic UWB MIMO radar. The localization scheme were developed based on the previously proposed joint DOD and DOA estimation scheme for wideband signal, and combined with a TOA arrival using MUSIC algorithm which were done simultaneously. The radar system localizes a target location based on the estimated DOD, DOA and TOA, using two types of algorithm, namely the DOD/DOA-based, and the TOA/DOA based.

We first evaluated the performance of both the DOD/DOA-based and TOA/DOA based method in terms of the localization accuracy, in two separate scenario of target relative range from the radar baseline. Numerical simulations revealed that the performance of the DOD/DOA-based was degraded when the vertical range perpendicular to the radar baseline increased, while that of the TOA/DOA-based method was almost independent of range. In short range (perpendicular range from the baseline was relatively smaller), the localization errors were numerically and experimentally found within a similar order for the two methods; the TOA/DOD-based method outperformed when the range was very short about and SNR was high. Finally, we described our proposal of adaptive localization method that selects either one of the localization method based on the target range from the baseline. By adaptively selecting the optimum localization in each scan will improve the final target localization accuracy.

We have also evaluated the computational complexity of both the DOD/DOA-based and the TOA/DOA-based. Our analysis concluded that in the case of large number of antennas ($MN > 60$), the TOA/DOA-based method requires larger computation resources, while the DOD/DOA-based marked larger complexity when using smaller number of antennas. Hence, adaptively selecting either of the method contributes to the reduction of computational complexity, compared to constantly using only either one of them. Further investigation regarding the impact of signal bandwidth and DOA at low grazing angle on the localization performance will be the focus of our future works.

Chapter 6

CONCLUSIONS

6.1. SUMMARY OF THESIS

In this thesis, numerical and experimental studies concerning the detection performance and target localization in UWB MIMO radars were presented.

We first described the study on jitter effects on the performance of spatial MIMO radar systems. A deterministic simulation in the time domain was developed to model an m-sequences-based MIMO radar system with three types of processing scheme namely the MIMO, RPNR and DRN. The detection performance was evaluated considering the presence of time and phase jitters in the MIMO radar receivers, and derived the probability of detection for each case of joint processing scheme. It was observed that the effects of timing jitter on the detection performance of MIMO radar were negligible when a non-coherent MIMO and DRN processing scheme were used. However, the detection performance of RPNR scheme degraded significantly when the standard deviation of the timing jitter was 1 % of the ideal clock. Secondly, it was shown that phase jitter at the local oscillator of each receiver directly degraded the SNR yielding similar probability of detection of the MIMO radar system, regardless of processing scheme chosen. It can be concluded from the results that the performance degradation due to phase jitter were negligible if the amount of jitter was limited to below 0.1 radian. Nevertheless, the effects of phase jitter may become significant when using a large MIMO array in conditions with low SNR margin. We also presented a MIMO radar testbed system developed for experimental evaluation in a radio anechoic chamber.

We then explained a new joint DOD and DOA estimation method in UWB MIMO radars in for improved target localization. The proposed scheme, were based on a two-dimensional MUSIC algorithm extended for MIMO radar using a UWB signal. The idea was to treat the UWB signal as a summation of sinusoidal waves swept throughout the UWB frequency. The DOD and DOA were estimated at each of the frequency component of the UWB signal, and combined through majority decision. The majority decision was a non-parametric approach that takes the histograms of the estimated DODs and DOAs. Numerical simulations along with experimental evaluations were conducted to evaluate the performance of the proposed scheme. It was found that in detecting targets with fluctuating RCS (in this case Weibull distributed RCS against frequency), it is essential to use large signal bandwidth to reduce the estimation error using the proposed algorithm. When taking wider signal bandwidth, the usage of majority decisions from the angle histograms resulted in good estimation performance compared to the conventional spectrum averaging method. We consider based

on the results obtained that the proposed scheme was a suitable candidate to implement joint angle estimation in MIMO radar using ultra wideband signal.

Finally, we extend our previously proposed joint DOD and DOA estimation scheme into an adaptive target localization method in bistatic UWB MIMO radars. The localization scheme combined the previously proposed estimation scheme for wideband signal with simultaneous TOA estimation using MUSIC algorithm. The radar system localizes a target location based on the estimated DOD, DOA and TOA, using two types of algorithm, namely the DOD/DOA-based, and the TOA/DOA based. We first showed through numerical simulations that the performance of the DOD/DOA-based was degraded when the range increased, while that of the TOA/DOA-based method was almost independent of the range. Experimental evaluation in a radio anechoic chamber was carried out to validate the simulation results. Although the space constraint of the radio anechoic chamber limited us to only reproduce the conditions of short-range targets, the result showed similar trend as the simulation in the particular case, where the DOD/DOA-based performs slightly better than the TOA/DOA-based method. Based on these results we proposed an adaptive localization method that selects either one of the localization method based on the target range from the baseline. In addition, the analysis of the computational complexity indicated that when the number of antennas MN is relatively large ($MN > 60$), the TOA/DOA-based method requires larger computation resources, while the DOD/DOA-based marked larger complexity when using smaller number of antennas. Hence, adaptively selecting either of the method contributes to the reduction of computational complexity, compared to constantly using only either one of them. By adaptively selecting the optimum localization in each scan will improve the final target localization accuracy.

6.2. FUTURE WORKS

We have shown the experimental evaluation of the proposed scheme based on measurement setup developed using the combination of VNA and electro-mechanical scanners. The VNA was capable to transmit and receive the fullband UWB signal due to its wide dynamic range of frequency sweeping. The quality of the receiving signal was also guaranteed due to the internal calibration function of the VNA. Nevertheless, it is not practical to use the developed measurement setup in real-time radar systems due to its high costs (particularly at high frequencies) and limitation of off-line processing. If an efficient real-time processing scheme is available for both the transmitting and receiving side of the MIMO radar, the proposed joint DOD and DOA estimation holds a great promise for implementation. One potential scheme capable of transmitting and receiving multiple frequency components is the OFDM scheme. Many existing wireless communication standards are adopting the

OFDM scheme [65-67]. The OFDM scheme exploits fast fourier transform (FFT) and the inverse FFT (IFFT) to efficiently assign and extract useful data to each of the frequency component of the signal. For example, in radio communication application, an angle histogram was adopted as narrowband interference detection of wideband OFDM scheme [68]. Similarly, the exploitation of the OFDM scheme can be one of the solutions for implementing the proposed joint DOD and DOA estimation in practical systems. However, the reliability, efficiency and the performance of the system need to be further studied, as one of the future work of the study.

In terms of algorithm point of view, we have analyzed the computational complexity of the proposed joint DOD and DOA estimation scheme compared to an existing spectrum averaging scheme. Although the resource required for both of them are in similar order (in cases where MN is sufficiently large), since the scheme utilizes a wideband signal, the complexity of the proposed algorithm increases with increasing frequency components of the radar signal used for detecting the targets. Therefore, we are looking for an alternative processing method that can reduced the complexity of the algorithm, without significantly degrading the estimation performance. Several methods were proposed in literature such as by using a reduced processing of the narrowband estimation algorithm [37, 69], however, we need to examine their compatibility with the proposed system and suitability in dealing with severely fluctuating targets. Furthermore, introducing adaptive frequency (sub-carrier) selection into the localization scheme could also improve the performance. While the selection technique may be useful if the RCS against frequency do not rapidly fluctuates within a specific scanning time (or generally referred to scan to scan fluctuation), severe fluctuations would still becomes a problem. In these kind of cases, it may be beneficial to consider algorithm such as compressive sensing [70].

REFERENCES

- [1] G. Galati, *Advanced Radar Techniques and Systems*. London: The Institution of Electrical Engineers, 1993.
- [2] M. I. Skolnik, *Introduction to Radar Systems*, 2nd ed. New York: McGraw-Hill College, 1980.
- [3] E. Fishler, A. Haimovich, R. S. Blum, L. J. Cimini, Jr., D. Chizhik, and R. A. Valenzuela, "Spatial diversity in radars-models and detection performance," *IEEE Trans. Signal Process.*, vol. 54, pp. 823-838, 2006.
- [4] A. M. Haimovich, R. S. Blum, and L. J. Cimini, "MIMO radar with widely separated antennas," *IEEE Signal Process. Magazine*, vol. 25, pp. 116-129, 2008.
- [5] L. Jian and P. Stoica, "MIMO radar with colocated antennas," *IEEE Signal Process. Magazine*, vol. 24, pp. 106-114, 2007.
- [6] J. Li and P. Stoica, *MIMO Radar Signal Processing*. New Jersey: Wiley, 2009.
- [7] V. S. Chernyak, "On the concept of MIMO radar," in *2010 IEEE Radar Conf.*, pp. 327-332, 2010.
- [8] R. C. Dixon, *Spread Spectrum Systems with Commercial Applications*, 3rd ed. New York: Wiley, 1994.
- [9] K. W. Forsythe, D. W. Bliss, and G. S. Fawcett, "Multiple-input multiple-output (MIMO) radar: performance issues," in *Eighth Asilomar Conf. on Signal, Systems and Computers*, pp. 310-315, 2004.
- [10] S. Zazo, B. Bejar, and J. Grajal, "Virtual MIMO radar using OFDM-CDM waveforms," in *2008 IEEE Radar Conf.*, pp. 1-5, 2008.
- [11] D. W. Bliss and K. W. Forsythe, "Multiple-input multiple-output (MIMO) radar and imaging: degrees of freedom and resolution," in *Seventh Asilomar Conf. on Sig., Systems and Computers*, pp. 54-59, 2003.
- [12] E. Fishler, A. Haimovich, R. Blum, R. Cimini, D. Chizhik, and R. Valenzuela, "Performance of MIMO radar systems: advantages of angular diversity," in *Eighth Asilomar Conf. on Signal, Systems and Computers*, pp. 305-309, 2004.
- [13] N. H. Lehmann, A. M. Haimovich, R. S. Blum, and L. Cimini, "High resolution capabilities of MIMO radar," in *Asilomar Conf. on Signal, Systems and Computers*, pp. 25-30, 2006.
- [14] H. Godrich, A. M. Haimovich, and R. S. Blum, "Cramer Rao bound on target localization estimation in MIMO radar systems," in *Annual Conf. on Information Sciences and Systems*, pp. 134-139, 2008.

-
- [15] T. Aittomaki and V. Koivunen, "MIMO radar direction finding performance using Swerling model," in *Asilomar Conf. on Signal, Systems and Computers*, pp. 518-522, 2008.
- [16] R. S. Blum, "Limiting case of a lack of rich scattering environment for MIMO radar diversity," *IEEE Signal Process. Lett.*, vol. 16, pp. 901-904, 2009.
- [17] Y. Yang and R. S. Blum, "MIMO radar waveform design based on mutual information and minimum mean-square error estimation," *IEEE Trans. Aerosp. and Electron. Syst.*, vol. 43, pp. 330-343, 2007.
- [18] B. Friedlander, "Waveform design for MIMO radars," *IEEE Trans. Aerosp. and Electron. Syst.*, vol. 43, pp. 1227-1238, 2007.
- [19] T. Hayashi, N. Kikuma, H. Hirayama, and K. Sakakibara, "A consideration of performance improvement of location estimation of scatterers in MIMO radar," in *2012 Int. Symposium on Antennas and Propag.*, pp. 1144-1147, 2012.
- [20] T. Yardibi, L. Jian, P. Stoica, X. Ming, and A. B. Baggeroer, "Source localization and sensing: A nonparametric iterative adaptive approach based on weighted least squares," *IEEE Trans. Aerospace and Electronic Systems*, vol. 46, pp. 425-443, 2010.
- [21] L. Fulai and W. Jinkuan, "AD-MUSIC for jointly DOA and DOD estimation in bistatic MIMO radar system," in *2010 Int. Conf. on Computer Design and Applications*, pp. V4-455-V4-458, 2010.
- [22] L. Jianfeng and Z. Xiaofei, "Unitary reduced-dimensional estimation of signal parameters via rotational invariance techniques for angle estimation in monostatic multiple-input multiple-output radar with rectangular arrays," *IET Radar, Sonar & Navigation*, vol. 8, pp. 575-584, 2014.
- [23] W. Wei, W. Xianpeng, and L. Xin, "Propagator method for angle estimation of non-circular sources in bistatic MIMO radar," in *2013 IEEE Radar Conf.*, pp. 1-5, 2013.
- [24] I. Pasya, N. Iwakiri, and T. Kobayashi, "Joint direction-of-departure and direction-of-arrival estimation in a UWB MIMO radar detecting targets with fluctuating radar cross sections," *Int. Journal of Antennas and Propag.*, vol. 2014, pp. 1-15, 2014.
- [25] S. Kong, S. Lee, C. Y. Kim, and S. Hong, "Wireless cooperative synchronization of coherent UWB MIMO radar," *IEEE Trans. Microwave Theory and Techniques*, vol. 62, pp. 154-165, 2014.
- [26] M. Z. Dooghabadi, H. A. Hjortland, and T. S. B. Lande, "A linear IR-UWB MIMO radar array," in *2013 IEEE Int. Conf. on Ultra-Wideband*, pp. 13-19, 2013.
- [27] S. O. Rice, "Mathematical analysis of random noise," *Bell System Tech. Journal*, vol. 23, pp. 282-332, 1944.
- [28] J. Capon, "High-resolution frequency-wavenumber spectrum analysis," *Proc. IEEE*, vol. 57, pp. 1408-1418, 1969.

-
- [29] R. O. Schmidt, "Multiple emitter location and signal parameter estimation," *IEEE Trans. Antennas and Propag.*, vol. 34, pp. 276-280, 1986.
- [30] R. Roy and T. Kailath, "ESPRIT-estimation of signal parameters via rotational invariance techniques," *IEEE Trans. Acoustics, Speech and Signal Process.*, vol. 37, pp. 984-995, 1989.
- [31] J. Rissanen, "Modeling by shortest data description," *Automatica*, vol. 14, pp. 465-471, 1978.
- [32] H. L. V. Tree, *Optimum Array Processing*. New York: Wiley, 2002.
- [33] C. C. Yeh, L. Ju-Hong, and C. Yih-min, "Estimating two-dimensional angles of arrival in coherent source environment," in *1988 Int. Conf. on Acoustics, Speech, and Signal Process.*, pp. 2909-2912, 1988.
- [34] W. Guangmin, X. Jingmin, Z. Nanning, and A. Sano, "Computationally efficient subspace-based method for two-dimensional direction estimation with L-shaped array," *IEEE Trans. Signal Process.*, vol. 59, pp. 3197-3212, 2011.
- [35] X. Maohui, D. Ruiyan, L. Cai, and L. Jin, "An effective array for 2-D direction-of-arrival estimation," in *2006 Int. Conf. on Innovative Computing, Information and Control*, pp. 370-373, 2006.
- [36] P. D. Silva and C. K. Seow, "Performance of MIMO radar using two-way MUSIC," in *2013 Progress in Electromagnetics Research Symposium*, 2013.
- [37] Z. Xiaofei, X. Lingyun, X. Lei, and X. Dazhuan, "Direction of departure (DOD) and direction of arrival (DOA) estimation in MIMO radar with reduced-dimension MUSIC," *IEEE Commun. Lett.*, vol. 14, pp. 1161-1163, 2010.
- [38] M. Fujimoto, S. Ohaka, and T. Hori, "DOA estimation without antenna characteristics calibration for UWB signal by using sub-band processing," in *2010 IEEE Int. Conf. on Wireless Information Technology and Systems*, pp. 1-4, 2010.
- [39] X. H. Wu, A. A. Kishk, and A. W. Glisson, "MIMO-OFDM radar for direction estimation," *IET Radar, Sonar & Navigation*, vol. 4, pp. 28-36, 2010.
- [40] S. Hyoungh-Chang and Y. Byung-woo, "Direction finding of wideband sources in sparse arrays," in *2002 Sensor Array and Multichannel Signal Process. Workshop*, pp. 518-522, 2002.
- [41] Y. Ogawa, N. Hamaguchi, K. Ohshima, and K. Itoh, "High-resolution analysis of indoor multipath propagation structure," *IEICE Trans. Communications*, vol. E78-B, pp. 1450-1457, 1995.
- [42] Y. Kuwahara and Y. Nakamura, "A high-resolution algorithm for analysis of multipath propagation structure," in *IEEE Antennas and Propag. Society Int. Symposium*, pp. 364-367, 1998.
- [43] C. Haowen, L. Xiang, J. Weidong, and Z. Zhaowen, "MIMO radar sensitivity analysis of antenna position for direction finding," *IEEE Trans. on Signal Processing*, vol. 60, pp. 5201-5216, 2012.

-
- [44] M. Akcakaya and A. Nehorai, "MIMO radar detection and adaptive design under a phase synchronization mismatch," *IEEE Trans. Signal Process.*, vol. 58, pp. 4994-5005, 2010.
- [45] C. Daniel. (2013, 15 March 2013). *Jitter Visualization, Part 1: Random Jitter*, 2013.
- [46] "Jitter and Jitter Testing for Modulator Drivers," New Focus Inc Application Note, 2002.
- [47] "Universal Serial Bus Specification Revision," 27 April 2000.
- [48] P. V. Brennan, A. Narayanan, and R. Benjamin, "Grating lobe control in randomised, sparsely populated MIMO radar arrays," *IET Radar, Sonar & Navigation*, vol. 6, pp. 587-594, 2012.
- [49] Y. Bobin, W. Wenjie, and Y. Qinye, "DOD and DOA estimation in bistatic non-uniform multiple-input multiple-output radar systems," *IEEE Commun. Lett.*, vol. 16, pp. 1796-1799, 2012.
- [50] G. Zheng, M. Yang, W. Guo, and B. Chen, "Joint DOD and DOA estimation for bistatic polarimetric MIMO radar," in *2012 IEEE 11th Int. Conf. on Signal Process.*, pp. 329-332, 2012.
- [51] M. A. Haleem, A. Haimovich, and R. S. Blum, "Sidelobe mitigation in MIMO radar with multiple subcarriers," in *2009 IEEE Radar Conf.*, pp. 1-6, 2009.
- [52] Z. Xiaodong, A. G. Yarovoy, T. Savelyev, and L. Ligthart, "Modified Kirchhoff migration for UWB MIMO array-based radar imaging," *IEEE Trans. Geoscience and Remote Sensing*, vol. 48, pp. 2692-2703, 2010.
- [53] M. S. Mercan, A. Caliskan, and E. Ozturk, "Through wall imaging with MIMO UWB radar," in *2013 Signal Process. and Commun. Applications Conf.*, pp. 1-4, 2013.
- [54] N. Iwakiri, "Ultra-wideband bi-directional space-time multiple-input multiple-output channel estimation schemes based on measurements," Ph.D. dissertation, Graduate School of Advanced Science and Technology, Tokyo Denki University, 2008.
- [55] D. Wilcox, M. Sellathurai, and T. Ratnarajah, "Subspace methods and spatial diversity in radars," in *2008 IEEE Radar Conf.*, pp. 1-5, 2008.
- [56] V. Mangulis, "Frequency diversity in low-angle radar tracking," *IEEE Trans. Aerospace and Electronic Systems*, vol. AES-17, pp. 149-153, 1981.
- [57] J. J. Zhang and A. Papandreou-Suppappola, "MIMO radar with frequency diversity," in *2009 Int. Waveform Diversity and Design Conf.*, pp. 208-212, 2009.
- [58] W.-Q. Wang, "Virtual antenna array analysis for MIMO synthetic aperture radars," *Int. Journal of Antennas and Propag.*, vol. 2012, pp. 1-10, 2012.
- [59] G. H. Golub and C. F. V. Loan, *Matrix Computation*, Third ed. Baltimore: John Hopkins University Press, 1996.
- [60] W. Buller, B. Wilson, L. van Nieuwstadt, and J. Ebling, "Statistical modelling of measured automotive radar reflections," in *2013 IEEE Int. Instrumentation and Measurement Technology Conf.*, pp. 349-352, 2013.

-
- [61] T. Kobayashi, N. Takahashi, M. Yoshikawa, K. Tsunoda, and N. Tenno, "Measurement of automobile UWB radar cross sections at Ka band," in *Ultra-Wideband, Short-Pulse Electromagnetics 7*, ed New York: Springer, pp. 586-592, 2007.
- [62] M. I. Skolnik, "An Analysis of Bistatic Radar," *Aerospace and Navigational Electronics, IRE Transactions on*, vol. ANE-8, pp. 19-27, 1961.
- [63] R. M. Shubair and R. S. Nuaimi, "Displaced sensor array for improved signal detection under grazing incidence conditions," *Progress in Electromagnetics Research*, vol. 79, pp. 427-411, 2008.
- [64] J. Ding, H. W. Chen, X. Li, and Z. Zhuang, "Fluctuating target detecting in low grazing angle with MIMO radar," *Progress in Electromagnetics Research*, vol. 141, pp. 79-98, 2013.
- [65] E. Perahia, "IEEE 802.11n development: history, process, and technology," *IEEE Commun. Magazine*, vol. 46, pp. 48-55, 2008.
- [66] A. Greenspan, M. Klerer, J. Tomcik, R. Canchi, and J. Wilson, "IEEE 802.20: Mobile broadband wireless access for the twenty-First century," *IEEE Commun. Magazine*, vol. 46, pp. 56-63, 2008.
- [67] E. Karapistoli, F. N. Pavlidou, I. Gragopoulos, and I. Tsetsinas, "An overview of the IEEE 802.15.4a standard," *IEEE Commun. Magazine*, vol. 48, pp. 47-53, 2010.
- [68] N. Iwakiri and T. Kobayashi, "Channel estimator employing narrowband interference detector of wideband OFDM receiver," *IEICE Trans. Fundamentals*, vol. E93-A, pp. 2648-2653, 2010.
- [69] J. Li, X. Zhang, and W. Chen, "Root-MUSIC based angle estimation for MIMO radar with unknown mutual coupling," *Int. Journal of Antennas and Propag.*, vol. 2014, p. 8, 2014.
- [70] W. Zhang, W. Liu, J. Wang, and S. Wu, "Joint transmission and reception diversity smoothing for direction finding of coherent targets in MIMO radar," *IEEE Journal of Selected Topics in Signal Process.*, vol. 8, pp. 115-124, 2014.

ACKNOWLEDGMENT

I would like to express my gratitude to my supervisor, Professor Takehiko Kobayashi, for accepting me as his postgraduate student, for the opportunity to work on this project, and also for his support and confidence in my work. His vast experience and deep knowledge of the subject proved to be immense help to me. Without his guidance and invaluable time spent with me in this project, this thesis would not have been completed successfully. I would like to thank Professor Yutaka Kaneda, Professor Takao Matsumoto, Professor Susuki Tsuyoshi, and Dr. Naohiko Iwakiri as referees for this dissertation, and for fruitful discussions for improving the contents.

Huge gratitude for the Ministry of Education, Culture, Sports, Science and Technology (MEXT) of Japan, for the financial sponsorship provided. I would also like to thank Universiti Teknologi MARA, Malaysia, for promoting me to enroll in this doctoral program, and for the financial support given to me throughout this study period. I would not have been able to be here without the support of these two institutions. Finally, I want to thank my beloved wife, and family who have been offering all round support during the period of my study.

Idnin Pasya bin Ibrahim

APPENDICES

APPENDIX A

MIMO RADAR TESTBED MEASUREMENT EQUIPMENTS SPECIFICATION.

Table A.1. Orthogonal modulator specification.

Manufacture	Hittite
Model	HMC497LP4
Frequency range	100~4000 MHz
IFport bandwidth	DC~700 MHz
Output power	+3 dBm
Amp	differential amplification

Table A.2. Orthogonal demodulator specification

Manufacture	Hittite
Model	HMC597LP4
Frequency range	100~4000 MHz
IF port bandwidth	DC~600 MHz
Conversion gain	-3.5 dBm

Table A.3. Broadband horn antenna specification

Frequency	2 – 18 GHz
VSWR	< 2.5:1
Average antenna gain	9.5 dBi
3dB Beam width	60 度

Table A.4. Power amplifier specification.

Gain	30 dB
Frequency	700 – 4200 MHz

Table A.5. Low noise amplifier specification.

Gain	15 dB
Frequency	2 – 20 GHz
Noise Figure	3.5 dB

Table A.6. Noise generator specification.

Frequency	10MHz – 10 GHz
Power	-17 dBm

APPENDIX B

DISTRIBUTION OF MEASURED RCS OF AUTOMOBILE AGAINST FREQUENCY

This document describes the distribution of measured RCS of automobile in a radio anechoic chamber using UWB signal from 22 to 27 GHz. The original measurement data was done by collaboration between Tokyo Denki University, Tokyo Institute of Technology and National Institute of Communication Technology (NICT) in measurement facility of NICT. Figure 8.1 shows example of the measurement scenario, where we could see that an automobile was positioned inside the anechoic chamber, and the RCS was measured while rotating the aspect angle. We further analyzed the data to study the distribution of the RCS along the frequency domain. The distribution of RCS observed against frequency was plotted in Figs. B.2 to B.5.



(a)



(b)

Fig. B.1. Example of RCS measurement scenario of automobile in a radio anechoic chamber observing from: (a) 180° and (b) 225° .

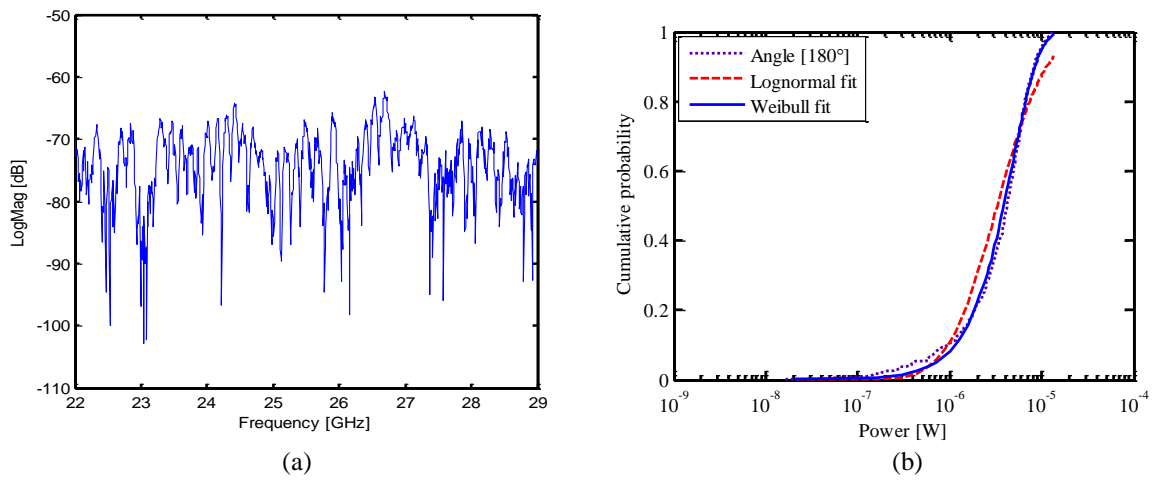


Fig. B.2. RCS of automobile against frequency, measured at angle 180° : (a) Measured raw data and (b) distribution fitting result.

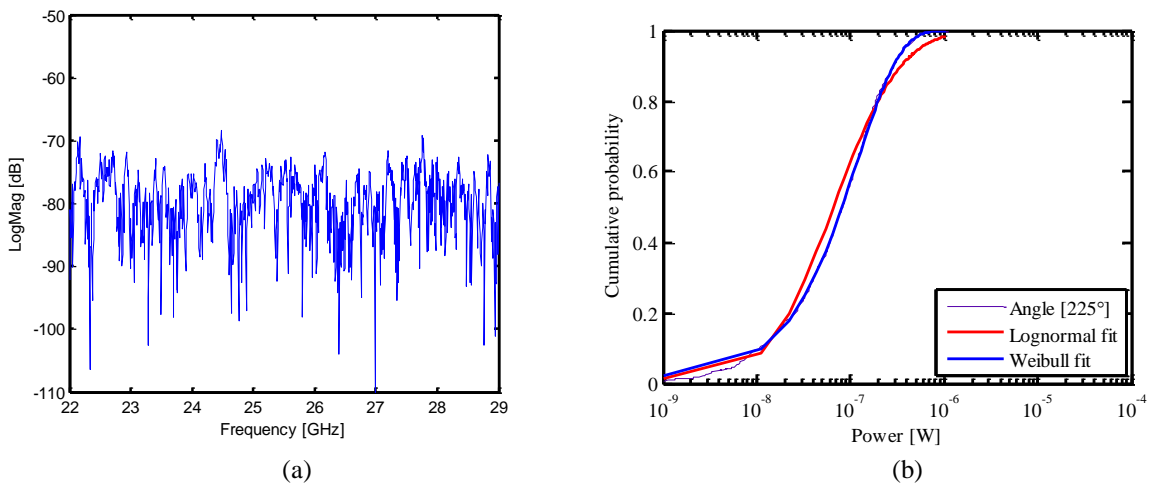


Fig. B.3. RCS of automobile against frequency, measured at angle 225° : (a) Measured raw data and (b) distribution fitting result.

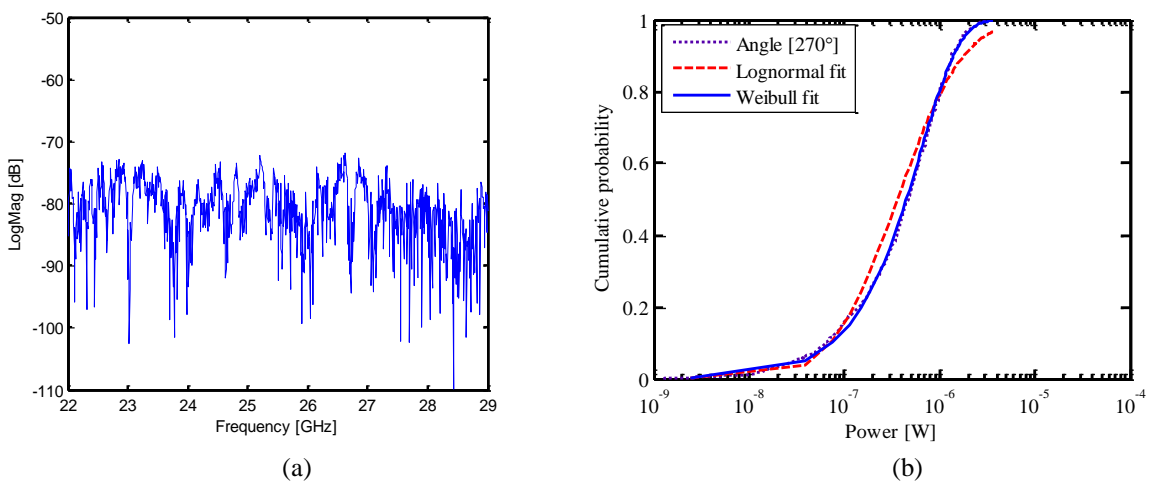


Fig. B.4. RCS of automobile against frequency, measured at angle 270° : (a) Measured raw data and (b) distribution fitting result.

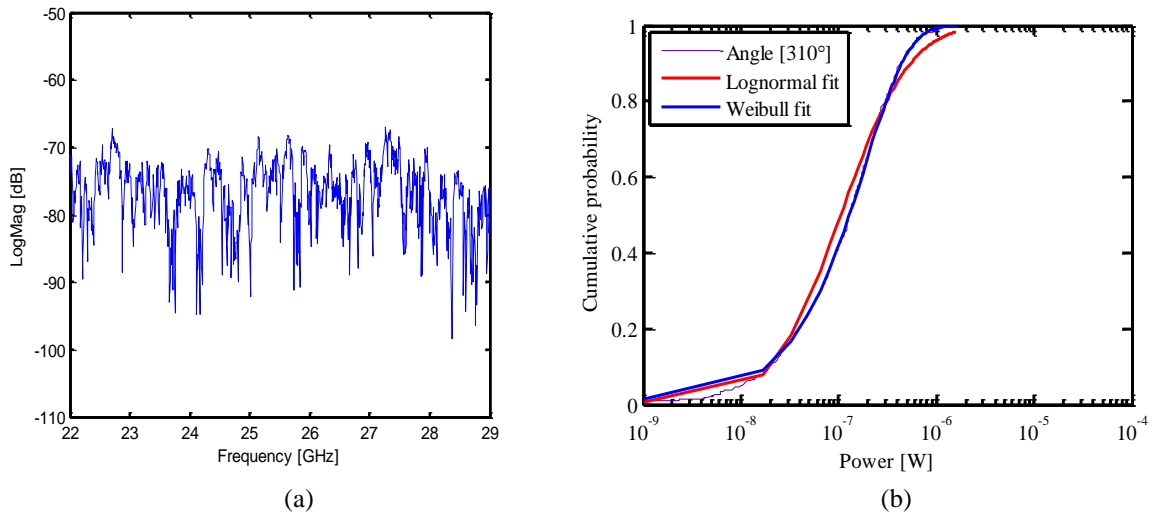


Fig. B.5. RCS of automobile against frequency, measured at angle 310° : (a) Measured raw data and (b) distribution fitting result.

APPENDIX C

RESOLUTION OF TRILATERATION AND TRIANGULATION

Consider a bistatic MIMO radar as illustrated in Fig. C.1. The target can be localized using trilateration and triangulation (DOD/DOA-based) method. The range resolution of trilateration is given by

$$\Delta R_{trl} = \frac{c}{2 \cdot BW}, \quad (C.1)$$

where c is the propagation speed and BW is the bandwidth of the signal used. The range resolution for triangulation is

$$\Delta R_{trg} = \frac{2h}{R_b} \tan(\Delta\theta), \quad (C.2)$$

where $\Delta\theta$ is the achievable resolution of angle estimation. We can observe that in general, the trilateration depends on the BW , and triangulation depends on the $2h/R_b$, which indicated the importance of positional relationship of the target and the respective transmitting and receiving antennas.

The range resolution for both method are compared in Fig. C.2. The signal bandwidth was varied from 10 MHz to 10 GHz. A value of 0.5° was used for $\Delta\theta$ in the case of triangulation. It can be clearly understood that the range resolution of triangulation method do not depend on BW . Its range resolution however changes according to the values of $2h/R_b$.

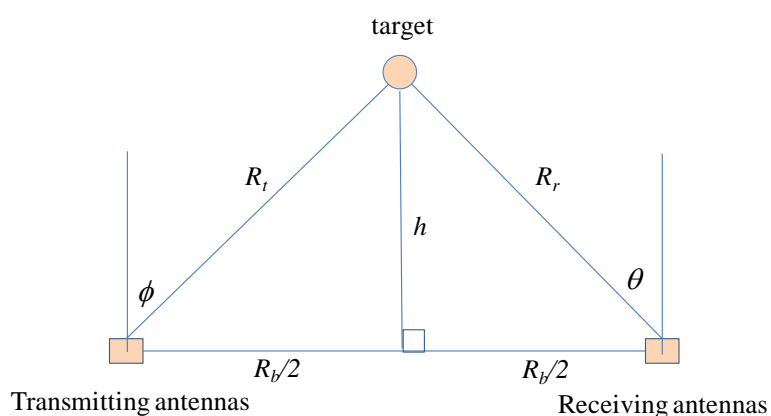


Fig. C.1. Bistatic MIMO radar geometry.

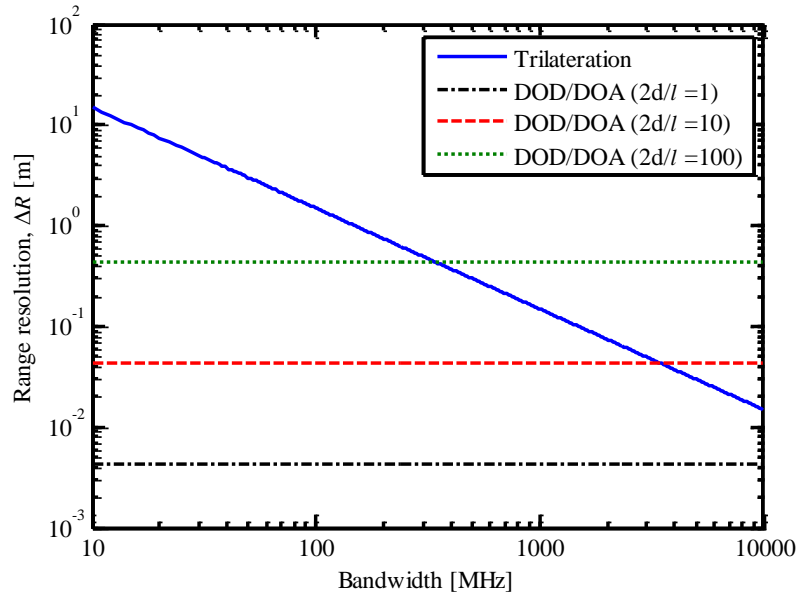


Fig. C.2. Range resolution against bandwidth for triangulation and trilateration methods. ($\Delta\theta = 0.5^\circ$)

APPENDIX D

LIST OF CONTRIBUTIONS AND AWARDS

JOURNAL PAPERS

- [1] **I. Pasya** and T. Kobayashi, "Detection performance of an M-sequence-based MIMO radar system considering jitter influence," *Journal of Selected Areas in Telecommunications*, vol. 3, pp. 16-24, 2013.
- [2] **I. Pasya**, N. Iwakiri, and T. Kobayashi, "Joint direction-of-departure and direction-of-arrival estimation in a UWB MIMO radar detecting targets with fluctuating radar cross sections," *Int. Journal of Antennas and Propag.*, vol. 2014, pp. 1-15, 2014.
- [3] **I. Pasya** and T. Kobayashi, "Joint direction-of-departure and direction-of-arrival estimation in a UWB MIMO radar using OFDM waveform," *Int. Journal of Microwave and Wireless Technology*. (Submitted for review)

INTERNATIONAL CONFERENCES

- [1] **I. Pasya** and T. Kobayashi, "Simulation of time jitter effects on the detection performance of M-sequence based MIMO radar systems," in *2013 IEEE Radio and Wireless Symposium*, pp. 208-210, 2013.
- [2] **I. Pasya** and T. Kobayashi, "Detection performance of M-sequence-based MIMO radar systems considering phase jitter effects," in *2013 IEEE Int. Symposium on Phased Array Systems and Technology*, pp. 394-398, 2013.
- [3] T. Otsuki, **I. Pasya**, and T. Kobayashi, "Experimental evaluation of detection performance of a MIMO radar testbed," in *2013 UNSC URSI National Radio Science Meeting*, pp.1, 2013.
- [4] K. Nagano, **I. Pasya** and T. Kobayashi, "Effects of bandwidth on joint estimation performance of direction-of-departure and direction-of-arrival in ultra-wideband MIMO radar," in *2014 UNSC URSI National Radio Science Meeting*, pp. 1 , 2014.
- [5] **I. Pasya**, N. Iwakiri, and T. Kobayashi, "Joint direction-of-departure and direction-of-arrival estimation in an ultra-wideband MIMO radar system," in *2014 IEEE Radio and Wireless Symposium*, pp. 52-54, 2014.
- [6] **I. Pasya**, N. Iwakiri, and T. Kobayashi, "Performance of joint direction-of-departure and direction-of-arrival estimation in an ultra wideband MIMO radar depending on bandwidths ," in *2014 IEEE Radar Conf.*, pp. 1353-1357, 2014.
- [7] **I. Pasya**, N. Iwakiri, and T. Kobayashi, "Performance of joint direction-of-departure and direction-of-arrival estimation in an ultra wideband MIMO radar detecting targets with fluctuating radar cross sections," in *2014 European Radar Conf.*, EuRAD16-01, 2014.

-
- [8] **I. Pasya** and T. Kobayashi, "Joint direction-of-departure and direction-of-arrival estimation in an MIMO OFDM radar," in *2014 Benjamin Franklin Symposium on Microwave and Antenna Sub-Systems for Radar, Telecommunication and Biomedical Applications*, SA2IF-2, 2014.
- [9] S. Seki, **I. Pasya**, and T. Kobayashi, "Numerical and experimental evaluation of localization methods in a UWB MIMO radar," in *Int. Conf. on Space Aeronautical and Navigational Electronics*, pp. 83-88, 2014.

DOMESTIC CONFERENCES

- [1] **I. Pasya** and T. Kobayashi, "Simulation of time jitter effects on the detection performance of M-sequence based MIMO radar systems," in *2013 IEICE Society Conf.* pp., 2012.
- [2] **I. Pasya**, N. Iwakiri and T. Kobayashi, "Experimental evaluation of joint direction-of-departure and direction-of-arrival in a UWB MIMO radar system," in *2013 IEICE Society Conf.*, 2013.
- [3] K. Nagano, **I. Pasya** and T. Kobayashi, "Experimental evaluation of joint direction-of-departure and direction-of-arrival in a UWB MIMO radar system," in *2013 IEICE Tokyo Shibu*, pp. 208-210, 2013.
- [4] S. Seki, **I. Pasya** and T. Kobayashi, "Target positioning with an ultra wideband MIMO radar" in *2014 Wireless Technology Park*, 2014.

AWARDS

- [1] Best Paper Award, 2014 IEEE Radio and Wireless Symposium, Newport Beach, USA, Jan. 2014.
- I. Pasya**, N. Iwakiri, and T. Kobayashi, "Joint direction-of-departure and direction-of-arrival estimation in an ultra-wideband MIMO radar system".
- [2] Encouragement Award, Tokyo Denki University 11th Idea Contest, Dec. 2013.
- I. Pasya**, and T. Kobayashi, "Joint direction-of-departure and direction-of-arrival estimation in an ultra-wideband MIMO radar". (In Japanese)